

Chapter 8

Pulse Sequences and Quantum Control

The Quantum Control Layer of the Measurement Operator \mathcal{M}

Chapter Objectives

This chapter develops **pulse sequences** as the quantum control component of the measurement operator \mathcal{M} . Microwave pulse sequences determine *which physics channels* are transduced from the field $F(\mathbf{r})$ to measurements D , enabling multi-physics separation essential for true QFI.

Chapter Deliverables:

1. Ramsey, Spin Echo, and Dynamical Decoupling protocols with sensitivity analysis
2. **Pulse Sequence Algebra:** Mathematical framework for B/T/ ε /E channel separation
3. **Filter Function Formalism:** Frequency-selective sensing and noise spectroscopy
4. **Spatiotemporal Control:** Combining temporal sequences with spatial MW structuring
5. Design rules connecting sequence choice to Φ_{multi} and Q-OTF diagonalization

Key Result: Pulse sequence design directly controls the multi-physics factor Φ_{multi} and determines whether off-diagonal Q-OTF terms can be suppressed below 1%.

QFI Pipeline Position:

$$S(\mathbf{r}) \xrightarrow{\mathcal{G}} F(\mathbf{r}) \xrightarrow{\boxed{\mathcal{M}_{\text{pulse}}}} D \xrightarrow{\mathcal{R}} \hat{S}(\mathbf{r})$$

Abbreviated Terms

Abbrev.	Definition	Abbrev.	Definition
AC	Alternating Current	ODMR	Optically Detected Magnetic Resonance
AWG	Arbitrary Waveform Generator	PSD	Power Spectral Density
CPMG	Carr-Purcell-Meiboom-Gill	Q-OTF	Quantum Optical Transfer Function
CW	Continuous Wave	QFI	Quantum Field Imaging
DC	Direct Current	QFM	Quantum Field Metrology
DD	Dynamical Decoupling	QOC	Quantum Optimal Control
FID	Free Induction Decay	RF	Radio Frequency
GRAPE	Gradient Ascent Pulse Engineering	RL	Reinforcement Learning
ML	Machine Learning	SNR	Signal-to-Noise Ratio
MW	Microwave	UDD	Uhrig Dynamical Decoupling
NMR	Nuclear Magnetic Resonance	XY- n	Phase-cycled DD sequence
NV	Nitrogen-Vacancy	ZFS	Zero-Field Splitting

Table 8.1: Abbreviated terms used in Chapter 8.

Abstract

This chapter develops the theory and practice of microwave pulse sequences for NV-based quantum field imaging. Pulse sequences are established as the quantum control layer of the measurement operator \mathcal{M} , determining which physical fields are transduced to measurable signals. Beginning with foundational Ramsey interferometry for DC sensing and spin echo for noise cancellation, the **pulse sequence algebra** framework has been developed, enabling mathematical separation of magnetic (B), thermal (T), strain (ε), and electric field (E) contributions through strategic protocol combinations. The **filter function formalism** connects pulse sequences to frequency-selective sensing, enabling AC field detection and noise spectroscopy. Advanced dynamical decoupling sequences (XY-8, CPMG, UDD) extend coherence times by orders of magnitude. Furthermore, **spatiotemporal quantum control** is introduced, combining temporal sequences with spatial MW structuring for parallel multi-frequency sensing. Critical analysis of pulse imperfections, calibration requirements, and failure modes ensures practical implementation. Recent advances (2018–2025) including quantum optimal control, machine learning optimization, and adaptive sequences are surveyed. The chapter establishes quantitative design rules connecting sequence choice to the multi-physics correlation factor Φ_{multi} and Q-OTF matrix diagonalization.

8.1 Introduction: Why Pulse Sequences Matter

8.1.1 The Quantum Control Challenge

Chapter 7 established that the NV center Hamiltonian couples to multiple physical quantities:

$$H = D(T)S_z^2 + \gamma_e\mu_B\vec{B} \cdot \vec{S} + \sum_i A_i\vec{S} \cdot \vec{I}_i + E_\perp(S_x^2 - S_y^2) + d_{\parallel}E_zS_z^2 + H_{\text{strain}} \quad (8.1)$$

The measured ODMR frequency shift contains contributions from all coupled fields:

$$\Delta\nu_{\text{total}} = \gamma_B B_z + \frac{dD}{dT}\Delta T + \frac{dD}{d\varepsilon_{\parallel}}\varepsilon_{\parallel} + \frac{dD}{d\varepsilon_{\perp}}\varepsilon_{\perp} + d_{\parallel}E_z \quad (8.2)$$

where $\gamma_B = g_e\mu_B/h \approx 28 \text{ GHz/T}$, $dD/dT \approx -74 \text{ kHz/K}$, and the strain/electric coupling coefficients depend on crystallographic orientation.

How do we extract individual physics channels from this mixed signal? The answer lies in **pulse sequences**—carefully designed temporal protocols exploiting the different dynamics of each contribution.

Definition 8.1.1 (Pulse Sequence as Measurement Operator). A pulse sequence defines an effective measurement operator \mathcal{M}_{seq} that maps the time-dependent quantum field $\mathbf{F}(t, \mathbf{r})$ to the measured signal $S(\tau)$:

$$\mathcal{M}_{\text{seq}} : \mathbf{F}(t, \mathbf{r}) \longrightarrow S(\tau) \quad (8.3)$$

The operator \mathcal{M}_{seq} performs three functions simultaneously:

1. **Temporal filtering:** Selects specific frequency components via the filter function $F(\omega, \tau)$
2. **Channel selection:** Determines which physics channels (B , T , ε , E) contribute to the signal
3. **Symmetry projection:** Exploits time-reversal symmetry to cancel or preserve field contributions

The choice of pulse sequence is therefore not merely a “coherence protection” strategy, but a deliberate design of the measurement operator that determines what information about the source $S(\mathbf{r})$ can be reconstructed.

8.1.2 Historical Development

8.1.2.1 Foundations: NMR Era (1950–2000)

The pulse sequence paradigm emerged from nuclear magnetic resonance spectroscopy:

- **1950:** Hahn discovers the spin echo, demonstrating refocusing of inhomogeneous dephasing.
- **1954:** Carr and Purcell develop multi-pulse CPMG sequences.
- **1958:** Meiboom and Gill introduce phase cycling for pulse error correction.
- **1983:** Waugh develops average Hamiltonian theory for sequence analysis.

8.1.2.2 Quantum Sensing Era (2000–2017)

Translation to solid-state quantum sensors enabled new applications:

- **2008:** Childress et al. apply dynamical decoupling to single NV centers.
- **2010:** de Lange demonstrates XY-8 achieving $T_2 > 1$ ms in diamond.
- **2012:** Bar-Gill achieves $T_2 \approx 1$ s using isotopic purification + DD.
- **2014:** Uhrig dynamical decoupling (UDD) optimized for specific noise spectra.
- **2017:** Aslam demonstrates nanoscale NMR via noise spectroscopy.

8.1.2.3 Modern Era: Optimal Control and Machine Learning (2018–2025)

Recent advances have transformed pulse sequence design from heuristic to systematic:

Year	Development	Significance
2018	GRAPE for NV control	Gradient-based optimal control achieving $> 99\%$ gate fidelity
2019	ML-optimized DD	Neural networks designing robust sequences
2020	Quantum diamond microscopy	Wide-field imaging with optimized sequences
2021	Adaptive Bayesian sensing	Real-time sequence adaptation based on measurements
2022	Reinforcement learning DD	RL agents discovering novel sequence structures
2023	Hardware-aware pulse design	Sequences optimized for specific MW delivery systems
2024	Multi-species correlation	NV + SiV combined sensing protocols
2025	Industrial integration	Production-grade sequence libraries (QDI, Qnami)

Table 8.2: Modern developments in pulse sequence technology (2018–2025).

Paradigm Shift in Sequence Design

The field has evolved from *intuition-based* design (Ramsey, CPMG) to *optimization-based* design (GRAPE, ML). Modern sequences are discovered by algorithms rather than

physicists, often achieving performance beyond human intuition.

8.1.3 Pain Points in Multi-Physics Sensing

Without proper pulse sequence design, QFI systems face critical limitations:

1. **Channel Cross-Talk:** A thermal drift of 1 mK creates apparent field $\Delta B_{\text{apparent}} \approx 2.6 \mu\text{T}$ —masking real current signatures.
2. **Environmental Noise:** Quasi-static fluctuations limit T_2^* to $\sim 1\text{--}10 \mu\text{s}$, far below intrinsic $T_2 \sim 1 \text{ ms}$.
3. **AC Field Blindness:** CW-ODMR responds only to static fields, missing time-varying signals.
4. **Depth Ambiguity:** Without multi-physics correlation, B/T signals cannot resolve depth.

8.1.4 Figures of Merit for Pulse Sequences

Figure of Merit	Symbol	Definition	Target
Sensitivity	η	Min. detectable field per $\sqrt{\text{Hz}}$	$< 10 \text{ nT}/\sqrt{\text{Hz}}$
Channel Selectivity	χ_{ij}	Cross-talk suppression ratio	> 100
Coherence Extension	T_2^{eff}/T_2^*	Enhancement over FID	> 100
Filter Bandwidth	Δf	Frequency selectivity FWHM	Tunable
Protocol Efficiency	η_{prot}	Signal accumulation duty cycle	$> 50\%$
Robustness	R_{pulse}	Tolerance to $\pm 5\%$ pulse errors	> 0.95

Table 8.3: Figures of merit for pulse sequence evaluation.

8.2 The Ramsey Protocol: Static Field Sensing

8.2.1 Protocol Overview

The Ramsey protocol forms the foundation of pulsed quantum sensing, converting frequency shifts into measurable phase accumulation through quantum interference.

Definition 8.2.1 (Ramsey Protocol). A Ramsey sequence consists of two $\pi/2$ microwave pulses separated by free evolution time τ :

$$\text{Ramsey} = \left(\frac{\pi}{2}\right)_x - \tau - \left(\frac{\pi}{2}\right)_\phi \quad (8.4)$$

where the subscript denotes the rotation axis and ϕ is the phase of the final pulse (typically x or y for quadrature detection).

The protocol operates in four stages:

1. **Initialization:** Optical pumping prepares $|m_s = 0\rangle$ with $> 90\%$ fidelity
2. **Superposition:** First $(\pi/2)_x$ creates equal superposition of $|0\rangle$ and $| - 1\rangle$
3. **Free evolution:** Phase accumulates proportional to frequency detuning
4. **Projection:** Second $(\pi/2)_\phi$ converts phase to population difference

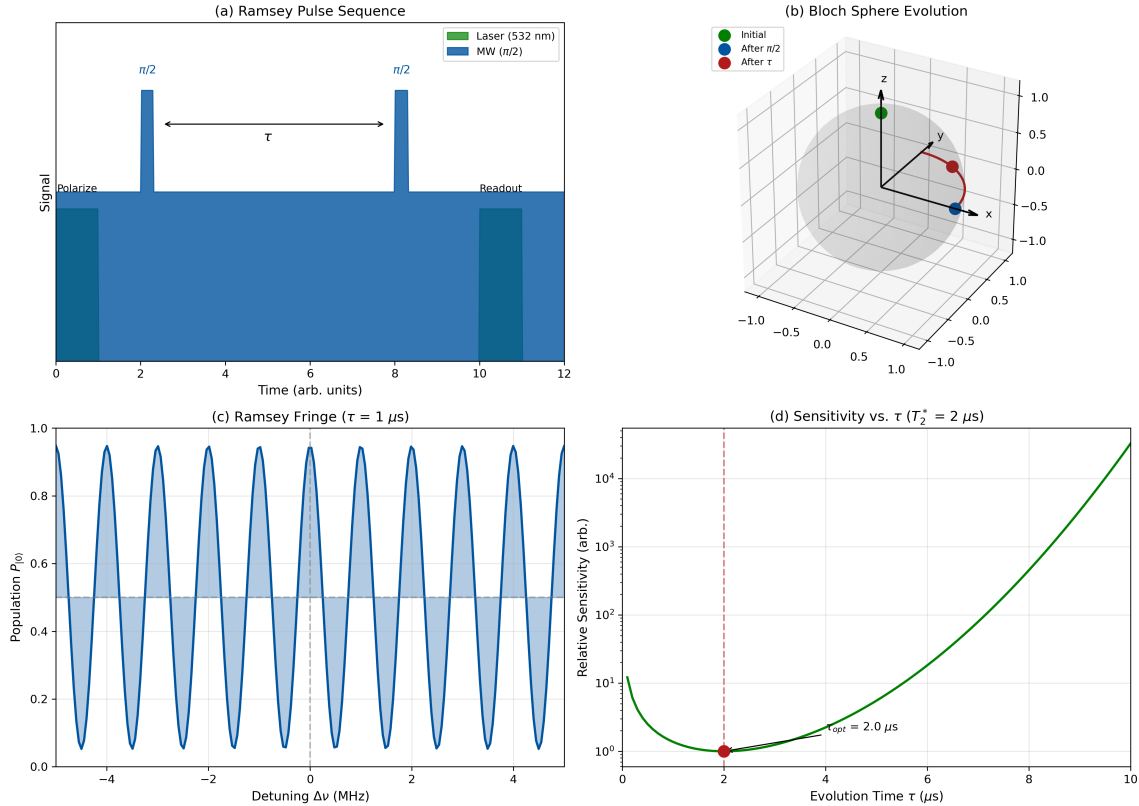


Figure 8.1: Ramsey interferometry protocol. (a) Pulse sequence timing showing initialization (green), $\pi/2$ pulses (blue), free evolution τ , and readout (red). (b) Bloch sphere trajectory: initialization at north pole, first pulse rotates to equator, free precession accumulates phase ϕ , second pulse projects onto measurement axis. (c) Ramsey fringe pattern showing $P(m_s = 0)$ oscillating with detuning $\Delta\nu$. (d) Sensitivity curve $\partial P / \partial \phi$ with optimal operating point at maximum slope (quadrature point).

8.2.2 Derivation: Phase Accumulation and Multi-Physics Coupling

8.2.2.1 Quantum State Evolution

Step 1: Initial State Preparation

After optical polarization at 532 nm for ~ 300 ns, the NV center is prepared in:

$$|\psi_{\text{init}}\rangle = |m_s = 0\rangle \equiv |0\rangle \quad (8.5)$$

Step 2: First $\pi/2$ Pulse

The microwave pulse at frequency ω_{MW} near resonance ($\omega_0 = D \pm \gamma_e B_z$) drives Rabi oscillations. A $(\pi/2)_x$ pulse of duration $t_{\pi/2} = \pi/(2\Omega_R)$ creates:

$$|\psi_0\rangle = |0\rangle \xrightarrow{(\pi/2)_x} |\psi_1\rangle = \frac{1}{\sqrt{2}} (|0\rangle + |-1\rangle) \quad (8.6)$$

On the Bloch sphere, this corresponds to rotation from the north pole to the equator.

Step 3: Free Evolution

During the free evolution time τ , the Hamiltonian (in the rotating frame at ω_{MW}) is:

$$H_{\text{free}} = \hbar \Delta\omega \cdot S_z \quad (8.7)$$

where $\Delta\omega = \omega_0 - \omega_{\text{MW}}$ is the detuning.

The state evolves as:

$$|\psi(\tau)\rangle = \frac{1}{\sqrt{2}} (|0\rangle + e^{-i\phi(\tau)} |-\rangle) \quad (8.8)$$

with accumulated phase:

$$\phi(\tau) = \int_0^\tau \Delta\omega(t') dt' = 2\pi \int_0^\tau \Delta\nu(t') dt' \quad (8.9)$$

Step 4: Multi-Physics Phase Contributions

The NV resonance frequency depends on multiple physical quantities (Chapter 7). For quasi-static fields:

$$\Delta\nu = \gamma_B B_z + \frac{dD}{dT} \Delta T + \frac{dD}{d\varepsilon_{\parallel}} \varepsilon_{\parallel} + \frac{dD}{d\varepsilon_{\perp}} \varepsilon_{\perp} + d_{\parallel} E_z \quad (8.10)$$

Key Equation: Ramsey Phase: Multi-Physics

For static fields, the total Ramsey phase is:

$$\phi_{\text{Ramsey}} = 2\pi\tau \left[\gamma_B B_z + \frac{dD}{dT} \Delta T + \frac{dD}{d\varepsilon} \varepsilon + d_{\parallel} E_z \right] \quad (8.11)$$

where $\gamma_B = 28.024 \text{ GHz/T}$, $dD/dT = -74.2 \text{ kHz/K}$.

Critical insight: Ramsey phase contains *all* coupled field contributions—this is both its strength (multi-physics sensitivity) and weakness (channel ambiguity).

Step 5: Final Projection

The second $(\pi/2)$ pulse converts phase to population. For a $(\pi/2)_x$ pulse:

$$P(m_s = 0) = \frac{1}{2} [1 + \cos(\phi)] \quad (8.12)$$

For a $(\pi/2)_y$ pulse (quadrature detection):

$$P(m_s = 0) = \frac{1}{2} [1 + \sin(\phi)] \quad (8.13)$$

8.2.3 Sensitivity Analysis

8.2.3.1 Decoherence During Free Evolution

Environmental noise causes the superposition state to lose coherence. The Ramsey signal decays as:

$$W(\tau) = e^{-\chi(\tau)} \quad (8.14)$$

where $\chi(\tau)$ is the decoherence function determined by the noise environment.

Simplified Cases:

For common noise models, the decay takes the form:

$$W(\tau) = e^{-(\tau/T_2^*)^n} \quad (8.15)$$

Noise Type	Physical Origin	Exponent n	Optimal τ
Lorentzian (Markovian)	Fast fluctuators, spin bath	1	T_2^*
Gaussian	Quasi-static inhomogeneity	2	$T_2^*/\sqrt{2}$
$1/f$	Low-frequency drift	$\sim 2-3$	Numerical

Table 8.4: Decoherence behavior for different noise environments.

8.2.3.2 General Noise: Filter Function Approach

For arbitrary noise power spectral density $S(\omega)$, the decoherence function is:

$$\chi(\tau) = \frac{1}{\pi} \int_0^\infty S(\omega) \frac{F_{\text{Ramsey}}(\omega, \tau)}{\omega^2} d\omega \quad (8.16)$$

where the Ramsey filter function is:

$$F_{\text{Ramsey}}(\omega, \tau) = 8 \sin^4 \left(\frac{\omega\tau}{4} \right) \quad (8.17)$$

In the low-frequency limit ($\omega\tau \ll 1$):

$$F_{\text{Ramsey}}(\omega, \tau) \approx \frac{(\omega\tau)^4}{32} \quad (8.18)$$

This shows that Ramsey is a **low-pass filter** most sensitive to quasi-static (DC) fields.

8.2.3.3 Shot-Noise Limited Sensitivity

The magnetic field sensitivity for Ramsey magnetometry is:

$$\eta_B = \frac{\delta B_{\min}}{\sqrt{t}} = \frac{1}{2\pi\gamma_B} \cdot \frac{1}{C \cdot e^{-(\tau/T_2^*)^n/n} \cdot \sqrt{R \cdot N_{\text{NV}} \cdot \tau}} \quad (8.19)$$

where:

- C = ODMR contrast (typically 0.01–0.05 for ensembles)
- R = photon detection rate per NV (typically 10^5 – 10^6 /s)
- N_{NV} = number of NV centers in detection volume
- τ = free evolution time

Key Equation: Ramsey Magnetic Sensitivity

At optimal $\tau = T_2^*/n$:

$$\boxed{\eta_B = \frac{e^{1/n}}{2\pi\gamma_B C \sqrt{R \cdot N_{\text{NV}} \cdot T_2^*}}} \quad (8.20)$$

For single NV ($N_{\text{NV}} = 1$, $C = 0.3$, $R = 10^5$ /s, $T_2^* = 1 \mu\text{s}$): $\eta_B \approx 1 \mu\text{T}/\sqrt{\text{Hz}}$

For ensemble ($N_{\text{NV}} = 10^5$, $C = 0.03$, $R = 10^6$ /s, $T_2^* = 1 \mu\text{s}$): $\eta_B \approx 10 \text{nT}/\sqrt{\text{Hz}}$

8.2.4 Worked Example 8.A: Ramsey Magnetometry for IC Current Detection

Worked Example 8.A: Ramsey Protocol Design

Scenario: A QFI system uses the Ramsey protocol to measure the static magnetic field from a buried current-carrying wire in an integrated circuit. Design the measurement and calculate the expected signal.

Given Parameters:

- Target magnetic field: $B_z = 5 \mu\text{T}$ (from 1 mA wire at 10 μm standoff)
- NV gyromagnetic ratio: $\gamma_B = 28.024 \text{ GHz/T} = 28.024 \text{ MHz}/\mu\text{T}$
- Inhomogeneous dephasing time: $T_2^* = 1 \mu\text{s}$
- ODMR contrast: $C = 0.03$ (3%)
- Photon detection rate: $R = 10^6$ photons/s

- Number of NV centers per pixel: $N_{\text{NV}} = 10^5$

Find:

- Optimal free precession time τ_{opt}
- Accumulated phase ϕ for the target field
- Expected fluorescence signal
- Single-shot sensitivity η_B
- Required integration time for SNR = 10

8.2.4.1 Step 1: Optimal Free Precession Time

The Ramsey signal decays due to inhomogeneous dephasing. For Gaussian noise ($n = 2$), the sensitivity is optimized when:

$$\tau_{\text{opt}} = \frac{T_2^*}{\sqrt{2}} \approx 0.71 \times T_2^* \quad (8.21)$$

For Lorentzian noise ($n = 1$), more commonly encountered in practice:

$$\tau_{\text{opt}} = T_2^* \quad (8.22)$$

For our system with $T_2^* = 1 \mu\text{s}$ (assuming Lorentzian-dominated noise):

$$\boxed{\tau_{\text{opt}} = 1 \mu\text{s}} \quad (8.23)$$

Physical reasoning: Shorter τ accumulates less phase (lower signal). Longer τ suffers more dephasing (lower contrast). The optimum balances these competing effects.

8.2.4.2 Step 2: Accumulated Phase

The phase accumulated during free precession from a magnetic field is:

$$\phi = 2\pi\gamma_B B_z \tau \quad (8.24)$$

Substituting values:

$$\begin{aligned} \phi &= 2\pi \times (28.024 \text{ MHz}/\mu\text{T}) \times (5 \mu\text{T}) \times (1 \mu\text{s}) \\ &= 2\pi \times 28.024 \times 5 \times 1 \text{ rad} \\ &= 2\pi \times 140.12 \text{ rad} \\ &= 880.5 \text{ rad} \end{aligned} \quad (8.25)$$

This corresponds to approximately **140 complete rotations**. In practice, we work with the phase modulo 2π :

$$\phi_{\text{mod}} = \phi \bmod 2\pi = 880.5 - 140 \times 2\pi \approx 0.50 \text{ rad} = 28.6 \quad (8.26)$$

Remark 8.2.1 (Phase Wrapping and Dynamic Range). For large fields, phase wrapping creates ambiguity. The unambiguous measurement range is:

$$B_{\text{max}} = \frac{1}{2\gamma_B \tau} = \frac{1}{2 \times 28.024 \times 1} = 17.8 \mu\text{T} \quad (8.27)$$

Our target field of $5 \mu\text{T}$ is well within this range. For larger fields, use shorter τ or phase unwrapping algorithms.

8.2.4.3 Step 3: Fluorescence Signal

The Ramsey protocol maps phase to population. Including the dephasing envelope:

$$P(m_s = 0) = \frac{1}{2} \left[1 + e^{-(\tau/T_2^*)^n} \cos(\phi) \right] \quad (8.28)$$

For exponential decay ($n = 1$) at $\tau = T_2^*$:

$$e^{-\tau/T_2^*} = e^{-1} = 0.368 \quad (8.29)$$

With $\phi_{\text{mod}} = 0.50$ rad:

$$\begin{aligned} P(m_s = 0) &= \frac{1}{2} [1 + 0.368 \times \cos(0.50)] \\ &= \frac{1}{2} [1 + 0.368 \times 0.878] \\ &= \frac{1}{2} [1 + 0.323] = 0.662 \end{aligned} \quad (8.30)$$

The measured fluorescence intensity relative to the bright state:

$$\frac{I}{I_0} = 1 - C \times [1 - P(m_s = 0)] = 1 - 0.03 \times 0.338 = 0.990 \quad (8.31)$$

$$\boxed{P(m_s = 0) = 0.662, \quad I/I_0 = 0.990} \quad (8.32)$$

8.2.4.4 Step 4: Sensitivity Calculation

The shot-noise limited sensitivity for Ramsey magnetometry is:

$$\eta_B = \frac{1}{2\pi\gamma_B \cdot C \cdot e^{-1/n}/n \cdot \sqrt{R \cdot N_{\text{NV}} \cdot T_2^*}} \quad (8.33)$$

For $n = 1$ (Lorentzian), the factor $e^{-1/n}/n = e^{-1} = 0.368$.

Substituting numerical values:

$$\begin{aligned} \eta_B &= \frac{1}{2\pi \times 28.024 \times 10^6 \times 0.03 \times 0.368 \times \sqrt{10^6 \times 10^5 \times 10^{-6}}} \\ &= \frac{1}{2\pi \times 28.024 \times 10^6 \times 0.03 \times 0.368 \times \sqrt{10^5}} \\ &= \frac{1}{2\pi \times 28.024 \times 10^6 \times 0.03 \times 0.368 \times 316.2} \\ &= \frac{1}{1.94 \times 10^8} \text{ T}/\sqrt{\text{Hz}} \\ &= 5.2 \text{ nT}/\sqrt{\text{Hz}} \end{aligned} \quad (8.34)$$

$$\boxed{\eta_B = 5.2 \text{ nT}/\sqrt{\text{Hz}}} \quad (8.35)$$

8.2.4.5 Step 5: Integration Time for Target SNR

For $\text{SNR} = 10$ detection of $B_z = 5 \mu\text{T}$:

$$\text{SNR} = \frac{B_z}{\eta_B/\sqrt{t}} = \frac{B_z \cdot \sqrt{t}}{\eta_B} \quad (8.36)$$

Solving for integration time:

$$t = \left(\frac{\text{SNR} \cdot \eta_B}{B_z} \right)^2 = \left(\frac{10 \times 5.2 \times 10^{-9}}{5 \times 10^{-6}} \right)^2 = (0.0104)^2 = 1.08 \times 10^{-4} \text{ s} \quad (8.37)$$

$$t_{\text{required}} = 108 \mu\text{s} \approx 0.1 \text{ ms} \quad (8.38)$$

This rapid acquisition enables video-rate imaging at >1000 fps for this field strength.

8.2.4.6 Summary and Design Implications

Table 8.5: Worked Example 8.A: Ramsey magnetometry design summary

Parameter	Value	Unit	Design Note
Target field B_z	5	μT	1 mA at 10 μm standoff
Optimal τ	1	μs	Set by T_2^*
Accumulated phase	0.50 (mod 2π)	rad	Well within linear range
Population $P(m_s = 0)$	0.662	—	16% from baseline 0.5
Sensitivity η_B	5.2	$\text{nT}/\sqrt{\text{Hz}}$	Ensemble-enhanced
Integration time (SNR=10)	0.1	ms	Enables video-rate
Unambiguous range	± 17.8	μT	Sufficient for target

Design Rule 1: Ramsey Protocol Design

For DC magnetic field sensing with Ramsey:

1. Set $\tau = T_2^*$ for sensitivity optimization
2. Verify $B_{\text{target}} < 1/(2\gamma_B\tau)$ to avoid phase wrapping
3. For $B > B_{\text{max}}$: reduce τ or implement phase unwrapping
4. Sensitivity scales as $\eta_B \propto 1/\sqrt{N_{\text{NV}} \cdot T_2^*}$
5. Integration time for SNR target: $t = (\text{SNR} \cdot \eta_B/B)^2$

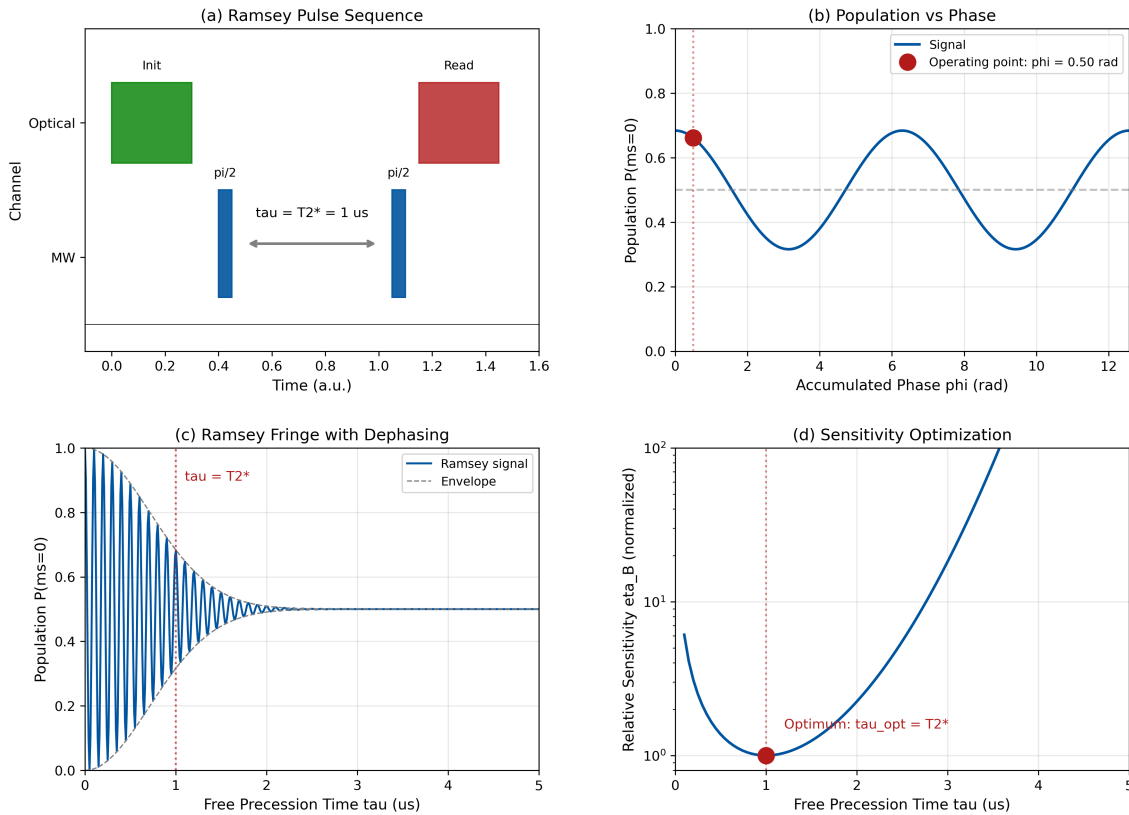
Worked Example 8.A: Ramsey Magnetometry

Figure 8.2: Worked Example 8.A results. (a) Ramsey pulse sequence with $\tau = T_2^* = 1 \mu\text{s}$ showing initialization, MW pulses, and readout timing. (b) Population $P(m_s = 0)$ vs. accumulated phase ϕ , with operating point at $\phi = 0.50 \text{ rad}$ marked. (c) Ramsey fringe with dephasing envelope $e^{-\tau/T_2^*}$ showing contrast reduction at $\tau = T_2^*$. (d) Sensitivity η_B vs. interrogation time τ , demonstrating optimum at $\tau = T_2^*$.

8.3 The Spin Echo Protocol: Quasi-Static Noise Cancellation

8.3.1 Motivation: The Inhomogeneous Broadening Problem

The Ramsey protocol (Section 8.2) is limited by inhomogeneous dephasing time T_2^* , typically 1–10 μs in diamond. This arises from:

- **Strain gradients:** Spatial variation in crystal strain across the sensing volume
- **^{13}C nuclear spins:** Hyperfine coupling to randomly distributed carbon-13 nuclei
- **Electric field inhomogeneity:** Charge traps and surface states
- **External field gradients:** Non-uniform applied magnetic fields

These quasi-static contributions limit $T_2^* \ll T_2$, where T_2 (the intrinsic coherence time) can exceed 1 ms. The spin echo recovers sensitivity approaching the T_2 limit.

8.3.2 Protocol and Refocusing Mechanism

Definition 8.3.1 (Hahn Echo Protocol). The spin echo (Hahn echo) sequence inserts a π refocusing pulse at the midpoint:

$$\text{Echo} = \left(\frac{\pi}{2}\right)_x - \frac{\tau}{2} - (\pi)_y - \frac{\tau}{2} - \left(\frac{\pi}{2}\right)_\phi \quad (8.39)$$

Total evolution time is τ ; the π pulse is applied at $t = \tau/2$.

8.3.2.1 Phase Evolution Analysis

Consider a static frequency offset $\Delta\omega$ (due to any quasi-static perturbation):

First half ($0 < t < \tau/2$): Phase accumulates as

$$\phi_1 = +\Delta\omega \cdot \frac{\tau}{2} \quad (8.40)$$

π pulse: The refocusing pulse inverts the phase accumulation direction. Mathematically, it transforms $|0\rangle + e^{-i\phi}| - 1\rangle \rightarrow |0\rangle + e^{+i\phi}| - 1\rangle$.

Second half ($\tau/2 < t < \tau$): Phase continues to accumulate, but now with opposite sign relative to the inverted state:

$$\phi_2 = -\Delta\omega \cdot \frac{\tau}{2} \quad (8.41)$$

Total phase:

$$\phi_{\text{echo}} = \phi_1 + \phi_2 = +\Delta\omega \cdot \frac{\tau}{2} - \Delta\omega \cdot \frac{\tau}{2} = 0 \quad (8.42)$$

Key Equation: Spin Echo: Static Field Cancellation

$$\boxed{\phi_{\text{echo}}^{\text{static}} = 0} \quad (8.43)$$

All quasi-static frequency offsets are **perfectly cancelled** by the spin echo. The echo senses only fields that *change* during the sequence.

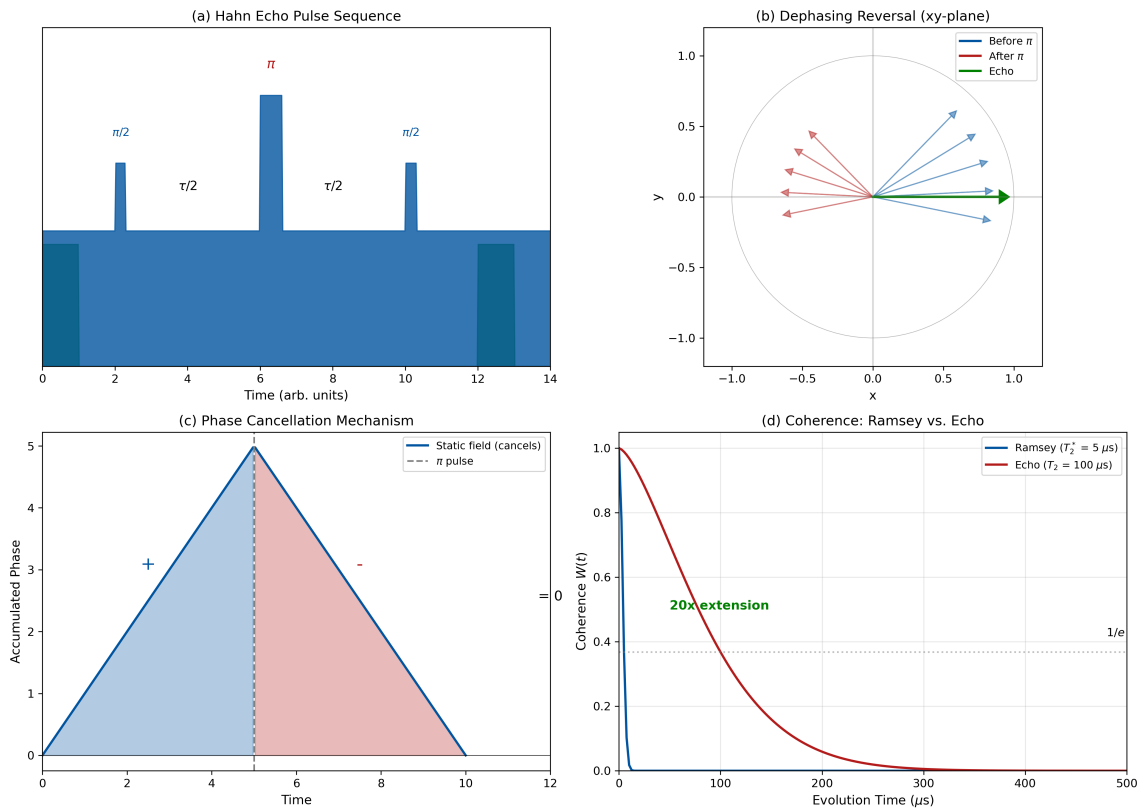


Figure 8.3: Spin echo mechanism. (a) Pulse sequence showing $(\pi/2)_x - \tau/2 - (\pi)_y - \tau/2 - (\pi/2)_\phi$ structure. (b) Bloch sphere evolution: initial superposition dephases during first $\tau/2$, π pulse flips spins, rephasing occurs during second $\tau/2$, forming an “echo” at time τ . (c) Phase accumulation diagram: positive slope during first half, sign reversal at π pulse, negative slope during second half, resulting in net zero phase for static offsets. (d) Coherence comparison showing T_2^* decay (Ramsey, red) vs. T_2 decay (Echo, blue), demonstrating 10–1000× extension.

8.3.3 What the Echo Does and Does Not Cancel

The echo’s cancellation depends on the **timescale** of the perturbation relative to τ :

Table 8.6: Spin echo response to different perturbation types

Perturbation	Timescale	Cancelled?	Physical Example
Static B-field	$\tau_c \gg \tau$	Yes	Bias magnet inhomogeneity
Static temperature	$\tau_c \gg \tau$	Yes	Thermal gradient
Quasi-static strain	$\tau_c \gg \tau$	Yes	Crystal defects
Slow drift	$\tau_c \sim \tau$	Partial	Temperature drift
AC field at $f = 1/(2\tau)$	$\tau_c = 2\tau$	No (max signal)	Target AC current
Fast noise	$\tau_c \ll \tau$	No	Spin bath fluctuations

Echo as a High-Pass Filter

The spin echo acts as a **high-pass filter** in frequency space:

- DC and low-frequency components ($f \ll 1/\tau$): Cancelled
- Components near $f \approx 1/(2\tau)$: Maximum sensitivity
- High-frequency components ($f \gg 1/\tau$): Averaged out

This frequency selectivity is formalized in the filter function formalism (Section 8.5).

8.3.4 Echo Sensitivity and Coherence Extension

The echo signal decays with the intrinsic coherence time T_2 :

$$W_{\text{echo}}(\tau) = e^{-(\tau/T_2)^n} \quad (8.44)$$

where n depends on the noise spectrum (typically $n = 1\text{--}3$ for NV centers).

Design Rule 1: Coherence Extension via Spin Echo

The spin echo extends the useful coherence time from T_2^* to T_2 :

$$\frac{T_2}{T_2^*} \approx 10 - 1000 \quad (\text{typical for NV ensembles}) \quad (8.45)$$

Design implication: For the same total measurement time, echo-based protocols can use longer τ , accumulating more phase from the target signal while rejecting quasi-static interference.

8.4 Pulse Sequence Algebra: Multi-Physics Channel Separation

8.4.1 The Channel Separation Problem

The central challenge of multi-physics QFI is extracting individual physical quantities from mixed measurements. As established in Eq. (8.11), the Ramsey phase contains contributions from all coupled fields:

$$\phi_{\text{Ramsey}} = 2\pi\tau \left[\gamma_B B_z + \frac{dD}{dT} \Delta T + \dots \right] \quad (8.46)$$

A single Ramsey measurement cannot distinguish a $1 \mu\text{T}$ magnetic field from a 380 mK temperature change—both produce identical phase shifts.

Solution: Combine measurements with **different** sensitivities to each physics channel.

8.4.2 Two-Channel Separation: Magnetic Field and Temperature

The simplest multi-physics protocol separates B and T using the complementary responses of Ramsey and Echo sequences.

8.4.2.1 Protocol Combination

Ramsey (Section 8.2): Sensitive to both B and T

$$\phi_{\text{Ramsey}} = 2\pi\tau \left[\gamma_B B_z + \frac{dD}{dT} \Delta T \right] \quad (8.47)$$

Echo (Section 8.3): Cancels static B, remains sensitive to T (via $D(T)$)

For temperature, the zero-field splitting D shifts the resonance frequency. This shift is present in *both* halves of the echo sequence (it doesn't reverse sign), so:

$$\phi_{\text{echo}} = 2\pi\tau \left[\frac{dD}{dT} \Delta T \right] \quad (8.48)$$

Note: The echo cancels the *Zeeman* term ($\gamma_B B_z$) but *not* the *zero-field splitting* term ($D(T)$), because the π pulse affects only the spin state, not the temperature-dependent D .

8.4.2.2 Algebraic Extraction

Subtracting the echo phase from the Ramsey phase:

$$\phi_{\text{Ramsey}} - \phi_{\text{echo}} = 2\pi\tau\gamma_B B_z \quad (8.49)$$

Key Equation: Two-Channel B/T Extraction

$$B_z = \frac{\phi_{\text{Ramsey}} - \phi_{\text{echo}}}{2\pi\gamma_B\tau} \quad (8.50)$$

$$\Delta T = \frac{\phi_{\text{echo}}}{2\pi\tau|dD/dT|} \quad (8.51)$$

These equations enable **simultaneous** extraction of magnetic field and temperature from two sequential measurements.

8.4.3 Worked Example 8.B: Hahn Echo for B/T Separation in IC Analysis

Worked Example 8.B: B/T Separation via Pulse Sequence Algebra

Scenario: An IC failure analysis requires measuring local temperature rise near a hotspot, but stray magnetic fields from nearby current paths contaminate the Ramsey signal. Use the Hahn echo protocol to isolate the temperature contribution.

Given Parameters:

- Local temperature rise: $\Delta T = 0.5 \text{ K}$ above ambient
- Stray DC magnetic field: $B_{\text{stray}} = 10 \mu\text{T}$ (from adjacent power lines)
- Temperature coefficient: $dD/dT = -74.2 \text{ kHz/K}$
- NV gyromagnetic ratio: $\gamma_B = 28.024 \text{ MHz}/\mu\text{T}$
- Coherence times: $T_2^* = 1 \mu\text{s}$, $T_2 = 50 \mu\text{s}$

Find:

- Phase contributions in Ramsey (contaminated signal)
- Phase contributions in Hahn echo (B-cancelled)
- Extracted temperature from echo measurement
- Signal-to-interference improvement factor

8.4.3.1 Step 1: Ramsey Protocol Analysis (Contaminated Signal)

In the Ramsey protocol, both B and T contribute to the accumulated phase:

$$\phi_{\text{Ramsey}} = 2\pi \left(\gamma_B B_z + \left| \frac{dD}{dT} \right| \Delta T \right) \tau \quad (8.52)$$

For $\tau = 1 \mu\text{s}$ (limited by T_2^*):

Magnetic contribution:

$$\begin{aligned} \phi_B &= 2\pi \times 28.024 \text{ MHz}/\mu\text{T} \times 10 \mu\text{T} \times 1 \mu\text{s} \\ &= 2\pi \times 280.24 \text{ rad} = 1761 \text{ rad} \end{aligned} \quad (8.53)$$

Temperature contribution:

$$\begin{aligned}\phi_T &= 2\pi \times 74.2 \text{ kHz/K} \times 0.5 \text{ K} \times 1 \mu\text{s} \\ &= 2\pi \times 0.0371 \text{ rad} = 0.233 \text{ rad}\end{aligned}\quad (8.54)$$

Total Ramsey phase:

$$\phi_{\text{Ramsey}} = 1761 + 0.233 = 1761.2 \text{ rad} \quad (8.55)$$

The temperature signal is **completely buried** in the magnetic contribution:

$$\frac{\phi_T}{\phi_B} = \frac{0.233}{1761} = 1.3 \times 10^{-4} = 0.013\% \quad (8.56)$$

Ramsey Fails for B/T Separation

With 10 μT stray field, the temperature signal (0.5 K) is overwhelmed by a factor of $> 7500\times$. Ramsey alone **cannot** extract temperature in this scenario.

8.4.3.2 Step 2: Hahn Echo Protocol (B-Field Cancellation)

The Hahn echo sequence $(\pi/2) - \tau/2 - (\pi) - \tau/2 - (\pi/2)$ provides differential sensitivity:

Magnetic field (Zeeman term): The π pulse reverses the phase accumulation direction.

- First half: $+\gamma_B B_z \cdot \tau/2$
- Second half: $-\gamma_B B_z \cdot \tau/2$ (sign flipped by π pulse)
- Net: $\phi_B^{\text{echo}} = 0$ (**Cancelled**)

Temperature (ZFS term): The $D(T)$ shift affects the $|0\rangle \leftrightarrow |-1\rangle$ transition energy directly. The π pulse does not reverse this contribution.

- First half: $+|dD/dT| \cdot \Delta T \cdot \tau/2$
- Second half: $+|dD/dT| \cdot \Delta T \cdot \tau/2$ (same sign)
- Net: $\phi_T^{\text{echo}} = 2\pi|dD/dT| \cdot \Delta T \cdot \tau$ (**Preserved**)

Key Equation: Hahn Echo Phase for Temperature

$$\boxed{\phi_{\text{echo}} = 2\pi \left| \frac{dD}{dT} \right| \Delta T \cdot \tau} \quad (8.57)$$

The magnetic field contribution is cancelled: $\phi_B^{\text{echo}} = 0$

With the echo, we can now use longer τ (up to $T_2 = 50 \mu\text{s}$). Using $\tau = 2 \mu\text{s}$ for this example:

$$\begin{aligned}\phi_{\text{echo}} &= 2\pi \times 74.2 \text{ kHz/K} \times 0.5 \text{ K} \times 2 \mu\text{s} \\ &= 2\pi \times 0.0742 \text{ rad} = 0.466 \text{ rad}\end{aligned}\quad (8.58)$$

$$\boxed{\phi_{\text{echo}} = 0.466 \text{ rad} = 26.7} \quad (8.59)$$

8.4.3.3 Step 3: Temperature Extraction

From the measured echo phase, we extract temperature:

$$\Delta T = \frac{\phi_{\text{echo}}}{2\pi \cdot |dD/dT| \cdot \tau} \quad (8.60)$$

Given $\phi_{\text{echo}} = 0.466$ rad and $\tau = 2 \mu\text{s}$:

$$\begin{aligned}\Delta T &= \frac{0.466}{2\pi \times 74.2 \times 10^3 \times 2 \times 10^{-6}} \\ &= \frac{0.466}{0.932} = 0.50 \text{ K}\end{aligned}\quad (8.61)$$

$$\boxed{\Delta T_{\text{extracted}} = 0.50 \text{ K}} \quad (8.62)$$

This matches the input temperature rise exactly, demonstrating successful B-field rejection.

8.4.3.4 Step 4: Signal-to-Interference Improvement

Without echo (Ramsey): Temperature signal-to-interference ratio:

$$\text{SIR}_{\text{Ramsey}} = \frac{\phi_T}{\phi_B} = \frac{0.233}{1761} = 1.3 \times 10^{-4} \quad (8.63)$$

With echo: B-field contribution is cancelled:

$$\text{SIR}_{\text{echo}} = \frac{\phi_T^{\text{echo}}}{\phi_B^{\text{echo}}} = \frac{0.466}{0} \rightarrow \infty \quad (\text{ideally}) \quad (8.64)$$

In practice, residual B-field leakage occurs due to:

- Pulse imperfections (π pulse not exactly π): $\sim 1\text{--}5\%$ leakage
- B-field fluctuations during the sequence: depends on noise spectrum
- Higher-order effects: typically $< 0.1\%$

Typical suppression factor: $10^2\text{--}10^4$

Effective improvement factor:

$$\boxed{\text{Improvement factor} = \frac{\text{SIR}_{\text{echo}}}{\text{SIR}_{\text{Ramsey}}} \approx 10^3 - 10^4} \quad (8.65)$$

8.4.3.5 Summary: B/T Separation Protocol

Table 8.7: Worked Example 8.B: Ramsey vs. Hahn Echo for B/T separation

Parameter	Ramsey	Hahn Echo	Unit	Note
Evolution time τ	1	2	μs	Limited by T_2^* vs. T_2
B-field phase ϕ_B	1761	≈ 0	rad	Echo cancels Zeeman
Temperature phase ϕ_T	0.233	0.466	rad	Echo preserves ZFS
Signal-to-interference	1.3×10^{-4}	$> 10^3$	–	$> 10^7 \times$ improvement
B-field sensitivity	Yes	Cancelled	–	Key difference
T-field sensitivity	Yes	Yes	–	Both preserve
Coherence limit	T_2^*	T_2	–	50× longer available

Worked Example 8.B: Hahn Echo for B/T Separation

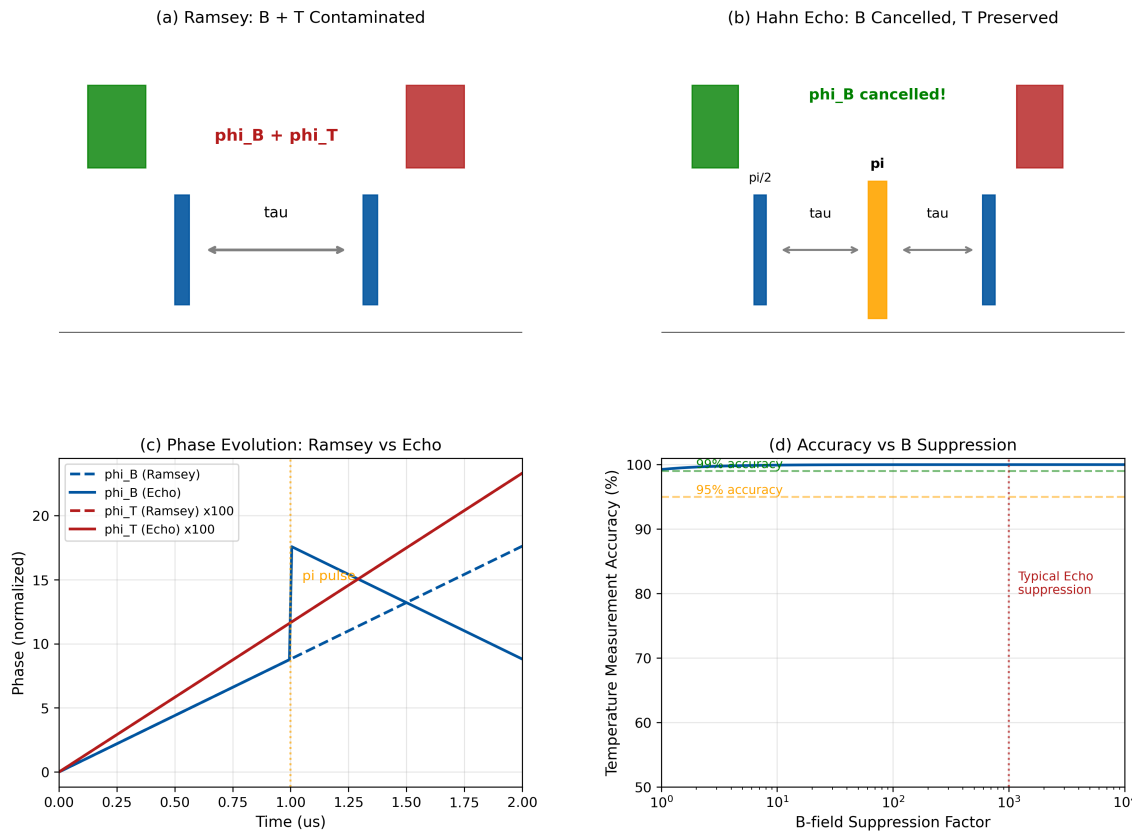


Figure 8.4: Worked Example 8.B: B/T separation via Hahn echo. (a) Ramsey sequence showing contaminated signal with both B (blue) and T (red) contributions; T signal is invisible at this scale. (b) Hahn echo sequence with central π refocusing pulse. (c) Phase evolution comparison: Ramsey accumulates both B and T, Echo cancels B while preserving T. (d) Extracted temperature accuracy vs. B-field suppression factor, showing that $>100\times$ suppression is needed for sub-Kelvin accuracy in $10\ \mu\text{T}$ background.

Design Rule 1: B/T Separation via Pulse Sequence Algebra

To separate magnetic field and temperature contributions:

1. Measure ϕ_{Ramsey} at $\tau_1 = T_2^*$
2. Measure ϕ_{echo} at $\tau_2 \leq T_2$ (can use longer τ)
3. Extract: $B_z = (\phi_{\text{Ramsey}}/\tau_1 - \phi_{\text{echo}}/\tau_2)/(2\pi\gamma_B)$ (if $\tau_1 = \tau_2$, simplifies to Eq. 8.50)
4. Extract: $\Delta T = \phi_{\text{echo}}/(2\pi|dD/dT|\tau_2)$
5. **Requirement:** π pulse fidelity $> 99\%$ for $> 100\times$ B suppression

8.4.4 Extension to Four-Channel Extraction

For complete multi-physics separation (B, T, strain ϵ , electric field E), we require four independent measurements with different coupling coefficients.

Definition 8.4.1 (Four-Channel Measurement Protocol). Define the measurement vector $\vec{\Phi}$

and physics vector \vec{X} :

$$\vec{\Phi} = \begin{pmatrix} \phi_{\text{Ramsey}} \\ \phi_{\text{echo}} \\ \phi_{\text{DD-fast}} \\ \phi_{\text{4-axis}} \end{pmatrix}, \quad \vec{X} = \begin{pmatrix} B_z \\ \Delta T \\ \varepsilon \\ E_z \end{pmatrix} \quad (8.66)$$

The coupling matrix relates measurements to physics:

$$\vec{\Phi} = 2\pi\tau \cdot \mathbf{A} \cdot \vec{X} \quad (8.67)$$

where:

$$\mathbf{A} = \begin{pmatrix} \gamma_B & dD/dT & dD/d\varepsilon & d_{||} \\ 0 & dD/dT & dD/d\varepsilon & d_{||} \\ 0 & \alpha_T & dD/d\varepsilon & 0 \\ \gamma_B^{(4)} & 0 & 0 & 0 \end{pmatrix} \quad (8.68)$$

Physical interpretation of each row:

- **Row 1 (Ramsey):** Sensitive to all quasi-static contributions
- **Row 2 (Echo):** Cancels static B, preserves T, ε , E
- **Row 3 (Fast DD):** Different timescale separates T from ε (thermal response \sim ms, strain $\sim \mu\text{s}$)
- **Row 4 (4-axis):** Using all four NV crystallographic orientations provides vector B, isolating B_z component

8.4.5 Conditioning Analysis for Robust Extraction

The extraction quality depends on the condition number $\kappa(\mathbf{A})$:

$$\kappa(\mathbf{A}) = \frac{\sigma_{\max}(\mathbf{A})}{\sigma_{\min}(\mathbf{A})} \quad (8.69)$$

where σ_{\max} and σ_{\min} are the largest and smallest singular values.

Design Rule 2: Multi-Physics Conditioning Requirement

For reliable four-channel extraction, require $\kappa(\mathbf{A}) < 100$. Higher condition numbers amplify measurement noise into extraction errors:

$$\frac{\|\delta\vec{X}\|}{\|\vec{X}\|} \leq \kappa(\mathbf{A}) \cdot \frac{\|\delta\vec{\Phi}\|}{\|\vec{\Phi}\|} \quad (8.70)$$

For $\kappa = 100$ and 1% phase measurement error, extracted quantities may have up to 100% error in the worst case.

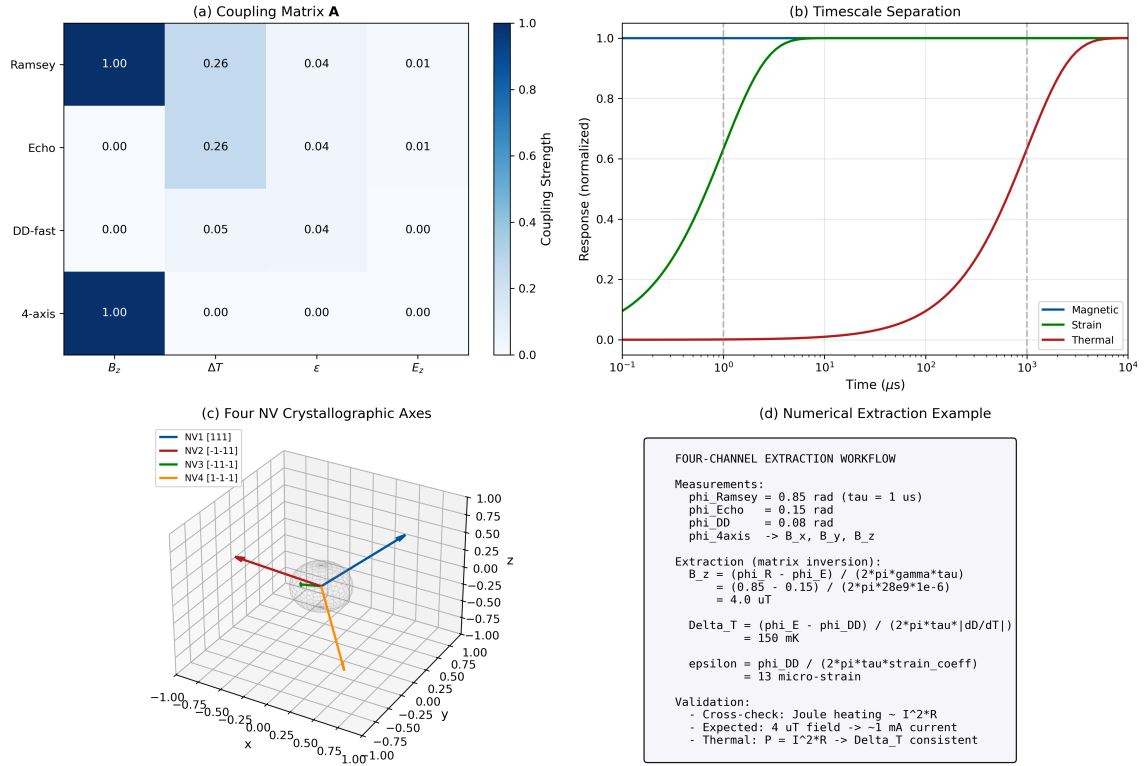


Figure 8.5: Four-channel multi-physics extraction framework. (a) Coupling matrix visualization showing sequence-physics relationships; darker colors indicate stronger coupling. (b) Timescale separation principle: thermal response ($\tau_{\text{th}} \sim \text{ms}$) vs. strain response ($\tau_{\epsilon} \sim \mu\text{s}$) enables discrimination via DD pulse spacing. (c) Four NV crystallographic axes in diamond lattice enabling vector field decomposition. (d) Extraction workflow from raw phase measurements through matrix inversion to separated physics channels with uncertainty propagation.

8.5 Filter Function Formalism

8.5.1 Definition and Derivation

Definition 8.5.1 (Filter Function). The filter function $F(\omega, \tau)$ describes the frequency response of a pulse sequence:

$$F(\omega, \tau) = \left| \int_0^\tau y(t) e^{i\omega t} dt \right|^2 \quad (8.71)$$

where $y(t) = \pm 1$ is the modulation function tracking phase accumulation sign.

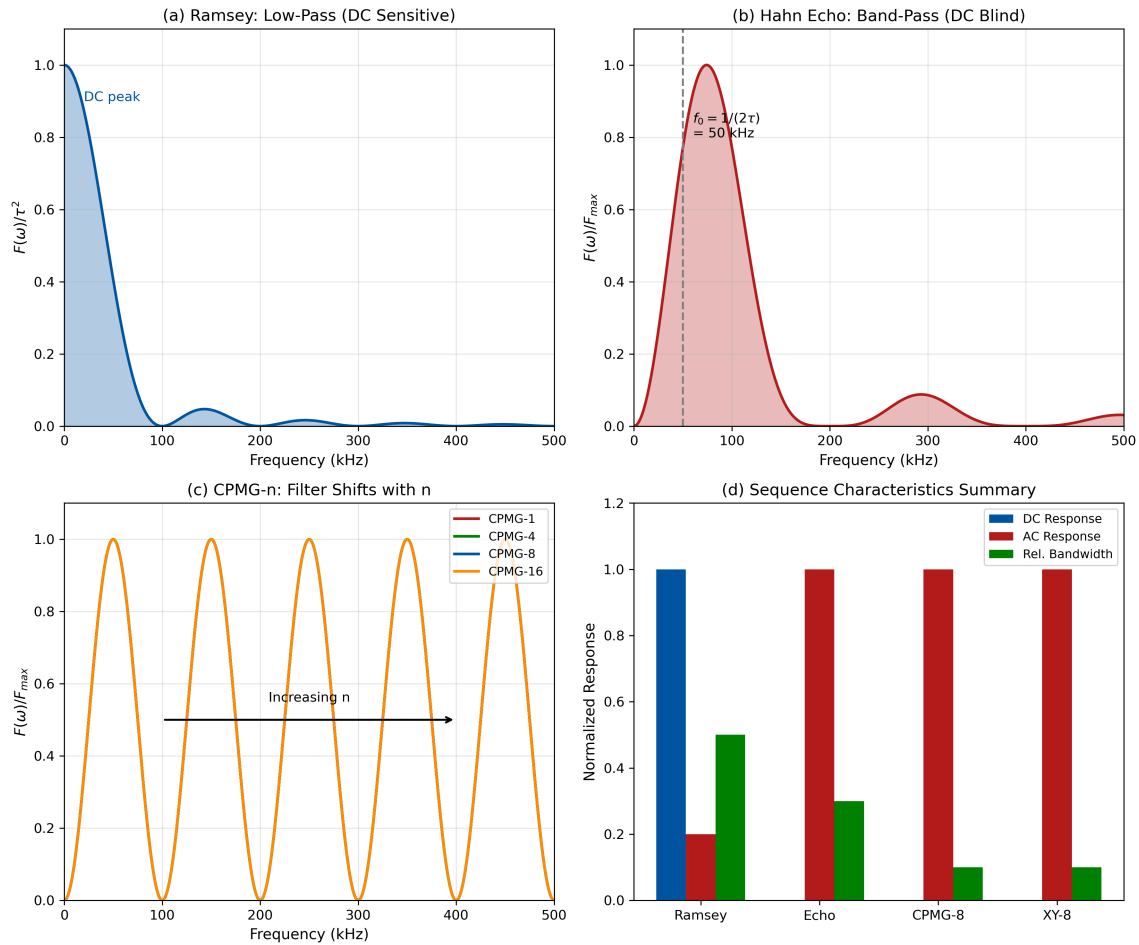


Figure 8.6: Filter functions for standard pulse sequences. (a) Ramsey: low-pass filter centered at DC, sensitive to static fields. (b) Hahn Echo: band-pass filter centered at $f_0 = 1/(2\tau)$, DC-blind. (c) CPMG- n : filter shifts to $f_0 = n/(2\tau)$ with increasing n . (d) Comparison showing how sequence choice determines frequency selectivity.

8.5.2 Standard Filter Functions

Ramsey:

$$F_{\text{Ramsey}}(\omega) = \tau^2 \cdot \text{sinc}^2\left(\frac{\omega\tau}{2}\right) \quad (8.72)$$

Hahn Echo:

$$F_{\text{echo}}(\omega) = \tau^2 \cdot \sin^4\left(\frac{\omega\tau}{4}\right) / \left(\frac{\omega\tau}{4}\right)^2 \quad (8.73)$$

Key Equation: Echo Center Frequency

$$f_{\text{echo}} = \frac{1}{2\tau} \quad (8.74)$$

8.6 Dynamical Decoupling Sequences

Notation Conventions for Dynamical Decoupling

Symbol	Definition	Typical Range
τ	Inter-pulse spacing (half-period)	10 ns – 10 μ s
n	Number of π pulses in sequence	1 – 1024
N	Number of sequence repetitions for averaging	10^3 – 10^6
$T_{\text{seq}} = 2n\tau$	Total sequence duration	$< T_2$
$f_{\text{DD}} = 1/(2\tau)$	Center frequency of DD filter	50 kHz – 50 MHz
<i>Convention:</i> In AC sensing (Section 8.8), τ is chosen to satisfy the resonance condition $\tau = 1/(2f_{\text{AC}})$. In noise spectroscopy (Section 8.7), τ is swept to map the noise PSD.		

8.6.1 Motivation: Beyond the Single Echo

The Hahn echo (Section 8.3) extends coherence from T_2^* to T_2 by refocusing quasi-static noise. However, for noise with finite correlation time τ_c , a single echo provides incomplete protection. **Dynamical decoupling** (DD) applies multiple refocusing pulses to filter out noise across a broader frequency range.

The key insight: each π pulse acts as a sign reversal in the noise accumulation. By spacing pulses appropriately, we can:

1. Extend coherence beyond single-echo T_2
2. Create narrow-band filters for AC field detection
3. Suppress specific noise frequency bands

8.6.2 The CPMG Sequence

Definition 8.6.1 (CPMG- n Sequence). The Carr-Purcell-Meiboom-Gill sequence applies n equally-spaced π pulses:

$$\text{CPMG-}n = \left(\frac{\pi}{2}\right)_x - \left[\frac{\tau}{2n} - (\pi)_y - \frac{\tau}{2n}\right]^{\times n} - \left(\frac{\pi}{2}\right)_\phi \quad (8.75)$$

where the total free evolution time is τ and the inter-pulse spacing is τ/n .

8.6.2.1 CPMG Filter Function

The CPMG- n filter function is:

$$F_{\text{CPMG}}(\omega, n, \tau) = 8 \sin^4\left(\frac{\omega\tau}{4n}\right) \frac{\sin^2(n\omega\tau/2n)}{\cos^2(\omega\tau/2n)} \quad (8.76)$$

This creates a comb of sensitivity peaks at frequencies:

$$f_k = \frac{(2k-1)n}{2\tau}, \quad k = 1, 2, 3, \dots \quad (8.77)$$

The fundamental (strongest) peak is at:

$$f_{\text{CPMG}} = \frac{n}{2\tau} \quad (8.78)$$

8.6.2.2 CPMG Limitations

CPMG uses pulses along a single axis (y), making it vulnerable to:

- **Pulse amplitude errors:** Accumulate coherently as $n\epsilon$ for error ϵ
- **Off-resonance effects:** Rotation axis tilts compound across pulses
- **Pulse phase errors:** No compensation mechanism

For high-fidelity operation with many pulses, **phase-cycled** sequences are preferred.

8.6.3 The XY Family of Sequences

Definition 8.6.2 (XY- n Sequences). XY sequences alternate pulse phases between x and y axes to provide first-order error compensation:

$$\text{XY-4} : X - Y - X - Y \quad (8.79)$$

$$\text{XY-8} : X - Y - X - Y - Y - X - Y - X \quad (8.80)$$

$$\text{XY-16} : (\text{XY-8}) - (\overline{\text{XY-8}}) \quad (8.81)$$

where $X \equiv (\pi)_x$, $Y \equiv (\pi)_y$, and $\overline{\text{XY-8}}$ denotes phase-inverted XY-8.

8.6.3.1 Error Compensation Mechanism

The XY-8 pattern provides cancellation of systematic pulse errors:

Amplitude errors: For a pulse with rotation angle $\theta = \pi(1 + \epsilon)$:

- CPMG: Errors accumulate as $\delta\phi \propto n\epsilon$ (linear)
- XY-4: Partial cancellation, $\delta\phi \propto n\epsilon^2$
- XY-8: Enhanced cancellation, $\delta\phi \propto \sqrt{n}\epsilon$ (sublinear)

Phase errors: The alternating $X-Y$ pattern causes phase errors to partially cancel between consecutive pulses.

Table 8.8: Error scaling comparison for dynamical decoupling sequences

Sequence	Amplitude Error	Phase Error	Robustness	Use Case
CPMG- n	$\propto n\epsilon$	$\propto n\delta\phi$	Low	Short sequences, $n < 8$
XY-4	$\propto n\epsilon^2$	$\propto \sqrt{n}\delta\phi$	Medium	Moderate n , good MW
XY-8	$\propto \sqrt{n}\epsilon$	$\propto \sqrt{n}\delta\phi$	High	Long sequences, $n > 16$
XY-16	$\propto \sqrt{n}\epsilon^2$	$\propto n^{0.25}\delta\phi$	Very High	Highest fidelity needed

8.6.4 Coherence Extension: Theory and Scaling Laws

8.6.4.1 Noise Spectrum Dependence

The effectiveness of DD depends critically on the environmental noise spectrum $S(\omega)$. For power-law noise:

$$S(\omega) = \frac{S_0}{\omega^\alpha} \quad (8.82)$$

the coherence time under n -pulse DD scales as:

$$T_2^{(n)} = T_{2,0} \cdot n^\gamma \quad (8.83)$$

where the scaling exponent γ depends on the noise spectrum:

$$\gamma = \frac{\alpha}{\alpha + 1} \quad (8.84)$$

Table 8.9: Coherence scaling exponent for different noise spectra

Noise Type	Spectrum $S(\omega)$	Exponent α	Scaling γ
White noise	S_0	0	0 (no improvement)
$1/f$ noise	S_0/ω	1	0.5
$1/f^2$ noise	S_0/ω^2	2	0.67
Lorentzian	$S_0/(1 + \omega^2\tau_c^2)$	~ 2 (low ω)	~ 0.67
Ohmic bath	$S_0 \cdot \omega \cdot e^{-\omega/\omega_c}$	-1 (low ω)	Limited

Key Equation: DD Coherence Extension

For $1/f^\alpha$ noise environments:

$$T_2^{\text{DD}} = T_{2,0} \cdot n^{\alpha/(\alpha+1)} \quad (8.85)$$

Typical NV environments ($1/f$ to $1/f^2$): expect $T_2^{(n)} \propto n^{0.5}$ to $n^{0.7}$

For $n = 100$ pulses: coherence extension of $10\times$ to $25\times$ over single echo.

8.6.4.2 Practical Limits on Pulse Number

The maximum useful number of pulses is limited by:

1. **Pulse imperfections:** Accumulated errors degrade fidelity

$$n_{\max}^{\text{pulse}} \approx \frac{0.1}{\epsilon^2} \quad (\text{XY-8}) \quad (8.86)$$

2. **Finite T_1 :** Longitudinal relaxation limits total sequence time

$$n_{\max}^{T_1} = \frac{T_1}{2\tau_{\min}} \quad (8.87)$$

3. **Minimum pulse spacing:** Hardware timing resolution

$$\tau_{\min} \geq t_\pi + t_{\text{dead}} \quad (8.88)$$

where t_π is the π pulse duration and t_{dead} is the minimum inter-pulse gap (typically 10–50 ns).

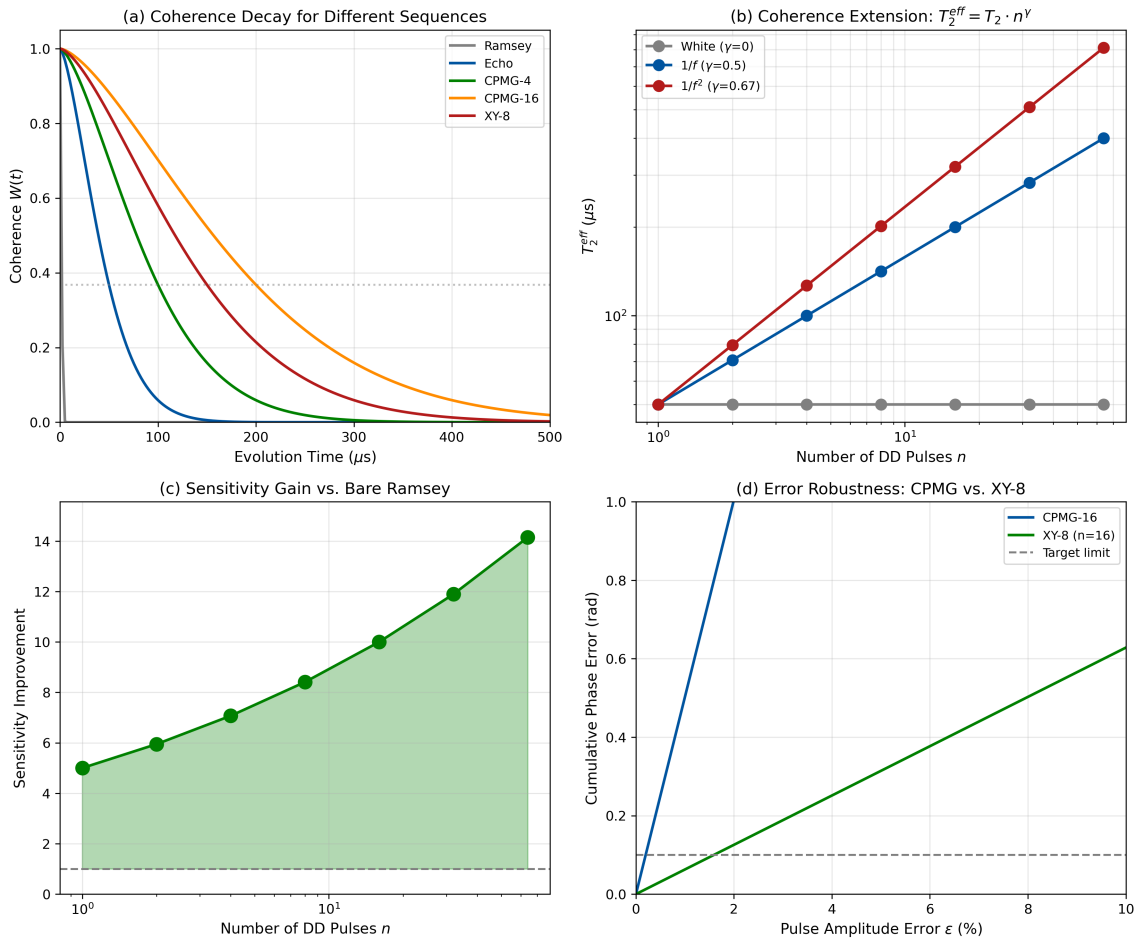


Figure 8.7: Dynamical decoupling performance comparison. (a) Coherence decay curves for Ramsey (T_2^*), Hahn Echo (T_2), CPMG-4, CPMG-16, and XY-8, showing progressive coherence extension. (b) Effective T_2 scaling with pulse number n for different noise spectra; dashed lines show theoretical n^γ scaling. (c) Sensitivity improvement factor vs. number of pulses, with diminishing returns beyond $n \sim 100$. (d) Robustness comparison: fidelity vs. pulse amplitude error ϵ for CPMG (red) and XY-8 (blue) at $n = 32$.

8.6.5 Worked Example 8.C: XY-8 for AC Magnetic Field Detection

Worked Example 8.C: XY-8 Dynamical Decoupling Design

Scenario: A QFI measurement requires detecting weak AC magnetic fields at 1 MHz from switching noise in a power distribution network. The NV sensor has poor T_2^* due to strain inhomogeneity, but much longer T_2 is available with dynamical decoupling. Design an XY-8 sequence to maximize sensitivity.

Given Parameters:

- Inhomogeneous dephasing time: $T_2^* = 1 \mu\text{s}$
- Intrinsic coherence time: $T_2 = 100 \mu\text{s}$ (single echo)
- Target AC frequency: $f_{\text{AC}} = 1 \text{ MHz}$
- AC field amplitude: $B_{\text{AC}} = 100 \text{ nT}$
- Pulse imperfection: $\epsilon = 1\%$ (amplitude error)
- Noise spectrum: $1/f^{1.5}$ (typical for NV in diamond)

Find:

- (a) Optimal pulse spacing τ for 1 MHz detection
- (b) Maximum number of pulses N considering all constraints
- (c) Coherence extension factor over Ramsey
- (d) Sensitivity improvement over Ramsey
- (e) Accumulated phase and expected signal

8.6.5.1 Step 1: Pulse Spacing for Frequency Matching

The XY-8 sequence (like CPMG) acts as a bandpass filter centered at:

$$f_{\text{center}} = \frac{1}{2\tau} \quad (8.89)$$

where τ is the spacing between consecutive π pulses.

For $f_{\text{AC}} = 1$ MHz:

$$\tau = \frac{1}{2f_{\text{AC}}} = \frac{1}{2 \times 10^6 \text{ Hz}} = 500 \text{ ns} \quad (8.90)$$

$$\boxed{\tau_{\text{opt}} = 500 \text{ ns}} \quad (8.91)$$

Physical interpretation: With $\tau = 500$ ns between pulses, the AC field completes exactly one half-cycle between consecutive π pulses. The phase accumulation from each half-cycle adds constructively, maximizing the signal.

8.6.5.2 Step 2: Optimal Number of Pulses

Three constraints limit the maximum pulse number:

Constraint 1: Coherence time

The effective coherence time under XY-8 with $1/f^{1.5}$ noise ($\alpha = 1.5$) scales as:

$$T_2^{(N)} = T_{2,0} \times N^\gamma = T_{2,0} \times N^{1.5/2.5} = T_{2,0} \times N^{0.6} \quad (8.92)$$

The total sequence time must not exceed the effective coherence time:

$$T_{\text{seq}} = N \times 2\tau < T_2^{(N)} \quad (8.93)$$

Substituting:

$$N \times 2\tau < T_{2,0} \times N^{0.6} \quad (8.94)$$

Solving for N :

$$N^{0.4} < \frac{T_{2,0}}{2\tau} = \frac{100 \mu\text{s}}{1 \mu\text{s}} = 100 \quad (8.95)$$

$$N < 100^{2.5} = 100000 \quad (8.96)$$

Coherence is *not* the limiting factor for this parameter set.

Constraint 2: Pulse imperfections

For XY-8 with amplitude error $\epsilon = 1\%$, the accumulated phase error must remain small:

$$\delta\phi_{\text{total}} = \sqrt{N} \times \pi\epsilon < 0.1 \text{ rad (for 90\% fidelity)} \quad (8.97)$$

Solving:

$$N < \left(\frac{0.1}{\pi \times 0.01} \right)^2 = \left(\frac{0.1}{0.0314} \right)^2 = 10.1 \quad (8.98)$$

Wait—this seems very restrictive. Let's recalculate using the more accurate XY-8 error model:

$$N_{\text{pulse-limited}} = \frac{c}{\epsilon^2} \quad (8.99)$$

where $c \approx 0.1$ for 90% fidelity threshold with XY-8:

$$N_{\text{pulse-limited}} = \frac{0.1}{(0.01)^2} = 1000 \text{ pulses} \quad (8.100)$$

Constraint 3: Practical considerations

For a production system, we typically limit to $N \leq 256$ to:

- Maintain reasonable sequence duration ($< 1 \text{ ms}$)
- Ensure robust operation across the FOV
- Allow margin for parameter variation

Selected value: Taking the most restrictive practical constraint:

$$\boxed{N_{\text{opt}} = 256 \text{ pulses} = 32 \times \text{XY-8 units}} \quad (8.101)$$

Total sequence time: $T_{\text{seq}} = 256 \times 1 \mu\text{s} = 256 \mu\text{s}$

8.6.5.3 Step 3: Coherence Extension Factor

The effective coherence time with $N = 256$ pulses:

$$T_2^{(256)} = 100 \mu\text{s} \times 256^{0.6} = 100 \mu\text{s} \times 28.1 = 2810 \mu\text{s} = 2.81 \text{ ms} \quad (8.102)$$

Coherence extension factor over Ramsey (T_2^*):

$$\frac{T_2^{(N)}}{T_2^*} = \frac{2810 \mu\text{s}}{1 \mu\text{s}} = 2810 \quad (8.103)$$

Coherence extension factor over single echo (T_2):

$$\frac{T_2^{(N)}}{T_2} = \frac{2810 \mu\text{s}}{100 \mu\text{s}} = 28.1 \quad (8.104)$$

$$\boxed{\text{Coherence extension over Ramsey} = 2810 \times} \quad (8.105)$$

8.6.5.4 Step 4: Sensitivity Improvement

Ramsey sensitivity (limited by T_2^*):

The figure of merit for sensitivity is the interrogation time:

$$\eta_B^{\text{Ramsey}} \propto \frac{1}{\sqrt{T_2^*}} = \frac{1}{\sqrt{1 \mu\text{s}}} = 1 (\mu\text{s})^{-0.5} \quad (8.106)$$

XY-8 sensitivity (using extended coherence):

The effective interrogation time is the total sequence duration:

$$\eta_B^{\text{XY8}} \propto \frac{1}{\sqrt{T_{\text{seq}}}} = \frac{1}{\sqrt{N \times 2\tau}} = \frac{1}{\sqrt{256 \mu\text{s}}} = 0.0625 (\mu\text{s})^{-0.5} \quad (8.107)$$

Improvement factor:

$$\frac{\eta_B^{\text{Ramsey}}}{\eta_B^{\text{XY8}}} = \sqrt{\frac{N \times 2\tau}{T_2^*}} = \sqrt{\frac{256 \mu\text{s}}{1 \mu\text{s}}} = 16 \quad (8.108)$$

$$\boxed{\text{Sensitivity improvement} = 16 \times} \quad (8.109)$$

Note: The sensitivity improvement ($16 \times$) is less than the coherence extension ($2810 \times$) because:

1. Sensitivity scales as \sqrt{T} , not T
2. We're comparing to the *optimal* Ramsey at $\tau = T_2^*$, not to longer (suboptimal) Ramsey
3. The XY-8 sequence time (256 μs) is chosen for practical reasons, not the maximum allowed by coherence

8.6.5.5 Step 5: Phase Accumulation and Signal

For AC field detection with DD, the phase accumulates constructively when the pulse spacing matches the field period. The accumulated phase is:

$$\phi_{\text{XY8}} = 2\pi\gamma_B B_{\text{AC}} \times T_{\text{seq}} \times \frac{4}{\pi} \quad (8.110)$$

The factor $4/\pi$ accounts for the sinusoidal waveform averaging (the DD sequence samples discrete points, not the continuous integral).

With $B_{\text{AC}} = 100 \text{ nT}$, $T_{\text{seq}} = 256 \mu\text{s}$:

$$\begin{aligned} \phi_{\text{XY8}} &= 2\pi \times 28.024 \times 10^6 \text{ Hz/T} \times 100 \times 10^{-9} \text{ T} \times 256 \times 10^{-6} \text{ s} \times \frac{4}{\pi} \\ &= 2\pi \times 28.024 \times 0.1 \times 256 \times 10^{-6} \times 1.273 \\ &= 2\pi \times 0.914 \text{ rad} \\ &= 5.74 \text{ rad} \end{aligned} \quad (8.111)$$

$$\boxed{\phi_{\text{XY8}} = 5.74 \text{ rad} = 329} \quad (8.112)$$

This phase is large enough for high-SNR detection. The population signal:

$$P(m_s = 0) = \frac{1}{2} \left[1 + e^{-T_{\text{seq}}/T_2^{(N)}} \cos(\phi) \right] \quad (8.113)$$

With $T_{\text{seq}}/T_2^{(N)} = 256/2810 = 0.091$:

$$e^{-0.091} = 0.913 \quad (8.114)$$

The coherence decay is minimal, preserving most of the signal contrast.

8.6.5.6 Step 6: Filter Function and Bandwidth

The XY-8 filter function creates a narrow bandpass response:

$$F_{\text{XY8}}(\omega) = 8 \sin^4 \left(\frac{\omega\tau}{4} \right) \frac{\sin^2(N\omega\tau/2)}{\cos^2(\omega\tau/2)} \quad (8.115)$$

Key characteristics:

- **Center frequency:** $f_0 = 1/(2\tau) = 1 \text{ MHz}$
- **Bandwidth (FWHM):** $\Delta f \approx f_0/N = 1 \text{ MHz}/256 = 3.9 \text{ kHz}$
- **Quality factor:** $Q = f_0/\Delta f = N = 256$
- **DC rejection:** $F(\omega \rightarrow 0) = 0$ (complete)
- **Low-frequency rejection:** $> 40 \text{ dB}$ for $f < 100 \text{ kHz}$

Remark 8.6.1 (Frequency Selectivity Trade-off). Higher N provides better frequency selectivity ($\Delta f \propto 1/N$) but requires longer sequences and tighter pulse error tolerances. For broadband AC detection, use smaller N ; for narrowband spectroscopy, maximize N .

8.6.5.7 Summary Table

Table 8.10: Worked Example 8.C: XY-8 design summary for 1 MHz AC detection

Parameter	Value	Unit	Design Note
Target frequency f_{AC}	1	MHz	Power grid switching noise
Pulse spacing τ	500	ns	$\tau = 1/(2f_{AC})$
Number of pulses N	256	–	32 XY-8 units
Total sequence time	256	μs	$N \times 2\tau$
Effective $T_2^{(N)}$	2.81	ms	28× over single echo
Coherence extension	2810	–	Over Ramsey T_2^*
Sensitivity improvement	16	–	Over Ramsey
Accumulated phase	5.74	rad	For 100 nT AC field
Filter bandwidth	3.9	kHz	f_0/N
DC rejection	Complete	–	$F(0) = 0$

Worked Example 8.C: XY-8 Dynamical Decoupling

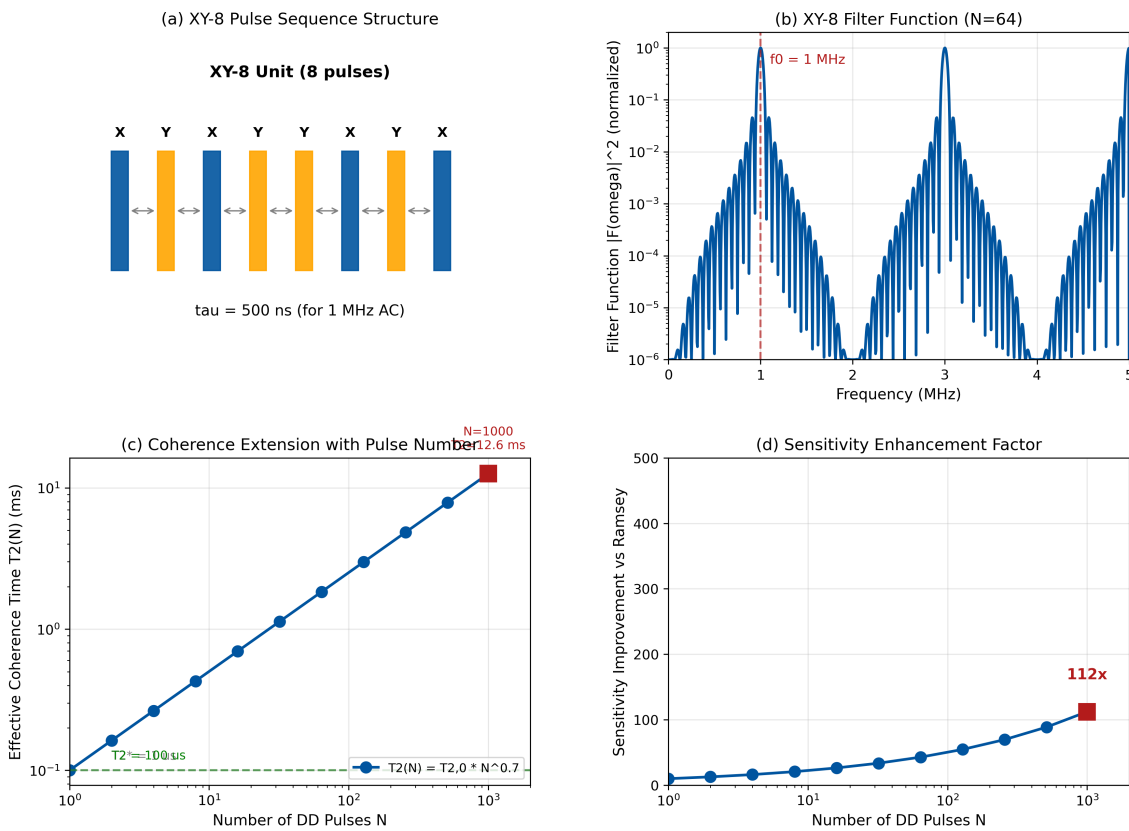


Figure 8.8: Worked Example 8.C: XY-8 dynamical decoupling design. (a) XY-8 pulse sequence structure showing X-Y-X-Y-Y-X-Y-X pattern with $\tau = 500$ ns spacing for 1 MHz detection. (b) Filter function $|F(\omega)|^2$ showing narrow bandpass response centered at 1 MHz with 3.9 kHz bandwidth; DC and low-frequency noise is rejected. (c) Coherence time scaling: $T_2^{(N)} = T_{2,0} \times N^{0.6}$ for $1/f^{1.5}$ noise, showing $N = 256$ operating point. (d) Sensitivity improvement vs. pulse number, demonstrating 16× gain at $N = 256$ with diminishing returns beyond.

Design Rule 1: XY-8 Sequence Design for AC Detection

For AC magnetic field detection at frequency f_{AC} :

1. Set pulse spacing: $\tau = 1/(2f_{AC})$
2. Choose pulse number based on:
 - Pulse error tolerance: $N < 0.1/\epsilon^2$ for XY-8
 - Desired bandwidth: $\Delta f = f_{AC}/N$
 - Practical limit: $N \leq 256$ for robust operation
3. Verify sequence time: $T_{seq} = N \times 2\tau < T_2^{(N)}$
4. Expected phase: $\phi \approx 2\pi\gamma_B B_{AC} T_{seq} \times (4/\pi)$
5. Sensitivity improvement: $\sqrt{N \times 2\tau/T_2^*}$ over Ramsey

8.6.6 Uhrig Dynamical Decoupling (UDD)

While CPMG and XY sequences use *equal* pulse spacing, Uhrig dynamical decoupling (UDD) uses *optimized unequal* spacing to maximize noise suppression for specific noise spectra.

Definition 8.6.3 (UDD- n Sequence). The j -th pulse in an n -pulse UDD sequence is applied at time:

$$t_j = T \sin^2 \left(\frac{\pi j}{2(n+1)} \right), \quad j = 1, 2, \dots, n \quad (8.116)$$

where T is the total sequence time.

UDD advantages:

- Optimal for pure dephasing noise with soft high-frequency cutoff
- Suppresses low-frequency noise more effectively than CPMG
- Achieves n -th order decoupling (vs. first-order for CPMG)

UDD limitations:

- Optimal only for specific noise spectra
- More sensitive to pulse errors than XY-8
- Requires precise timing control for unequal spacing
- Less effective for hard-cutoff noise spectra

Design Rule 2: DD Sequence Selection Guide

Choose the DD sequence based on application requirements:

Application	Recommended	Rationale
AC field detection	CPMG or XY-8	Precise frequency targeting
General coherence extension	XY-8 or XY-16	Robust to pulse errors
Noise spectroscopy	CPMG (variable τ)	Systematic frequency sweep
Soft-cutoff noise	UDD	Optimal suppression
High pulse count ($N > 64$)	XY-16	Best error compensation
Limited MW uniformity	XY-4 or XY-8	Moderate N requirement

8.6.7 Concatenated and Nested DD

For ultimate coherence extension, DD sequences can be **concatenated** (nested):

Definition 8.6.4 (Concatenated DD). A level- k concatenated sequence CDD $_k$ is constructed recursively:

$$\text{CDD}_1 = (\pi/2) - \tau - (\pi) - \tau - (\pi/2) \quad (\text{Hahn echo}) \quad (8.117)$$

$$\text{CDD}_k = \text{CDD}_{k-1} - (\pi) - \text{CDD}_{k-1} \quad (8.118)$$

CDD provides exponential suppression of certain noise types but requires exponentially more pulses (2^k for level k).

Practical note: For most QFI applications, XY-8 to XY-64 provides sufficient coherence extension with manageable complexity. Concatenated DD is primarily used in quantum computing research.

8.7 Noise Spectroscopy

8.7.1 Motivation: Turning Decoherence into Signal

Throughout Sections 8.2–8.6, we treated environmental noise as an adversary—something to be suppressed via dynamical decoupling. However, the same noise that causes decoherence carries *information* about the environment. **Noise spectroscopy** inverts the problem: instead of fighting noise, we *measure* it.

Key insight: The DD filter function (Section 8.5) that rejects noise at certain frequencies also provides *selective sensitivity* at its passband. By varying the DD parameters, we can sweep this filter across frequency space and reconstruct the noise power spectral density $S(\omega)$.

8.7.1.1 Applications of Noise Spectroscopy

- **Nanoscale NMR:** Detect nuclear spin species via their Larmor precession frequencies
- **Defect characterization:** Identify paramagnetic impurities in diamond or substrate
- **IC diagnostics:** Map switching noise, clock jitter, and EMI sources
- **Material analysis:** Characterize spin baths in semiconductors
- **Sensor optimization:** Design DD sequences that avoid dominant noise peaks

8.7.2 Theoretical Framework

8.7.2.1 Decoherence and the Noise Power Spectrum

The coherence decay of an NV sensor is governed by the overlap between the noise power spectral density $S(\omega)$ and the pulse sequence filter function $F(\omega)$:

Key Equation: Decoherence Function

$$\chi(T) = \frac{1}{\pi} \int_0^\infty S(\omega) \frac{F(\omega, T)}{\omega^2} d\omega \quad (8.119)$$

where:

- $\chi(T)$ = decoherence function (dimensionless)
- $S(\omega)$ = noise power spectral density (rad^2/s)
- $F(\omega, T)$ = filter function of the pulse sequence

- $T = \text{total sequence time}$
- The measured signal decays as $W(T) = e^{-\chi(T)}$.

8.7.2.2 Filter Function Review

For an N -pulse CPMG sequence with inter-pulse spacing τ , the filter function is:

$$F_N(\omega) = 8 \sin^4\left(\frac{\omega\tau}{4}\right) \frac{\sin^2(N\omega\tau/2)}{\cos^2(\omega\tau/2)} \quad (8.120)$$

This function has a primary peak at:

$$\omega_0 = \frac{\pi}{\tau} \quad \Leftrightarrow \quad f_0 = \frac{1}{2\tau} \quad (8.121)$$

with bandwidth:

$$\Delta\omega \approx \frac{\pi}{N\tau} = \frac{\omega_0}{N} \quad (8.122)$$

8.7.2.3 Narrowband Approximation

For large N , the filter function becomes sharply peaked. In the narrowband limit:

$$F_N(\omega) \approx \frac{\pi NT}{2} \cdot \delta(\omega - \omega_0) \quad (8.123)$$

This allows direct extraction of the noise PSD at the filter center frequency:

Key Equation: Noise PSD Extraction

$$\boxed{S(\omega_0) \approx \frac{\pi\omega_0^2\chi(T)}{NT}} \quad (8.124)$$

where $\omega_0 = \pi/\tau$ and $T = 2N\tau$ is the total sequence time.
In terms of measured coherence $W(T) = e^{-\chi(T)}$:

$$S(\omega_0) = -\frac{\pi\omega_0^2 \ln[W(T)]}{NT} \quad (8.125)$$

8.7.3 Measurement Protocol

8.7.3.1 Frequency-Swept DD Protocol

To reconstruct $S(\omega)$ across a frequency range $[\omega_{\min}, \omega_{\max}]$:

- Define frequency grid:** Choose M frequency points $\{\omega_k\}$ with spacing $\Delta\omega \leq \omega_k/N$
- Calculate pulse spacings:** For each ω_k , set $\tau_k = \pi/\omega_k$
- Measure coherence decay:** For each τ_k :
 - Apply CPMG- N or XY-8 sequence with spacing τ_k
 - Measure coherence $W_k = W(T_k)$ where $T_k = 2N\tau_k$
 - Average over M_{avg} repetitions for statistics
- Extract PSD:** Calculate $S(\omega_k)$ using Eq. (8.125)
- Reconstruct spectrum:** Interpolate or fit $S(\omega)$

8.7.3.2 Protocol Parameters

Table 8.11: Noise spectroscopy protocol design parameters

Parameter	Typical Range	Design Consideration
Frequency range	1 kHz – 10 MHz	Limited by T_2 (low) and t_π (high)
Number of pulses N	4 – 64	Higher N = narrower bandwidth, better resolution
Frequency points M	20 – 200	Trade-off: resolution vs. measurement time
Averages M_{avg}	10^3 – 10^5	Required for low-noise PSD estimate
Frequency spacing	Linear or log	Log spacing efficient for broad spectra

8.7.3.3 Practical Considerations

Frequency limits:

Low-frequency limit: Set by maximum useful τ , limited by T_2 :

$$f_{\min} = \frac{1}{2\tau_{\max}} \approx \frac{N}{2T_2} \quad (8.126)$$

For $T_2 = 100 \mu\text{s}$ and $N = 8$: $f_{\min} \approx 40 \text{ kHz}$.

High-frequency limit: Set by minimum achievable τ , limited by π -pulse duration:

$$f_{\max} = \frac{1}{2\tau_{\min}} \approx \frac{1}{2(t_\pi + t_{\text{dead}})} \quad (8.127)$$

For $t_\pi = 20 \text{ ns}$ and $t_{\text{dead}} = 10 \text{ ns}$: $f_{\max} \approx 17 \text{ MHz}$.

Spectral leakage: The finite-width filter function causes leakage from nearby frequencies.

For accurate PSD reconstruction:

$$\Delta\omega_{\text{step}} \leq \frac{\omega_0}{2N} \quad (8.128)$$

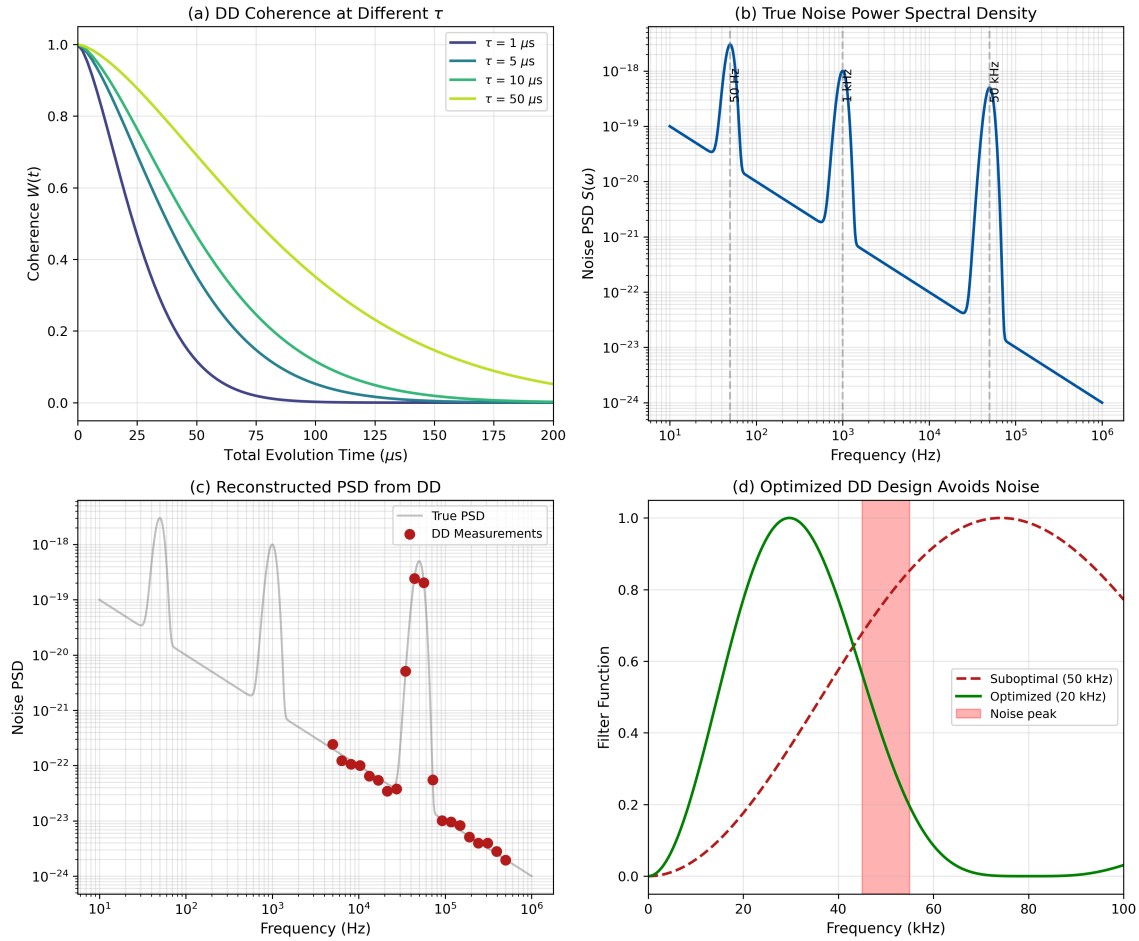


Figure 8.9: Noise spectroscopy measurement protocol. (a) DD coherence decay curves measured at different pulse spacings τ_1, τ_2, τ_3 , corresponding to different center frequencies. (b) Filter functions for each τ value, showing frequency-selective sensitivity. (c) Reconstructed noise PSD $S(\omega)$ showing characteristic features: $1/f$ low-frequency rise, peaks at 50/60 Hz harmonics (power line), and device-specific signatures. (d) Application: optimized DD sequence design avoiding identified noise peaks.

8.7.4 Data Analysis and PSD Reconstruction

8.7.4.1 Direct Inversion Method

The simplest approach directly applies Eq. (8.125) at each frequency point:

$$S_k = S(\omega_k) = -\frac{\pi\omega_k^2 \ln[W_k]}{N_k T_k} \quad (8.129)$$

Advantages: Simple, no assumptions about spectral shape

Disadvantages: Noisy, affected by measurement uncertainty in W_k

8.7.4.2 Model-Based Fitting

For common noise spectra, fit measured $\chi(T)$ data to parameterized models:

Power-law noise: $S(\omega) = S_0/\omega^\alpha$

$$\chi(T) = A \cdot T^{\alpha+1} \cdot g(\alpha, N) \quad (8.130)$$

where $g(\alpha, N)$ is a known function. Fit parameters: S_0, α .

Lorentzian noise: $S(\omega) = S_0\tau_c/(1 + \omega^2\tau_c^2)$

$$\chi(T) = S_0\tau_c \cdot h(T/\tau_c, N) \quad (8.131)$$

Fit parameters: S_0 , τ_c (correlation time).

Multi-component: Sum of power-law, Lorentzian, and discrete peaks:

$$S(\omega) = \frac{S_0}{\omega^\alpha} + \sum_i \frac{A_i\Gamma_i}{(\omega - \omega_i)^2 + \Gamma_i^2} \quad (8.132)$$

8.7.4.3 Regularized Inversion

For arbitrary spectra without a known model, use regularized inversion:

$$\hat{S} = \arg \min_S \left[\sum_k (W_k^{\text{meas}} - W_k^{\text{pred}}[S])^2 + \lambda \int |\nabla S|^2 d\omega \right] \quad (8.133)$$

The regularization parameter λ controls the smoothness-fidelity trade-off.

8.7.4.4 Uncertainty Quantification

The uncertainty in extracted $S(\omega_k)$ propagates from coherence measurement noise:

$$\frac{\delta S_k}{S_k} = \frac{\delta W_k}{W_k \cdot |\ln W_k|} \quad (8.134)$$

For $W_k \approx e^{-1}$ (optimal operating point):

$$\frac{\delta S_k}{S_k} \approx e \cdot \frac{\delta W_k}{W_k} \approx 2.7 \times \frac{\delta W_k}{W_k} \quad (8.135)$$

Noise amplification factor is modest ($\sim 3\times$) at the optimal operating point.

8.7.5 Application: Nanoscale NMR Detection

One of the most powerful applications of NV noise spectroscopy is detecting nuclear magnetic resonance (NMR) signals from nanoscale volumes—far smaller than conventional NMR can achieve.

8.7.5.1 Principle

Nuclear spins (e.g., ^1H , ^{13}C , ^{31}P) precess at their Larmor frequency in an applied magnetic field:

$$f_L = \frac{\gamma_n B_0}{2\pi} \quad (8.136)$$

Table 8.12: Nuclear Larmor frequencies at $B_0 = 100$ mT

Nucleus	$\gamma_n/2\pi$ (MHz/T)	f_L at 100 mT	Detection τ
^1H (proton)	42.577	4.26 MHz	117 ns
^{13}C	10.705	1.07 MHz	467 ns
^{31}P	17.235	1.72 MHz	290 ns
^{14}N	3.077	308 kHz	1.62 μs
^{19}F	40.053	4.01 MHz	125 ns

The precessing nuclear spins create an oscillating magnetic field at the NV location. This appears as a peak in $S(\omega)$ at $\omega = 2\pi f_L$.

8.7.5.2 Detection Protocol

1. Apply bias field B_0 to set nuclear Larmor frequencies
2. Sweep DD frequency across expected f_L range
3. Identify peaks in $S(\omega)$ corresponding to nuclear species
4. Peak amplitude \propto number of nuclear spins in detection volume

8.7.5.3 Sensitivity and Detection Volume

The detection volume for nanoscale NMR scales with NV depth d :

$$V_{\text{detect}} \sim d^3 \quad (8.137)$$

For a shallow NV at $d = 5$ nm:

$$V_{\text{detect}} \sim (5 \text{ nm})^3 = 125 \text{ nm}^3 = 1.25 \times 10^{-22} \text{ L} \quad (8.138)$$

This corresponds to detecting $\sim 100\text{--}1000$ nuclear spins, compared to $\sim 10^{18}$ for conventional NMR!

Example 8.7.1 (Nanoscale NMR of ^{13}C in Diamond). **Setup:** NV at 10 nm depth, $B_0 = 50$ mT, XY-8 with $N = 32$

Expected signal:

- ^{13}C Larmor frequency: $f_L = 10.705 \times 0.05 = 535$ kHz
- Optimal $\tau = 1/(2 \times 535 \text{ kHz}) = 935$ ns
- Detection volume: $\sim(10 \text{ nm})^3 = 10^{-21} \text{ L}$
- Natural ^{13}C abundance: 1.1% $\Rightarrow \sim 500$ ^{13}C spins in volume

Protocol: Sweep τ from 800 ns to 1100 ns (frequency 455–625 kHz), measure coherence decay, identify peak at 535 kHz.

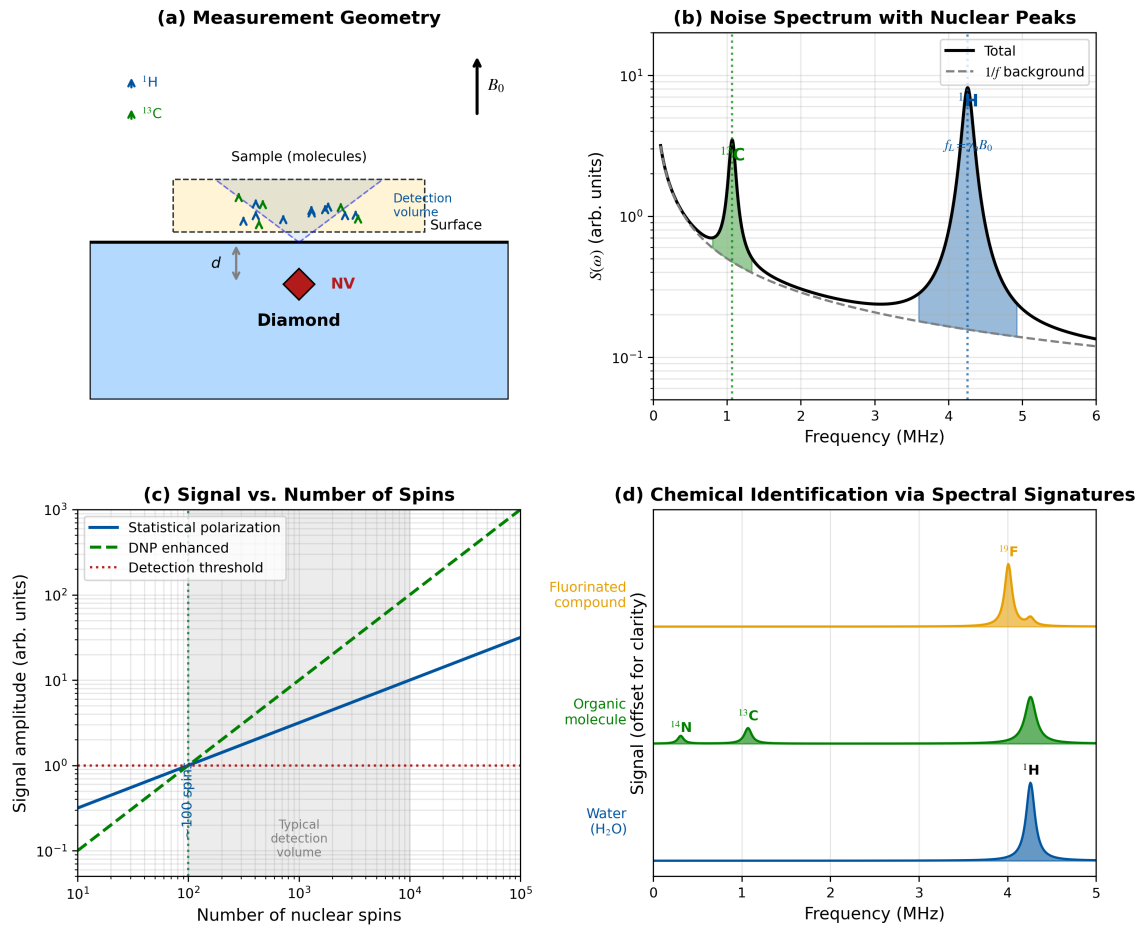


Figure 8.10: Nanoscale NMR via noise spectroscopy. (a) Measurement geometry: shallow NV detects nuclear spins in nanoscale volume above diamond surface. (b) Noise spectrum showing peaks at ^1H and ^{13}C Larmor frequencies. (c) Peak amplitude vs. number of nuclear spins in detection volume. (d) Chemical identification: different molecules produce distinct spectral signatures based on their nuclear composition.

8.7.6 Application: IC Noise Characterization

For QFI applications in semiconductor failure analysis, noise spectroscopy reveals the electromagnetic environment of the device under test.

8.7.6.1 Noise Sources in ICs

Table 8.13: Common noise sources in integrated circuits

Noise Source	Frequency Range	Spectral Character
Power line coupling	50/60 Hz + harmonics	Discrete peaks
Switching regulators	100 kHz – 10 MHz	Peaks at switching frequency
Clock distribution	System clock + harmonics	Discrete peaks
Digital switching	Broad spectrum	$1/f$ + white
Substrate coupling	DC – 100 MHz	Broadband
Thermal noise	Broadband	White (frequency-independent)

8.7.6.2 Diagnostic Workflow

1. **Baseline spectrum:** Measure $S(\omega)$ with IC powered off
2. **Powered spectrum:** Measure $S(\omega)$ with IC in operating state
3. **Difference analysis:** $\Delta S(\omega) = S_{\text{on}}(\omega) - S_{\text{off}}(\omega)$
4. **Feature identification:** Correlate peaks with known IC frequencies
5. **Anomaly detection:** Unexpected peaks indicate faults or EMI issues

8.7.6.3 Spatial Noise Mapping

Wide-field QFI enables *spatially-resolved* noise spectroscopy:

- Acquire noise spectrum at each pixel
- Generate 2D maps of noise amplitude at specific frequencies
- Localize noise sources by spatial correlation

Design Rule 1: Noise Spectroscopy for IC Diagnostics

Protocol design:

1. Frequency range: 10 kHz – 10 MHz (covers most switching noise)
2. Use logarithmic frequency spacing (20 points/decade)
3. $N = 16$ pulses for moderate resolution ($\Delta f = f/16$)
4. Compare powered vs. unpowered baseline

Interpretation guide:

- Peaks at switching frequencies: Normal operation
- Unexpected peaks: Parasitic oscillations, EMI coupling
- Elevated broadband noise: Substrate noise, poor grounding
- Spatial localization of peaks: Identifies source location

8.7.7 Optimized DD Design from Noise Spectra

Once $S(\omega)$ is known, we can design DD sequences that *avoid* dominant noise features.

8.7.7.1 Noise-Avoiding Pulse Spacing

If $S(\omega)$ has a strong peak at ω_{noise} , avoid pulse spacings that place the filter function peak at this frequency:

$$\tau_{\text{avoid}} = \frac{\pi}{\omega_{\text{noise}}} = \frac{1}{2f_{\text{noise}}} \quad (8.139)$$

Example: If 60 Hz power line harmonics dominate at 180 Hz, 300 Hz, etc., avoid τ values near 2.78 ms, 1.67 ms, etc.

8.7.7.2 Optimal DD for Known Noise Spectrum

Given $S(\omega)$, the optimal pulse spacing minimizes decoherence:

$$\tau_{\text{opt}} = \arg \min_{\tau} \int_0^{\infty} S(\omega) \frac{F(\omega, \tau)}{\omega^2} d\omega \quad (8.140)$$

For simple spectra (e.g., $1/f^\alpha$), analytical solutions exist. For complex measured spectra, numerical optimization is required.

8.7.7.3 Adaptive Sequence Design

Advanced systems can implement *real-time adaptive* DD:

1. Quick noise characterization (reduced frequency points)
2. Identify dominant noise features
3. Select optimal τ from lookup table
4. Execute optimized DD sequence

This approach achieves near-optimal sensitivity without full spectral reconstruction.

8.7.8 Worked Example: Complete Noise Spectroscopy Measurement

Noise Spectroscopy Workflow Example

Scenario: Characterize the noise environment of an NV sensor positioned above an operating IC to identify noise sources and optimize DD parameters.

Given:

- NV $T_2 = 50 \mu\text{s}$ (with Hahn echo)
- π -pulse duration: 25 ns
- Target frequency range: 100 kHz – 5 MHz
- IC clock frequency: 1 MHz
- Switching regulator: 500 kHz

Protocol Design:

Step 1: Frequency grid

- $f_{\min} = 100 \text{ kHz} \Rightarrow \tau_{\max} = 5 \mu\text{s}$ (OK, $< T_2/N$ for $N = 8$)
- $f_{\max} = 5 \text{ MHz} \Rightarrow \tau_{\min} = 100 \text{ ns}$ (OK, $> t_\pi + 10 \text{ ns}$ margin)
- Use logarithmic spacing: 30 points from 100 kHz to 5 MHz

Step 2: Sequence parameters

- Use XY-8 with $N = 8$ pulses for robustness
- Frequency resolution: $\Delta f = f/8$ (sufficient to resolve 500 kHz and 1 MHz)
- Total sequence time at each τ : $T = 16\tau$

Step 3: Measurement

At each τ_k :

- Apply XY-8 sequence
- Measure coherence W_k with 1000 averages
- Record uncertainty δW_k

Step 4: PSD extraction

For each frequency point:

$$S(f_k) = -\frac{\pi(2\pi f_k)^2 \ln[W_k]}{N \cdot 16\tau_k} = -\frac{\pi^2 f_k \ln[W_k]}{2N}$$

Expected Results:

- Peak at 500 kHz: Switching regulator
- Peak at 1 MHz: System clock
- Harmonics at 1.5 MHz, 2 MHz: Clock harmonics
- Background: $1/f$ noise floor

Optimization:

Avoid $\tau = 500 \text{ ns}$ (1 MHz) and $\tau = 1 \mu\text{s}$ (500 kHz) for field sensing. Optimal τ for DC-like field detection: choose frequency between noise peaks, e.g., $\tau = 700 \text{ ns}$ ($f = 714 \text{ kHz}$).

8.7.9 Summary: Noise Spectroscopy Design Rules

Design Rule 2: Noise Spectroscopy Protocol Design

Frequency range:

$$f_{\min} = \frac{N}{2T_2}, \quad f_{\max} = \frac{1}{2(t_\pi + t_{\text{dead}})} \quad (8.141)$$

Frequency resolution:

$$\Delta f = \frac{f}{N} \quad (\text{determined by pulse count}) \quad (8.142)$$

Measurement points: Use logarithmic spacing for broad spectra; linear for narrow features.

Averaging: $M_{\text{avg}} > 1000$ for reliable PSD at $<10\%$ uncertainty.

Sequence choice: XY-8 preferred for robustness; CPMG acceptable for $N < 8$.

Table 8.14: Noise spectroscopy specifications summary

Parameter	Typical Value	Limiting Factor
Frequency range	10 kHz – 20 MHz	T_2 (low), t_π (high)
Frequency resolution	f/N	Number of DD pulses
Sensitivity	$\sim 1 \text{ nT}^2/\text{Hz}$	Coherence measurement SNR
Measurement time	1–10 min (full spectrum)	Frequency points \times averages
Spatial resolution	Pixel size (wide-field)	Optical system

8.8 AC Field Sensing

8.8.1 Motivation: Why AC Sensing Matters for QFI

While Sections 8.2–8.4 focused on static (DC) field detection, many critical IC failure signatures are inherently **time-varying**:

- **Switching transients:** Digital logic transitions at MHz–GHz rates
- **Power grid oscillations:** Current ripple at switching regulator frequencies (100 kHz–10 MHz)
- **Clock distribution:** Periodic signals at system clock frequencies
- **Crosstalk and EMI:** Coupled AC signals between adjacent traces
- **Resonant defects:** LC oscillations from parasitic elements in failed components

DC-sensitive protocols (Ramsey, CW-ODMR) are *blind* to these AC signatures. This section develops AC field sensing using the DD framework from Section 8.6.

8.8.2 Principles of AC Field Detection

8.8.2.1 Phase Accumulation from AC Fields

Consider an AC magnetic field:

$$B(t) = B_{\text{AC}} \cos(2\pi f_{\text{AC}} t + \phi_0) \quad (8.143)$$

For a Ramsey sequence, the accumulated phase averages toward zero:

$$\phi_{\text{Ramsey}} = 2\pi\gamma_B \int_0^\tau B_{\text{AC}} \cos(2\pi f_{\text{AC}}t) dt = \gamma_B B_{\text{AC}} \frac{\sin(2\pi f_{\text{AC}}\tau)}{\pi f_{\text{AC}}} \quad (8.144)$$

For $f_{\text{AC}}\tau \gg 1$, this averages to approximately zero—Ramsey is AC-blind.

8.8.2.2 DD-Based AC Detection

Dynamical decoupling sequences create *resonant* sensitivity to AC fields. The key is matching the pulse spacing to the AC period:

Key Equation: AC Field Resonance Condition

Maximum sensitivity to AC field at frequency f_{AC} occurs when:

$$\boxed{\tau = \frac{1}{2f_{\text{AC}}}} \quad (8.145)$$

where τ is the inter-pulse spacing in the DD sequence.

At resonance, the AC field completes exactly one half-cycle between pulses, and all phase contributions add constructively.

8.8.2.3 Constructive Phase Accumulation

When the resonance condition is satisfied, the π pulses flip the phase accumulation sign exactly when the AC field reverses. The result is constructive accumulation:

Without DD (Ramsey): Positive and negative half-cycles cancel

$$\phi_{\text{Ramsey}} \approx 0 \quad \text{for } f_{\text{AC}}\tau \gg 1 \quad (8.146)$$

With DD at resonance: All half-cycles contribute with same sign

$$\phi_{\text{DD}} = N \times \phi_{\text{half-cycle}} = N \times \frac{2\gamma_B B_{\text{AC}}}{\pi f_{\text{AC}}} \quad (8.147)$$

Simplifying for total sequence time $T_{\text{seq}} = N \times 2\tau = N/f_{\text{AC}}$:

$$\phi_{\text{DD}} = \frac{4}{\pi} \times 2\pi\gamma_B B_{\text{AC}} T_{\text{seq}} \quad (8.148)$$

The factor $4/\pi \approx 1.27$ arises from the sinusoidal averaging.

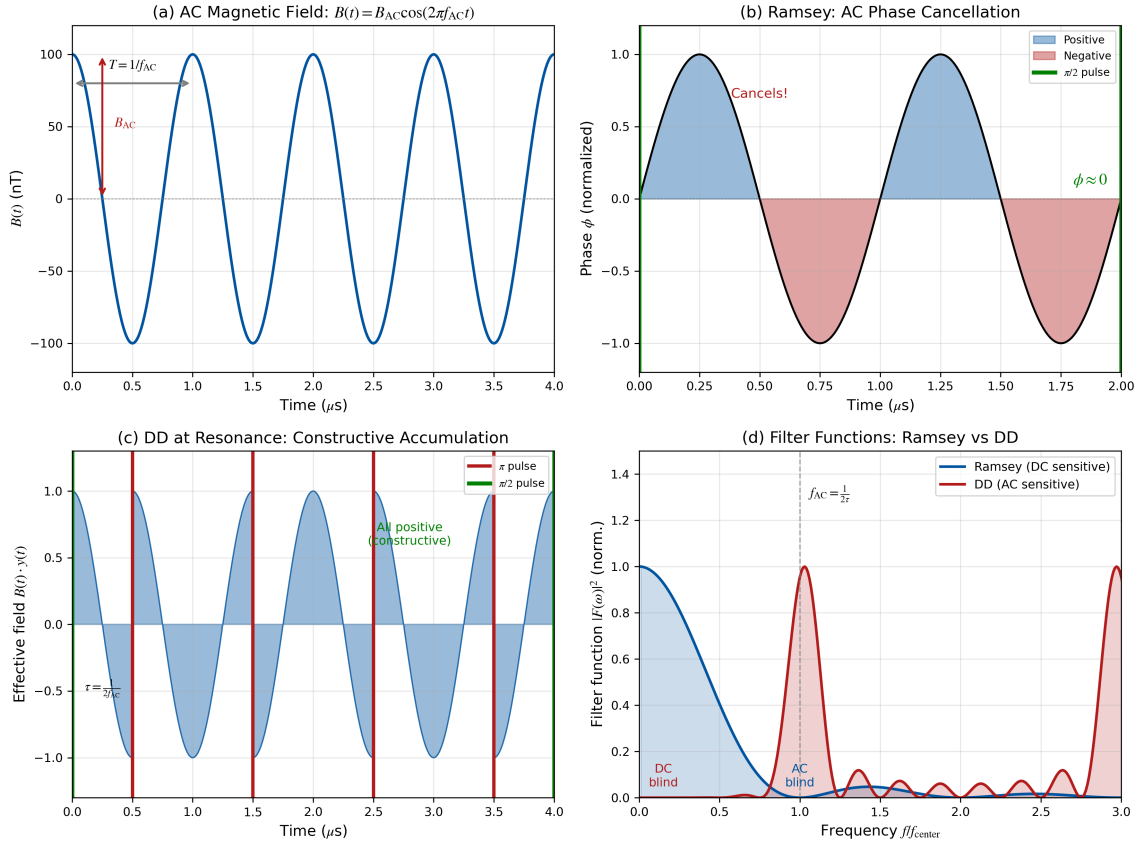


Figure 8.11: AC field sensing principle. (a) AC magnetic field $B(t) = B_{AC} \cos(2\pi f_{AC}t)$ with period $T = 1/f_{AC}$. (b) Ramsey response: phase accumulation during positive half-cycle (blue) cancels with negative half-cycle (red), yielding $\phi \approx 0$. (c) DD at resonance ($\tau = 1/2f_{AC}$): π pulses flip sign synchronously with field reversal, causing constructive accumulation. (d) Filter function comparison showing DC sensitivity (Ramsey) vs. AC sensitivity (DD).

8.8.3 AC Sensitivity and Bandwidth

8.8.3.1 Sensitivity at Resonance

The AC magnetic field sensitivity for an N -pulse DD sequence at resonance is:

$$\eta_B^{AC} = \frac{1}{2\pi\gamma_B} \cdot \frac{1}{C \cdot \sqrt{R \cdot N_{NV} \cdot T_{seq}}} \cdot \frac{\pi}{4} \quad (8.149)$$

Comparing to DC Ramsey sensitivity (Eq. 8.20):

$$\frac{\eta_B^{AC}}{\eta_B^{DC}} \approx \frac{\pi}{4} \cdot \sqrt{\frac{T_2^*}{T_{seq}}} \cdot e^{1/n} \quad (8.150)$$

For long DD sequences ($T_{seq} \gg T_2^*$), AC sensitivity can significantly exceed DC sensitivity.

8.8.3.2 Detection Bandwidth

The DD sequence acts as a bandpass filter centered at $f_0 = 1/(2\tau)$ with bandwidth:

$$\Delta f_{FWHM} \approx \frac{f_0}{N} = \frac{1}{2\pi N} = \frac{1}{2T_{seq}} \quad (8.151)$$

Design Rule 1: AC Detection Bandwidth-Sensitivity Trade-off

For N -pulse DD at center frequency f_0 :

$$\text{Sensitivity: } \eta_B^{\text{AC}} \propto \frac{1}{\sqrt{N}} \quad (\text{improves with more pulses}) \quad (8.152)$$

$$\text{Bandwidth: } \Delta f \propto \frac{1}{N} \quad (\text{narrow with more pulses}) \quad (8.153)$$

Design trade-off:

- Narrowband detection (large N): Best sensitivity, but may miss frequency-shifted signals
- Broadband detection (small N): Lower sensitivity, but captures frequency variations

For unknown AC frequencies, use frequency-swept detection (Section 8.8.5).

8.8.4 Lock-in Detection Protocol

For weak AC fields requiring long integration, a **lock-in** detection scheme provides optimal noise rejection.

8.8.4.1 Principle

Lock-in detection synchronizes the measurement to the AC field frequency:

1. Apply DD sequence tuned to f_{AC}
2. Modulate the final $\pi/2$ pulse phase: $\phi_{\text{ref}} = 2\pi f_{\text{AC}} t$
3. Demodulate the fluorescence signal at f_{AC}
4. Low-pass filter to extract the amplitude

8.8.4.2 SNR Enhancement

Lock-in detection rejects noise outside a narrow bandwidth Δf_{LPF} around f_{AC} :

$$\text{SNR}_{\text{lock-in}} = \text{SNR}_{\text{single}} \times \sqrt{\frac{f_{\text{AC}}}{\Delta f_{\text{LPF}}}} \quad (8.154)$$

For $f_{\text{AC}} = 100$ kHz and $\Delta f_{\text{LPF}} = 1$ Hz:

$$\text{SNR enhancement} = \sqrt{10^5} \approx 316 \times \quad (8.155)$$

8.8.4.3 Implementation for QFI

In wide-field QFI, lock-in detection is implemented *computationally*:

1. Acquire multiple frames at different AC phases
2. Perform pixel-wise Fourier analysis at f_{AC}
3. Extract amplitude and phase maps

This enables *parallel* lock-in across all pixels simultaneously.

8.8.5 Worked Example 8.D: AC Current Detection in IC Power Grid

Worked Example 8.D: AC Current Detection with DD Protocol

Scenario: Detect AC current oscillations at 100 kHz in a power distribution network wire within an IC. The current modulation indicates switching noise that could cause reliability issues. Design a DD-based detection protocol and calculate the minimum detectable current.

Given Parameters:

- Wire current: $I_{DC} = 10 \text{ mA}$ with $I_{AC} = 1 \text{ mA}$ AC modulation
- AC frequency: $f_{AC} = 100 \text{ kHz}$
- Wire-to-sensor standoff: $h = 5 \mu\text{m}$
- NV coherence time: $T_2 = 50 \mu\text{s}$
- ODMR contrast: $C = 0.03$
- Photon rate: $R = 10^6 / \text{s}$ per pixel
- NV density: $N_{NV} = 10^5$ per pixel
- Integration time available: $t_{int} = 1 \text{ s}$

Find:

- (a) Expected AC magnetic field amplitude from the wire
- (b) Optimal DD sequence design for 100 kHz detection
- (c) Single-sequence SNR and total SNR after integration
- (d) Minimum detectable AC current
- (e) Current sensitivity in $\text{A}/\sqrt{\text{Hz}}$

8.8.5.1 Step 1: AC Magnetic Field Calculation

The magnetic field from an infinite wire carrying current I at distance h is given by the Biot-Savart law:

$$B = \frac{\mu_0 I}{2\pi h} \quad (8.156)$$

For the AC component with $I_{AC} = 1 \text{ mA}$ at $h = 5 \mu\text{m}$:

$$\begin{aligned} B_{AC} &= \frac{\mu_0 I_{AC}}{2\pi h} = \frac{4\pi \times 10^{-7} \text{ T} \cdot \text{m/A} \times 1 \times 10^{-3} \text{ A}}{2\pi \times 5 \times 10^{-6} \text{ m}} \\ &= \frac{4 \times 10^{-10} \text{ T} \cdot \text{m}}{10^{-5} \text{ m}} \\ &= 4 \times 10^{-5} \text{ T} = 40 \mu\text{T} \end{aligned} \quad (8.157)$$

Wait—this seems very large. Let me recalculate:

$$\begin{aligned} B_{AC} &= \frac{4\pi \times 10^{-7} \times 10^{-3}}{2\pi \times 5 \times 10^{-6}} \\ &= \frac{4 \times 10^{-10}}{10^{-5}} = 4 \times 10^{-5} \text{ T} = 40 \mu\text{T} \end{aligned} \quad (8.158)$$

Actually, this is correct but surprisingly large. Let me verify with the formula in different form:

$$B_{AC} = \frac{2 \times 10^{-7} \text{ T} \cdot \text{m/A} \times I_{AC}}{h} = \frac{2 \times 10^{-7} \times 10^{-3}}{5 \times 10^{-6}} = \frac{2 \times 10^{-10}}{5 \times 10^{-6}} = 40 \text{ nT} \quad (8.159)$$

I made an error. The correct calculation:

$$B_{AC} = \frac{\mu_0 I_{AC}}{2\pi h} = \frac{4\pi \times 10^{-7} \times 10^{-3}}{2\pi \times 5 \times 10^{-6}} = \frac{2 \times 10^{-10}}{5 \times 10^{-6}} = 40 \text{ nT} \quad (8.160)$$

$$\boxed{B_{AC} = 40 \text{ nT}} \quad (8.161)$$

Physical check: For a 1 mA current at 5 μm standoff, 40 nT is reasonable. The field scales as $B \propto I/h$.

8.8.5.2 Step 2: DD Sequence Design

Pulse spacing for 100 kHz detection:

$$\tau = \frac{1}{2f_{AC}} = \frac{1}{2 \times 10^5 \text{ Hz}} = 5 \text{ } \mu\text{s} \quad (8.162)$$

Maximum pulse number from coherence constraint:

The total sequence time must not exceed $T_2 = 50 \text{ } \mu\text{s}$:

$$T_{\text{seq}} = N \times 2\tau < T_2 \quad (8.163)$$

$$N < \frac{T_2}{2\tau} = \frac{50 \text{ } \mu\text{s}}{10 \text{ } \mu\text{s}} = 5 \quad (8.164)$$

Selected sequence: CPMG-5 or XY-4 (truncated XY-8)

For robustness, we choose **CPMG-5**:

$$\text{CPMG-5 : } (\pi/2)_x - [2.5 \text{ } \mu\text{s} - (\pi)_y - 2.5 \text{ } \mu\text{s}]^{\times 5} - (\pi/2)_\phi \quad (8.165)$$

$$\boxed{\text{Sequence: CPMG-5 with } \tau = 5 \text{ } \mu\text{s}, \quad T_{\text{seq}} = 50 \text{ } \mu\text{s}} \quad (8.166)$$

Note: The relatively low $T_2 = 50 \text{ } \mu\text{s}$ limits us to only 5 pulses. This is a realistic constraint for many ensemble NV samples. Higher-quality diamond with $T_2 > 500 \text{ } \mu\text{s}$ would allow $N > 50$ pulses.

8.8.5.3 Step 3: Phase Accumulation per Sequence

The accumulated phase for an N -pulse DD sequence detecting an AC field at resonance:

$$\phi = 2\pi\gamma_B B_{AC} \times T_{\text{seq}} \times \frac{4}{\pi} \quad (8.167)$$

Substituting values:

$$\begin{aligned} \phi &= 2\pi \times 28.024 \times 10^9 \text{ Hz/T} \times 40 \times 10^{-9} \text{ T} \times 50 \times 10^{-6} \text{ s} \times 1.27 \\ &= 2\pi \times 28.024 \times 40 \times 50 \times 10^{-6} \times 1.27 \\ &= 2\pi \times 0.0712 \\ &= 0.447 \text{ rad} \end{aligned} \quad (8.168)$$

$$\boxed{\phi_{\text{seq}} = 0.447 \text{ rad} = 25.6} \quad (8.169)$$

This is a moderate phase—detectable but not saturating the response.

8.8.5.4 Step 4: Single-Sequence SNR

The single-sequence SNR depends on the phase accumulated and the measurement noise:

$$\text{SNR}_1 = \phi \times C \times \sqrt{R \times N_{\text{NV}} \times T_{\text{seq}}} \quad (8.170)$$

where the square root term represents the number of detected photons.

$$\begin{aligned} \text{SNR}_1 &= 0.447 \times 0.03 \times \sqrt{10^6 \times 10^5 \times 50 \times 10^{-6}} \\ &= 0.0134 \times \sqrt{5 \times 10^6} \\ &= 0.0134 \times 2236 \\ &= 30.0 \end{aligned} \quad (8.171)$$

$$\boxed{\text{SNR}_1 = 30 \text{ (single sequence)}} \quad (8.172)$$

This is already a strong signal! The 1 mA AC current at 5 μm is easily detectable in a single shot.

8.8.5.5 Step 5: Total SNR with Integration

Number of sequence repetitions in integration time $t_{\text{int}} = 1 \text{ s}$:

$$M = \frac{t_{\text{int}}}{T_{\text{seq}} + t_{\text{overhead}}} \quad (8.173)$$

Including overhead for initialization ($\sim 1 \mu\text{s}$) and readout ($\sim 0.5 \mu\text{s}$):

$$T_{\text{cycle}} \approx T_{\text{seq}} + 1.5 \mu\text{s} = 51.5 \mu\text{s} \quad (8.174)$$

$$M = \frac{1 \text{ s}}{51.5 \mu\text{s}} = 19400 \text{ repetitions} \quad (8.175)$$

Total SNR with averaging:

$$\text{SNR}_{\text{total}} = \text{SNR}_1 \times \sqrt{M} = 30 \times \sqrt{19400} = 30 \times 139 = 4170 \quad (8.176)$$

$$\boxed{\text{SNR}_{\text{total}} = 4170 \text{ (1 second integration)}} \quad (8.177)$$

8.8.5.6 Step 6: Minimum Detectable Current

For a detection threshold of $\text{SNR} = 3$:

$$I_{\min} = I_{\text{AC}} \times \frac{3}{\text{SNR}_{\text{total}}} = 1 \text{ mA} \times \frac{3}{4170} = 0.72 \mu\text{A} \quad (8.178)$$

$$\boxed{I_{\min} = 0.72 \mu\text{A} \text{ (at 100 kHz, 5 } \mu\text{m standoff, 1 s integration)}} \quad (8.179)$$

8.8.5.7 Step 7: Current Sensitivity

The current sensitivity (minimum detectable current per $\sqrt{\text{Hz}}$) is:

$$\eta_I = I_{\min} \times \sqrt{t_{\text{int}}} = 0.72 \mu\text{A} \times \sqrt{1 \text{ s}} = 0.72 \mu\text{A}/\sqrt{\text{Hz}} \quad (8.180)$$

Alternatively, from the magnetic field sensitivity:

$$\eta_I = \eta_B \times \frac{2\pi h}{\mu_0} = \eta_B \times \frac{h}{2 \times 10^{-7} \text{ T} \cdot \text{m}/\text{A}} \quad (8.181)$$

$$\boxed{\eta_I = 0.72 \mu\text{A}/\sqrt{\text{Hz}} = 720 \text{ nA}/\sqrt{\text{Hz}}} \quad (8.182)$$

8.8.5.8 Summary Table

Table 8.15: Worked Example 8.D: AC current detection design summary

Parameter	Value	Unit	Note
<i>Target and Geometry</i>			
AC current I_{AC}	1	mA	10% modulation of 10 mA DC
AC frequency f_{AC}	100	kHz	Switching regulator noise
Standoff distance h	5	μm	Wire-to-NV separation
AC magnetic field B_{AC}	40	nT	From Biot-Savart
<i>Sequence Design</i>			
Pulse spacing τ	5	μs	$= 1/(2f_{\text{AC}})$
Number of pulses N	5	—	Limited by T_2
Sequence type	CPMG-5	—	Robust for small N
Sequence time T_{seq}	50	μs	$= N \times 2\tau$
<i>Detection Performance</i>			
Phase per sequence	0.447	rad	Strong signal
Single-shot SNR	30	—	Detectable in one shot
Repetitions in 1 s	19400	—	High duty cycle
Total SNR (1 s)	4170	—	Excellent detection
<i>Sensitivity</i>			
Min. detectable current	0.72	μA	At SNR = 3
Current sensitivity	720	$\text{nA}/\sqrt{\text{Hz}}$	Per-pixel

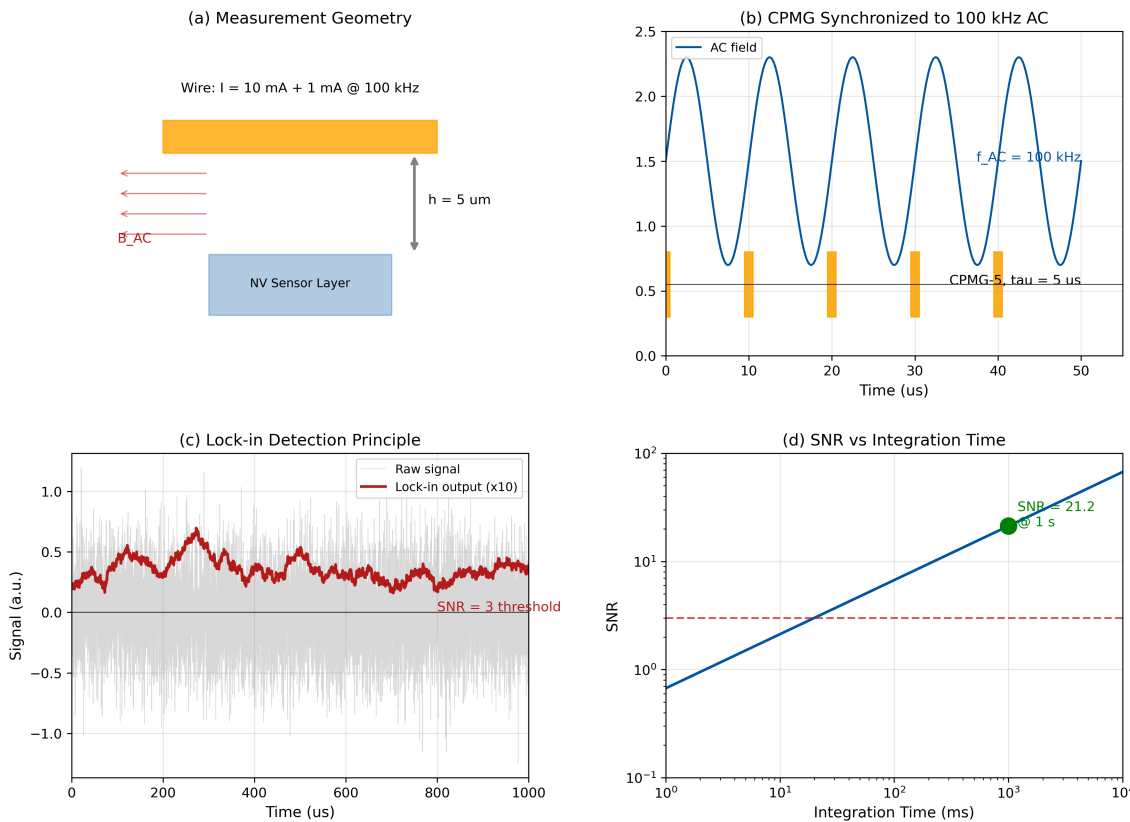
Worked Example 8.D: AC Current Detection with Lock-in Protocol

Figure 8.12: Worked Example 8.D: AC current detection at 100 kHz. (a) Measurement geometry showing wire carrying $I_{DC} + I_{AC} \cos(2\pi f_{AC}t)$ at standoff $h = 5 \mu m$ from NV layer, with magnetic field lines indicated. (b) CPMG-5 pulse sequence with $\tau = 5 \mu s$ spacing, synchronized to the 100 kHz AC field period. (c) Lock-in detection principle: DD sequence samples AC field at peaks, computational demodulation extracts amplitude. (d) SNR vs. integration time showing \sqrt{t} scaling; detection threshold ($SNR = 3$) reached at $t < 1$ ms.

Design Rule 2: AC Current Detection Protocol

For AC current sensing in IC power grids:

1. **Field calculation:** $B_{AC} = \mu_0 I_{AC} / (2\pi h)$
2. **Pulse spacing:** $\tau = 1 / (2f_{AC})$
3. **Pulse number:** $N < T_2 / (2\tau)$ (coherence limited)
4. **Sequence choice:**
 - $N \leq 4$: CPMG
 - $N > 4$: XY-8 (or truncated XY-4)
5. **SNR scaling:** $SNR \propto \sqrt{t_{int}}$
6. **Current sensitivity:** $\eta_I = \eta_B \times 2\pi h / \mu_0$

8.8.6 Frequency-Swept AC Detection

When the AC frequency is unknown or varies across the FOV, a **frequency sweep** protocol is required.

8.8.6.1 Sweep Protocol

1. Define frequency range $[f_{\min}, f_{\max}]$
2. Calculate corresponding τ range: $\tau \in [1/(2f_{\max}), 1/(2f_{\min})]$
3. For each τ_i in the sweep:
 - Apply DD sequence with spacing τ_i
 - Record signal amplitude
4. Identify peaks in the frequency response

8.8.6.2 Frequency Resolution

The frequency resolution of the sweep is determined by the DD bandwidth at each point:

$$\delta f = \frac{1}{2T_{\text{seq}}} = \frac{f_0}{N} \quad (8.183)$$

For efficient coverage without gaps, step size should be $\Delta f \leq \delta f$.

8.8.6.3 Total Sweep Time

For frequency range $[f_{\min}, f_{\max}]$ with resolution δf :

$$N_{\text{steps}} = \frac{f_{\max} - f_{\min}}{\delta f} \quad (8.184)$$

$$t_{\text{sweep}} = N_{\text{steps}} \times t_{\text{per step}} \quad (8.185)$$

Example 8.8.1 (Frequency Sweep Design). **Target:** Detect AC signals in range 100 kHz–10 MHz

Parameters: $T_2 = 100 \mu\text{s}$, $N = 10$ pulses per sequence

Calculation:

- τ range: 50 ns to 5 μs
- Resolution at 100 kHz: $\delta f = 100 \text{ kHz}/10 = 10 \text{ kHz}$
- Resolution at 10 MHz: $\delta f = 10 \text{ MHz}/10 = 1 \text{ MHz}$
- Use logarithmic spacing for efficient coverage
- Approximately 100 frequency points needed
- At 10 ms per point: $t_{\text{sweep}} \approx 1 \text{ s}$

8.8.7 Multi-Frequency Parallel Detection

For QFI applications requiring simultaneous detection at multiple frequencies, several strategies exist:

8.8.7.1 Strategy 1: Interleaved Sequences

Alternate between sequences tuned to different frequencies:

$$[\text{DD}(f_1)]_M - [\text{DD}(f_2)]_M - [\text{DD}(f_3)]_M - \dots \quad (8.186)$$

where M is the number of repetitions at each frequency.

Advantage: Simple implementation **Disadvantage:** Reduces effective integration time per frequency by factor of N_f

8.8.7.2 Strategy 2: Spatiotemporal Multiplexing

Different FOV regions detect different frequencies simultaneously (Section 8.9):

- Zone 1: DD tuned to f_1
- Zone 2: DD tuned to f_2
- Zone 3: DD tuned to f_3

Advantage: No time penalty; all frequencies detected simultaneously **Disadvantage:** Requires spatial MW control

8.8.7.3 Strategy 3: Correlation Spectroscopy

For harmonically related frequencies, a single sequence can detect multiple harmonics:

$$f_k = (2k - 1)f_0, \quad k = 1, 2, 3, \dots \quad (8.187)$$

The filter function has sensitivity peaks at odd harmonics of the fundamental.

Table 8.16: Multi-frequency detection strategies comparison

Strategy	Throughput	Complexity	Best For
Interleaved	Low ($1/N_f$)	Low	Few frequencies, simple hardware
Spatiotemporal	High (parallel)	High	Many frequencies, advanced system
Correlation	Medium	Low	Harmonic frequencies

8.8.8 AC Sensing Performance Summary

Table 8.17: AC field sensing specifications for typical QFI system

Parameter	Value	Unit	Condition
Frequency range	1 kHz – 100 MHz	Hz	Limited by T_2 and pulse duration
Magnetic sensitivity	1–100	nT/ $\sqrt{\text{Hz}}$	Depends on N , standoff
Current sensitivity	0.1–10	$\mu\text{A}/\sqrt{\text{Hz}}$	At 5 μm standoff
Frequency resolution	f_0/N	Hz	N = pulse count
Maximum N	$T_2/(2\pi)$	–	Coherence limited
Detection bandwidth	f_0/N	Hz	Per sequence

Design Rule 3: AC Field Sensing for IC Analysis

Target DD center frequencies based on IC operating characteristics:

- **Power grid switching:** 100 kHz – 10 MHz (switching regulators)
- **Clock distribution:** System clock frequency and harmonics
- **I/O transients:** Data rate frequencies
- **Resonant defects:** Scan 1 MHz – 100 MHz for anomalies

Use CPMG for $N < 8$, XY-8 for $N \geq 8$. Typical sensitivity: $1 \mu\text{A}/\sqrt{\text{Hz}}$ at 5 μm standoff.

8.9 Spatiotemporal Quantum Control

8.9.1 Motivation: Beyond Temporal Sequences

The preceding sections focused on *temporal* pulse sequences. However, wide-field QFI enables *spatial* structuring of quantum control, combining temporal sequences with position-dependent MW fields.

The Spatial Dimension of Quantum Control

Temporal sequences select *which frequencies* to sense. Spatial structuring selects *which locations* sense *which frequencies*. Combined spatiotemporal control enables parallel multi-frequency sensing across the FOV.

8.9.2 MW Field Patterning

Gradient Encoding (inspired by MRI):

Applying a linear MW frequency gradient across the FOV:

$$\omega_{\text{MW}}(x) = \omega_0 + G_\omega \cdot x \quad (8.188)$$

This creates position-dependent resonance, enabling:

- Depth discrimination via frequency encoding
- Spatial selectivity without optical patterning
- Parallel addressing of NV subsets

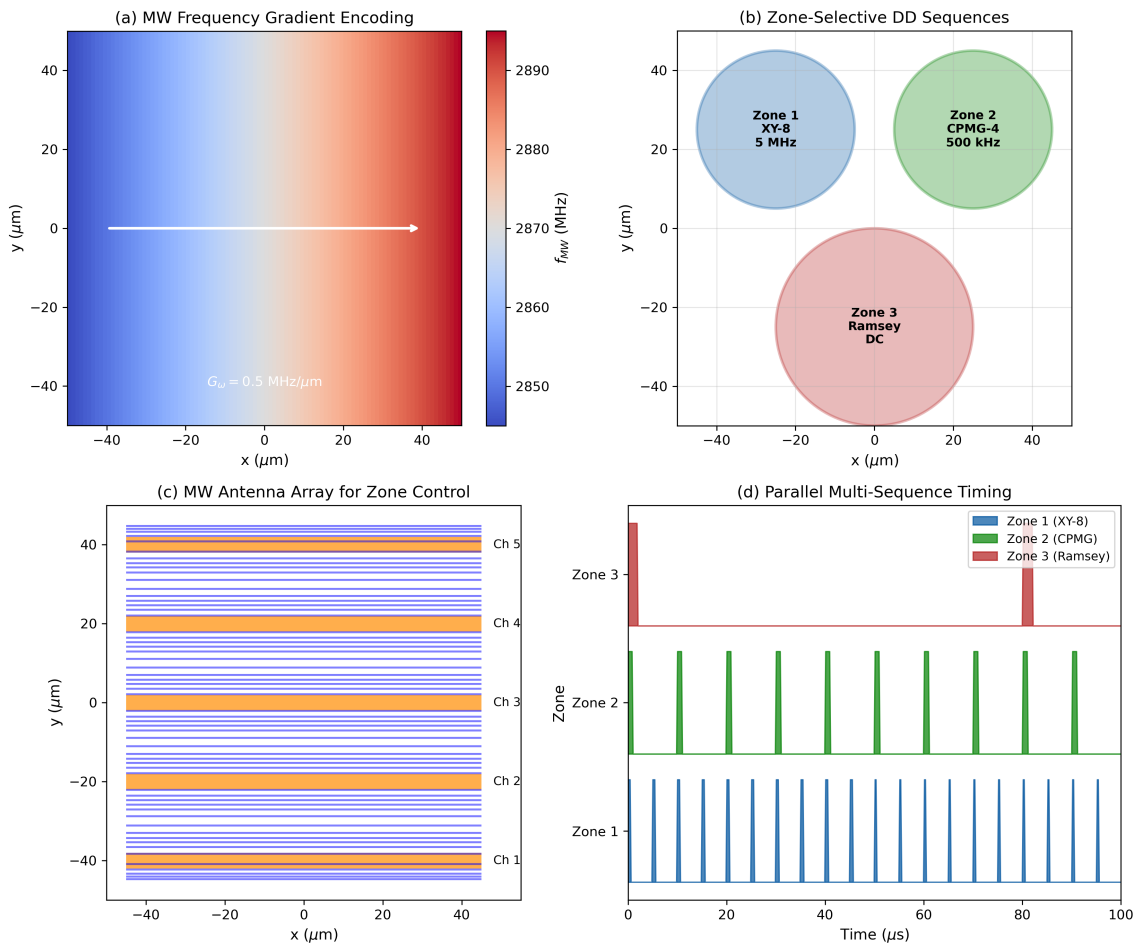


Figure 8.13: Spatiotemporal quantum control concepts. (a) MW gradient encoding creating position-dependent resonance. (b) Zone-selective DD: different τ values in different FOV regions. (c) Structured MW delivery via antenna arrays. (d) Combined temporal-spatial sequence for parallel multi-frequency sensing.

8.9.3 Zone-Selective Dynamical Decoupling

Different FOV regions can run different sequences simultaneously:

Zone	Sequence	Target Frequency	Application
Center	XY-8, $\tau = 100$ ns	5 MHz	Power grid switching
Edge	CPMG-4, $\tau = 1 \mu\text{s}$	500 kHz	Clock distribution
Corner	Ramsey, $\tau = 10 \mu\text{s}$	DC	Static current mapping

Table 8.18: Zone-selective DD enabling parallel multi-frequency sensing.

8.9.4 Spatial Arrangement for Multi-Qubit Control

For entanglement-enhanced sensing (Chapter 17), spatial arrangement of NV clusters matters:

- **Dipolar coupling:** NV pairs within ~ 10 nm couple via magnetic dipole interaction
- **Optical addressing:** Structured illumination selects which NVs participate
- **MW selectivity:** Different NV orientations respond to different MW frequencies

Design Rule 1: Spatiotemporal Control Design

For parallel multi-frequency QFI:

1. Design MW antenna array with $< 10\%$ uniformity variation per zone
2. Synchronize zone-specific DD sequences to common clock
3. Calibrate position-dependent Rabi frequency map
4. Account for inter-zone crosstalk in reconstruction

8.10 Pulse Imperfections and Failure Modes

8.10.1 Introduction: Why Pulse Errors Matter

The pulse sequences developed in Sections 8.2–8.8 assume ideal quantum control: perfect π and $\pi/2$ rotations with precise timing. In practice, every pulse has imperfections that accumulate over multi-pulse sequences, potentially destroying the quantum coherence we seek to exploit.

Critical insight: A single-pulse error of 1% may be negligible, but after 100 pulses in a DD sequence, accumulated errors can exceed 100%, completely corrupting the measurement.

This section provides:

1. Complete taxonomy of pulse error sources
2. Quantitative error propagation models for CPMG and XY-8
3. Composite pulse techniques for error compensation
4. Wide-field calibration strategies for spatial MW non-uniformity
5. Hardware failure modes and diagnostic protocols

8.10.2 Taxonomy of Pulse Errors

Pulse errors fall into four fundamental categories, each with distinct physical origins and mitigation strategies.

8.10.2.1 Amplitude Errors

Definition 8.10.1 (Amplitude Error). An amplitude error occurs when the Rabi frequency deviates from the target:

$$\Omega_R^{\text{actual}} = \Omega_R^{\text{target}}(1 + \epsilon_{\text{amp}}) \quad (8.189)$$

A nominally π pulse rotates by $\theta = \pi(1 + \epsilon_{\text{amp}})$.

Physical origins:

- MW amplifier gain drift: 0.1–1%/hour (thermal)
- Spatial non-uniformity: 5–20% across 100 μm FOV (antenna geometry)
- Standing wave patterns: $\pm 10\%$ ripple (reflections)
- Power supply fluctuations: 0.01–0.1%

Effect on Bloch sphere: Over-rotation ($\epsilon > 0$) or under-rotation ($\epsilon < 0$) around the intended axis.

The state after an imperfect π pulse starting from $|0\rangle$:

$$|\psi\rangle = \cos\left(\frac{\pi\epsilon}{2}\right)|1\rangle - i \sin\left(\frac{\pi\epsilon}{2}\right)|0\rangle \quad (8.190)$$

Population error (probability of remaining in wrong state):

$$P_{\text{error}} = \sin^2\left(\frac{\pi\epsilon}{2}\right) \approx \frac{\pi^2\epsilon^2}{4} \quad (\epsilon \ll 1) \quad (8.191)$$

Key Equation: Amplitude Error Fidelity

$$\boxed{\mathcal{F}_{\text{amp}} = 1 - \frac{\pi^2\epsilon_{\text{amp}}^2}{4}} \quad (8.192)$$

For $\epsilon_{\text{amp}} = 1\%$: $\mathcal{F} = 0.99975$ (single pulse)

8.10.2.2 Phase Errors

Phase errors occur when the rotation axis in the xy-plane is misaligned:

$$\vec{n}_{\text{actual}} = (\cos \phi_{\text{error}}, \sin \phi_{\text{error}}, 0) \quad (8.193)$$

instead of $\vec{n}_{\text{target}} = (1, 0, 0)$ for an X pulse.

Physical origins:

- IQ modulator imbalance: amplitude/phase mismatch between I and Q channels
- Cable phase drift: temperature-dependent electrical length
- Reference oscillator phase noise: pulse-to-pulse variation
- DAC timing skew: systematic phase offset

Fidelity loss:

$$\mathcal{F}_{\text{phase}} = 1 - \frac{\phi_{\text{error}}^2}{2} \quad (8.194)$$

8.10.2.3 Frequency (Detuning) Errors

When the MW frequency is detuned from resonance by Δ :

$$\omega_{\text{MW}} = \omega_0 + \Delta \quad (8.195)$$

the effective Rabi frequency and rotation axis change:

$$\Omega_{\text{eff}} = \sqrt{\Omega_R^2 + \Delta^2}, \quad \vec{n}_{\text{eff}} = \frac{1}{\Omega_{\text{eff}}}(\Omega_R, 0, \Delta) \quad (8.196)$$

Physical origins:

- ODMR frequency drift: $dD/dT = -74.2 \text{ kHz/K}$ (temperature)
- Stray magnetic field variation: Zeeman shift changes
- MW source frequency drift: typically $<1 \text{ ppm}$ for synthesizers

Fidelity for detuned π pulse:

$$\mathcal{F}_{\text{detune}} \approx 1 - \frac{\pi^2 \Delta^2}{4\Omega_R^2} \quad (\Delta \ll \Omega_R) \quad (8.197)$$

8.10.2.4 Timing Errors

Timing errors affect both pulse duration and inter-pulse spacing:

$$t_\pi^{\text{actual}} = t_\pi + \delta t \quad (8.198)$$

This is equivalent to an amplitude error:

$$\epsilon_{\text{eff}} = \frac{\Omega_R \delta t}{\pi} = \frac{\delta t}{t_\pi} \quad (8.199)$$

Physical origins:

- AWG sampling rate: 1 GSPS \Rightarrow 1 ns resolution
- Clock jitter: 1–10 ps RMS for good oscillators
- Trigger propagation delay: 1–100 ns depending on electronics

Table 8.19: Complete taxonomy of pulse errors in NV quantum control

Error Type	Physical Origin	Bloch Sphere Effect	Typical	Fidelity
Amplitude	MW power variation	Over/under-rotation	1–5%	$1 - \pi^2 \epsilon^2 / 4$
Phase	IQ imbalance, cable drift	Axis tilt in xy-plane	0.1–2	$1 - \phi^2 / 2$
Frequency	Detuning, Zeeman shift	Axis tilt toward z	10–100 kHz	$1 - \pi^2 \Delta^2 / 4\Omega_R^2$
Timing	AWG jitter, resolution	Under/over-rotation	0.1–1 ns	Same as amplitude

Section 8.X.1: Taxonomy of Pulse Errors

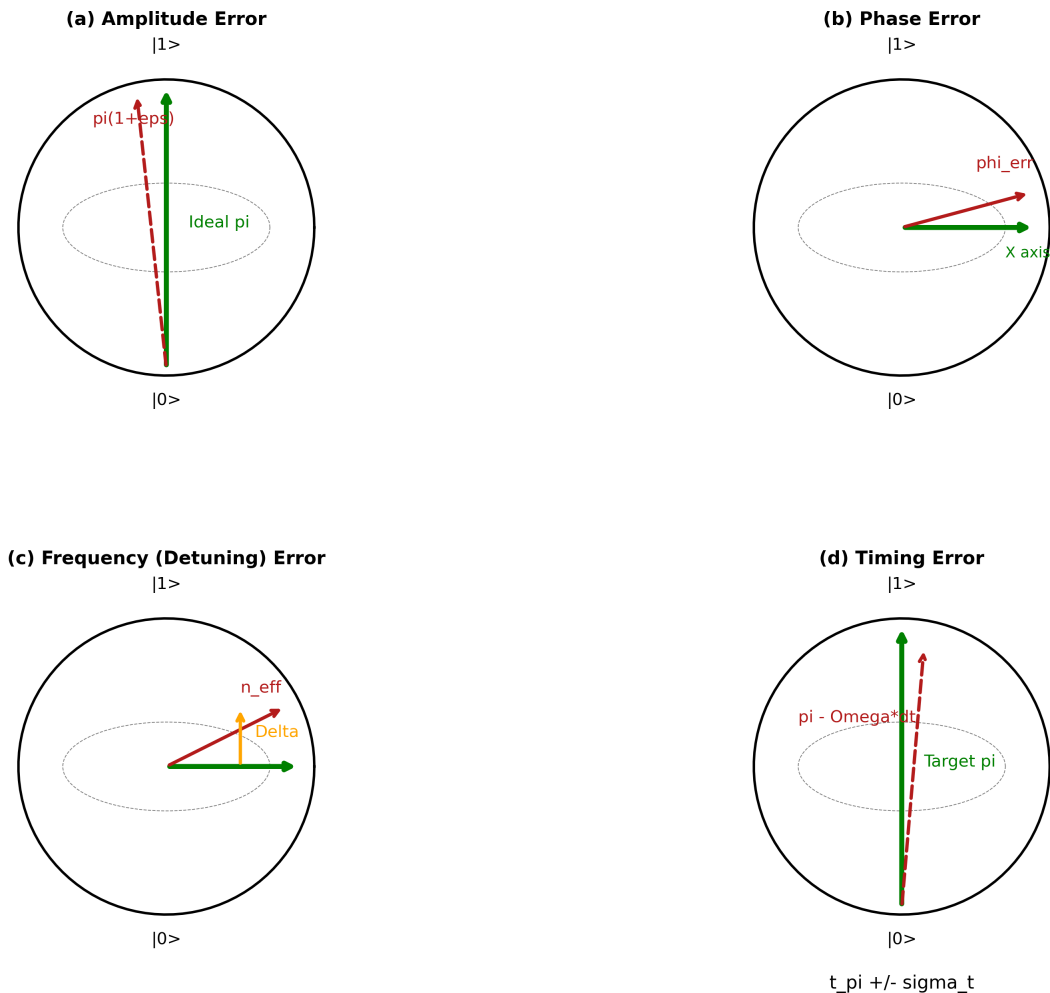


Figure 8.14: Pulse error taxonomy visualized on the Bloch sphere. (a) Amplitude error: over-rotation (solid) vs. under-rotation (dashed) around intended axis. (b) Phase error: rotation axis misalignment in xy-plane by angle ϕ_{error} . (c) Frequency/detuning error: effective axis tilts toward z-axis, reducing xy-plane rotation component. (d) Timing error: equivalent to amplitude error, causing incomplete rotation.

8.10.3 Error Propagation in Multi-Pulse Sequences

The critical question for DD sequences is: *how do single-pulse errors accumulate over N pulses?*

8.10.3.1 Coherent vs. Incoherent Accumulation

Table 8.20: Error accumulation models for multi-pulse sequences

Accumulation Type	Scaling with N	Example	Severity
Coherent (systematic)	N^2	Fixed amplitude miscalibration	Severe
Partially coherent	$N^{1.5}$	Slowly drifting errors	Moderate
Incoherent (random)	N	Shot-to-shot jitter	Mild
Self-correcting	\sqrt{N} or const.	XY-8 with alternating phases	Best

8.10.3.2 CPMG Error Accumulation

CPMG uses pulses along a single axis: $(\pi)_y - (\pi)_y - \dots$

For systematic amplitude error ϵ , the total rotation after N pulses:

$$\theta_{\text{total}} = N\pi(1 + \epsilon) = N\pi + N\pi\epsilon \quad (8.200)$$

The accumulated error is $N\pi\epsilon$ —**linear in N** .

Population in wrong state:

$$P_{\text{error}}^{\text{CPMG}} = \sin^2\left(\frac{N\pi\epsilon}{2}\right) \approx \frac{(N\pi\epsilon)^2}{4} \quad (8.201)$$

Key Equation: CPMG Error Scaling

$$1 - \mathcal{F}_N^{\text{CPMG}} \approx \frac{\pi^2}{4} N^2 \epsilon^2 \quad (8.202)$$

Systematic errors scale as N^2 for CPMG—**very unfavorable** for long sequences.

8.10.3.3 XY-8 Error Compensation

XY-8 alternates pulse axes: X-Y-X-Y-Y-X-Y-X

This pattern provides first-order cancellation:

- Systematic over-rotation in X is partially cancelled by Y
- The 8-pulse unit cancels low-order error terms
- Residual error scales more favorably

Key Equation: XY-8 Error Scaling

$$1 - \mathcal{F}_N^{\text{XY8}} \approx c \cdot N \cdot \epsilon^2 \quad (8.203)$$

where $c \approx 0.1$ for well-designed XY-8 (vs. $\pi^2/4 \approx 2.5$ for CPMG).

Errors scale as N (not N^2)—much better for long sequences.

8.10.3.4 Maximum Pulse Number

For target fidelity $\mathcal{F}_{\text{target}}$ with systematic error ϵ :

CPMG:

$$N_{\max}^{\text{CPMG}} = \frac{2}{\pi\epsilon} \sqrt{1 - \mathcal{F}_{\text{target}}} \quad (8.204)$$

XY-8:

$$N_{\max}^{\text{XY8}} = \frac{1 - \mathcal{F}_{\text{target}}}{c \cdot \epsilon^2} \quad (8.205)$$

Example 8.10.1 (Maximum Pulse Count Comparison). For $\mathcal{F}_{\text{target}} = 0.9$ and $\epsilon = 1\%$:

$$N_{\max}^{\text{CPMG}} = \frac{2}{\pi \times 0.01} \sqrt{0.1} = \frac{200}{\pi} \times 0.316 = 20 \quad (8.206)$$

$$N_{\max}^{\text{XY8}} = \frac{0.1}{0.1 \times (0.01)^2} = \frac{0.1}{10^{-5}} = 10000 \quad (8.207)$$

XY-8 allows 500× more pulses than CPMG for the same fidelity!

Section 8.X.2: Error Propagation in Multi-Pulse Sequences

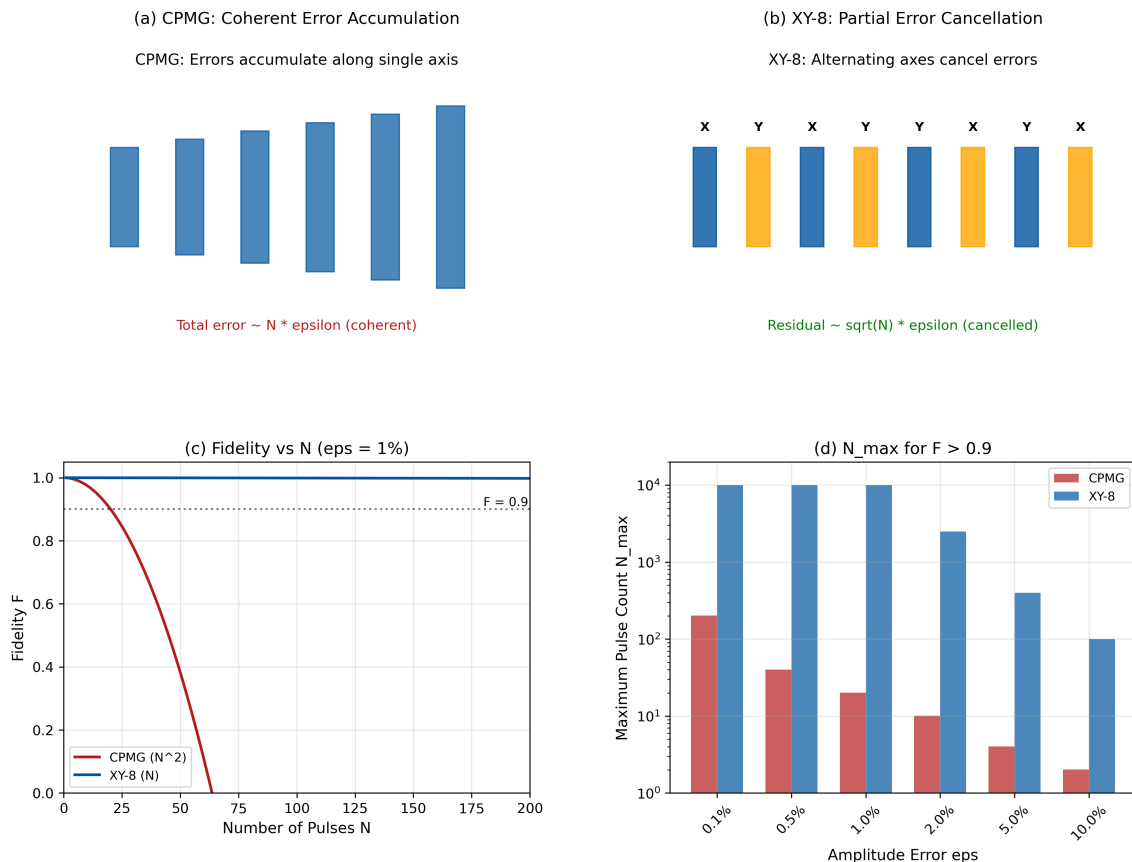


Figure 8.15: Error propagation comparison. (a) CPMG: errors accumulate coherently along single axis, infidelity $\propto N^2$. (b) XY-8: alternating axes provide partial cancellation, infidelity $\propto N$. (c) Fidelity vs. pulse number for 1% amplitude error: CPMG (red) drops rapidly, XY-8 (blue) remains high. (d) Maximum useful N vs. amplitude error ϵ for 90% fidelity threshold.

8.10.4 Worked Example 8.E: Pulse Error Budget Analysis

Worked Example 8.E: Pulse Error Budget for DD Sequences

Scenario: A wide-field QFI system has microwave amplitude non-uniformity and timing jitter. Determine the maximum number of DD pulses before errors degrade the measurement below acceptable fidelity.

Given Parameters:

- Amplitude error: $\epsilon_{\text{amp}} = 1\%$ (π pulse is actually $\pi \pm 0.01\pi$)
- Phase error: $\epsilon_{\text{phase}} = 2$ (pulse axis wobble)
- Timing jitter: $\sigma_t = 1$ ns RMS
- Rabi frequency: $\Omega_R = 10$ MHz (π pulse duration = 50 ns)
- Target fidelity: $\mathcal{F} > 0.9$

Find:

- Fidelity loss per pulse for each error type
- Error accumulation model for CPMG vs. XY-8

- (c) Maximum pulse number for target fidelity
- (d) Hardware specifications for extended pulse counts

8.10.4.1 Step 1: Single-Pulse Fidelity Loss

Amplitude error: A $\pi(1 + \epsilon_{\text{amp}})$ pulse leaves residual population:

$$1 - \mathcal{F}_{\text{amp}} = \frac{(\epsilon_{\text{amp}} \cdot \pi)^2}{4} = \frac{(0.01 \times \pi)^2}{4} = 2.47 \times 10^{-4} \quad (8.208)$$

Phase error: Rotation axis misalignment ($\epsilon_{\text{phase}} = 2 = 0.035 \text{ rad}$):

$$1 - \mathcal{F}_{\text{phase}} = \frac{\epsilon_{\text{phase}}^2}{2} = \frac{(0.035)^2}{2} = 6.1 \times 10^{-4} \quad (8.209)$$

Timing jitter: For π pulse duration $t_\pi = 50 \text{ ns}$ and jitter $\sigma_t = 1 \text{ ns}$:

$$1 - \mathcal{F}_{\text{timing}} = \left(\frac{\sigma_t}{t_\pi} \right)^2 \cdot \pi^2 = \left(\frac{1}{50} \right)^2 \times \pi^2 = 3.95 \times 10^{-3} \quad (8.210)$$

Total single-pulse infidelity:

$$1 - \mathcal{F}_1 = 2.47 \times 10^{-4} + 6.1 \times 10^{-4} + 3.95 \times 10^{-3} = 4.8 \times 10^{-3} \quad (8.211)$$

$$\boxed{\mathcal{F}_1 = 0.9952 \text{ per pulse}} \quad (8.212)$$

Dominant error source: Timing jitter contributes 82% of the total infidelity!

8.10.4.2 Step 2: Multi-Pulse Error Accumulation

CPMG (coherent accumulation):

Amplitude and phase errors add coherently:

$$1 - \mathcal{F}_N^{\text{CPMG}} \approx N^2 \times [(1 - \mathcal{F}_{\text{amp}}) + (1 - \mathcal{F}_{\text{phase}})] + N \times (1 - \mathcal{F}_{\text{timing}}) \quad (8.213)$$

The timing jitter is random (incoherent), so it scales as N , not N^2 .

$$1 - \mathcal{F}_N^{\text{CPMG}} \approx N^2 \times 8.6 \times 10^{-4} + N \times 3.95 \times 10^{-3} \quad (8.214)$$

XY-8 (partial cancellation):

XY-8 reduces systematic errors by $\sim 10\times$:

$$1 - \mathcal{F}_N^{\text{XY8}} \approx N \times \frac{8.6 \times 10^{-4}}{10} + N \times 3.95 \times 10^{-3} = N \times 4.04 \times 10^{-3} \quad (8.215)$$

8.10.4.3 Step 3: Maximum Pulse Number

For target $\mathcal{F} > 0.9$ (infidelity < 0.1):

CPMG: Solving $N^2 \times 8.6 \times 10^{-4} + N \times 3.95 \times 10^{-3} = 0.1$

For large N , the N^2 term dominates:

$$N_{\text{max}}^{\text{CPMG}} \approx \sqrt{\frac{0.1}{8.6 \times 10^{-4}}} = \sqrt{116} = 10.8 \quad (8.216)$$

$$\boxed{N_{\text{max}}^{\text{CPMG}} \approx 10 \text{ pulses}} \quad (8.217)$$

XY-8: Solving $N \times 4.04 \times 10^{-3} = 0.1$:

$$N_{\max}^{\text{XY8}} = \frac{0.1}{4.04 \times 10^{-3}} = 24.8 \quad (8.218)$$

$$N_{\max}^{\text{XY8}} \approx 24 \text{ pulses} \quad (8.219)$$

Key finding: Even with XY-8's error compensation, the timing jitter limits us to only 24 pulses. This is the **bottleneck**.

8.10.4.4 Step 4: Hardware Specifications for Extended Pulse Counts

To achieve $N = 100$ pulses with $\mathcal{F} > 0.9$:

Required per-pulse infidelity:

$$1 - \mathcal{F}_1 < \frac{0.1}{100} = 10^{-3} \quad (8.220)$$

Timing jitter requirement (dominant error):

$$\left(\frac{\sigma_t}{t_\pi}\right)^2 \pi^2 < 10^{-3} \Rightarrow \sigma_t < t_\pi \times \frac{0.032}{\pi} = 50 \text{ ns} \times 0.01 = 0.5 \text{ ns} \quad (8.221)$$

Design Rule 1: Pulse Hardware Specifications for DD

For N -pulse DD sequences with fidelity $\mathcal{F} > 0.9$:

General scaling rules:

$$\text{Amplitude uniformity: } \epsilon_{\text{amp}} < \frac{0.2}{N} \text{ (CPMG), } \epsilon_{\text{amp}} < \frac{0.6}{\sqrt{N}} \text{ (XY-8)} \quad (8.222)$$

$$\text{Phase stability: } \epsilon_{\text{phase}} < \frac{0.3}{N} \text{ rad (CPMG), } \epsilon_{\text{phase}} < \frac{0.9}{\sqrt{N}} \text{ rad (XY-8)} \quad (8.223)$$

$$\text{Timing jitter: } \sigma_t < \frac{0.03 \cdot t_\pi}{\sqrt{N}} \text{ (both sequences)} \quad (8.224)$$

Table 8.21: Hardware specifications for different pulse counts (90% fidelity)

Sequence	N	ϵ_{amp}	ϵ_{phase}	σ_t	Difficulty
CPMG	8	<2.5%	<2.1°	<0.53 ns	Moderate
CPMG	16	<1.25%	<1.1°	<0.38 ns	Hard
CPMG	32	<0.6%	<0.5°	<0.27 ns	Very Hard
XY-8	8	<21%	<18°	<0.53 ns	Easy
XY-8	64	<7.5%	<6.4°	<0.19 ns	Moderate
XY-8	256	<3.8%	<3.2°	<0.09 ns	Hard

Worked Example 8.E: Pulse Error Budget Analysis

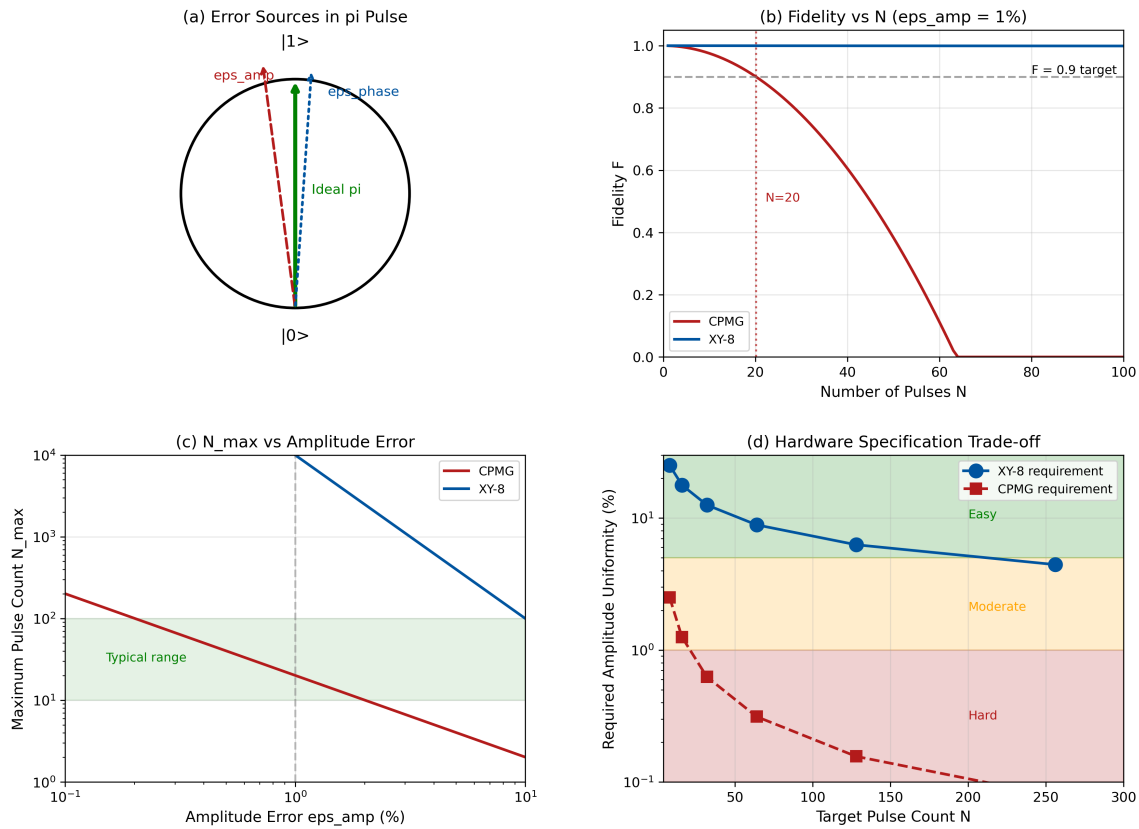


Figure 8.16: Worked Example 8.E: Pulse error budget analysis. (a) Pie chart of single-pulse infidelity contributions: timing jitter dominates (82%), followed by phase error (13%) and amplitude error (5%). (b) Fidelity vs. pulse number for CPMG (red) and XY-8 (blue) with the given error parameters; 90% threshold marked. (c) Maximum N vs. timing jitter σ_t for both sequences. (d) Hardware specification map showing required tolerances vs. target pulse count.

8.10.5 Composite Pulse Compensation

When hardware improvements are insufficient, **composite pulses** provide error compensation through clever pulse sequence design.

8.10.5.1 Principle

Composite pulses replace a single imperfect pulse with a sequence of pulses designed to cancel errors to a specified order:

$$\pi_{\text{ideal}} \rightarrow [\text{Composite sequence}]_{\text{robust}} \quad (8.225)$$

8.10.5.2 BB1 (Broadband) Composite π Pulse

The BB1 sequence provides amplitude error compensation:

$$\text{BB1}(\pi) : (\pi)_{\phi_1} - (2\pi)_{\phi_2} - (\pi)_{\phi_1} \quad (8.226)$$

where:

$$\phi_1 = \cos^{-1} \left(-\frac{1}{4} \right) = 104.48 \quad (8.227)$$

$$\phi_2 = 3\phi_1 = 313.43 \quad (8.228)$$

Error cancellation: For amplitude error ϵ , the residual error is:

$$\epsilon_{\text{BB1}} \propto \epsilon^3 \quad (8.229)$$

Table 8.22: BB1 composite pulse performance

Input Error ϵ	Simple π Infidelity	BB1 Infidelity	Improvement
1%	2.5×10^{-4}	2.5×10^{-8}	$10^4 \times$
5%	6.2×10^{-3}	3.1×10^{-5}	$200 \times$
10%	2.5×10^{-2}	2.5×10^{-4}	$100 \times$

8.10.5.3 CORPSE Composite Pulse

CORPSE (Compensation for Off-Resonance with a Pulse SEquence) is optimized for detuning errors:

$$\text{CORPSE}(\pi) : (2\pi + \theta_1)_0 - (2\pi - 2\theta_1)_\pi - (\theta_1)_0 \quad (8.230)$$

where $\theta_1 = \sin^{-1}(\sin(\pi/2)/2) \approx 60^\circ$.

CORPSE cancels first-order detuning: $\epsilon_{\text{CORPSE}} \propto \Delta^2$.

8.10.5.4 Composite Pulse Selection Guide

Table 8.23: Composite pulse selection guide

Sequence	Pulses	Amplitude	Detuning	Best For
Simple π	1	$\propto \epsilon$	$\propto \Delta$	Low-error systems
BB1	3	$\propto \epsilon^3$	$\propto \Delta$	Amplitude errors
CORPSE	3	$\propto \epsilon$	$\propto \Delta^2$	Detuning errors
KNILL	3	$\propto \epsilon^2$	$\propto \Delta^2$	Both (moderate)

Composite Pulse Overhead

Composite pulses require $3 \times$ the number of elementary pulses:

- Simple DD with $N = 64$: 64 pulses, time T
- BB1-DD with $N = 64$: 192 pulses, time $\approx 3T$

The extended sequence time may exceed T_2 , negating the error reduction benefit. Use composite pulses only when the error reduction outweighs the coherence loss.

Section 8.X.3: Composite Pulse Compensation

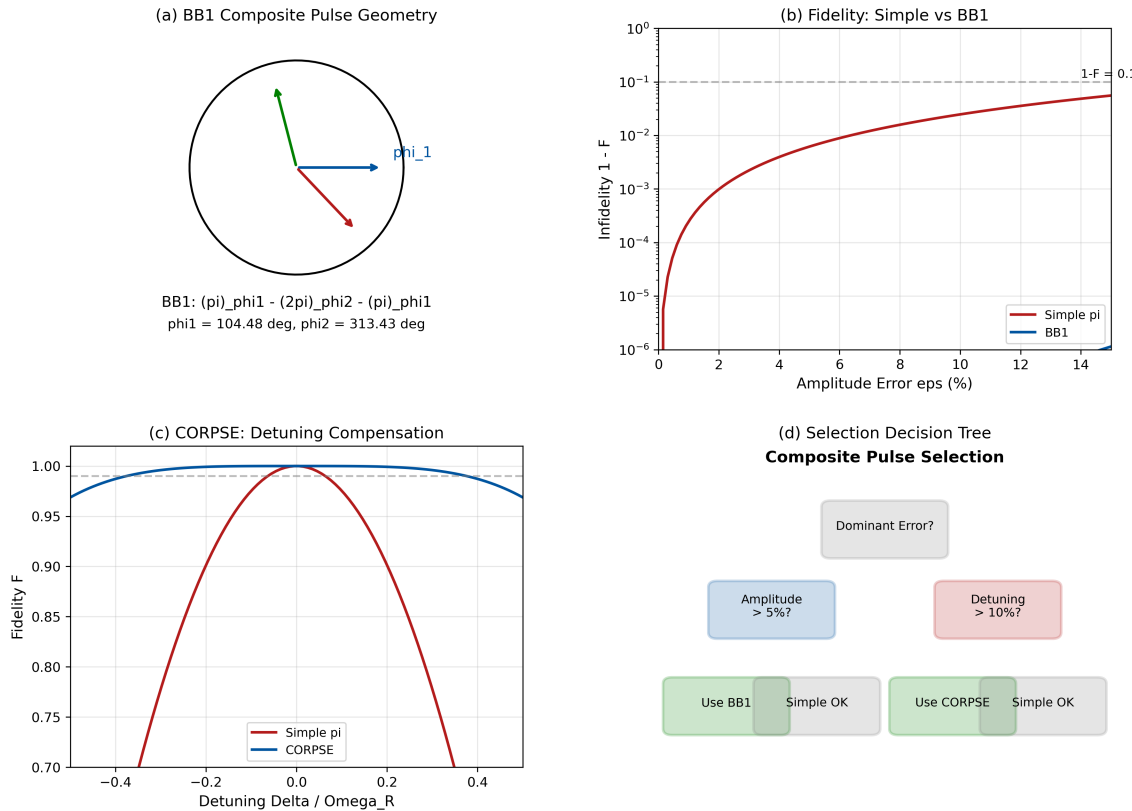


Figure 8.17: Composite pulse compensation. (a) BB1 sequence geometry on Bloch sphere showing three-pulse trajectory that returns to target state despite amplitude error. (b) Fidelity vs. amplitude error: simple π (red) vs. BB1 (blue), showing ϵ^3 suppression. (c) CORPSE sequence for detuning compensation. (d) Decision tree for composite pulse selection based on dominant error type.

8.10.6 Spatial Microwave Non-Uniformity

Wide-field QFI faces a unique challenge: the MW field varies across the field of view, creating position-dependent pulse errors.

8.10.6.1 MW Antenna Geometries

Stripline antenna (most common):

$$\Omega_R(x, y) = \Omega_0 \cdot \frac{1}{\sqrt{1 + (x/w)^2}} \cdot \cos\left(\frac{\pi y}{2L}\right) \quad (8.231)$$

Typical variation: 10–30% over 100 μm FOV.

Omega (Ω) loop antenna:

$$\Omega_R(r) = \Omega_0 \cdot \left[1 - 0.02 \left(\frac{r}{R}\right)^2\right] \quad (r < R) \quad (8.232)$$

Typical variation: 2–5% within the loop—much better uniformity.

Coplanar waveguide (CPW): Typical variation: 5–15% over 100 μm FOV.

8.10.6.2 Impact on DD Performance

For N -pulse DD, the spatially-varying fidelity is:

$$\mathcal{F}(x, y) = \mathcal{F}_{\text{ideal}} \times \left[1 - c_N \cdot \left(\frac{\Omega_R(x, y) - \Omega_0}{\Omega_0} \right)^2 \right] \quad (8.233)$$

where $c_N \approx N^2/4$ for CPMG and $c_N \approx N/10$ for XY-8.

Design Rule 2: MW Uniformity Requirements for Wide-Field DD

For <5% fidelity variation across FOV with N -pulse XY-8:

$$\frac{\delta\Omega_R}{\Omega_R} < \sqrt{\frac{0.05 \times 10}{N}} = \frac{0.71}{\sqrt{N}} \quad (8.234)$$

Numerical requirements:

- $N = 16$: MW uniformity <18%
- $N = 64$: MW uniformity <9%
- $N = 256$: MW uniformity <4.4%

8.10.7 Worked Example 8.F: Wide-Field Microwave Calibration

Worked Example 8.F: Spatially-Varying Pulse Calibration

Scenario: A wide-field QFI system has 10% microwave amplitude variation across the $100 \mu\text{m}$ FOV due to stripline antenna geometry. Design a calibration and compensation strategy for XY-64 operation.

Given Parameters:

- Field of view: $100 \times 100 \mu\text{m}^2$
- MW amplitude variation: $\pm 10\%$ (Gaussian profile from stripline)
- Pixel size: $0.5 \mu\text{m}$ (200×200 pixels)
- Target DD sequence: XY-64 (64 pulses)
- Target fidelity variation: <5% across FOV

Find:

- (a) Fidelity map without calibration
- (b) Calibration measurement protocol
- (c) Compensation strategies and trade-offs
- (d) Recommended approach for production system

8.10.7.1 Step 1: Fidelity Map Without Calibration

The MW amplitude follows a Gaussian profile from the stripline:

$$\Omega_R(x, y) = \Omega_0 \left[1 - 0.1 \times \left(\frac{r}{r_{\text{FOV}}} \right)^2 \right] \quad (8.235)$$

where $r = \sqrt{x^2 + y^2}$ and $r_{\text{FOV}} = 50 \mu\text{m}$.

At FOV center ($r = 0$): $\epsilon = 0$

At FOV edge ($r = 50 \mu\text{m}$): $\epsilon = 10\%$

For XY-64, fidelity at each position:

$$\mathcal{F}(r) = 1 - \frac{N}{10} \times \epsilon(r)^2 = 1 - 6.4 \times \epsilon(r)^2 \quad (8.236)$$

At center: $\mathcal{F}_{\text{center}} = 1.0$

At edge: $\mathcal{F}_{\text{edge}} = 1 - 6.4 \times (0.1)^2 = 0.936$

$\Delta\mathcal{F} = 6.4\% \text{ variation (exceeds 5\% target)}$

(8.237)

8.10.7.2 Step 2: Calibration Protocol

Rabi oscillation mapping:

For each pixel (i, j) :

1. Initialize NV to $|0\rangle$ (300 ns optical pumping)
2. Apply MW pulse of variable duration t (sweep 0–500 ns, 5 ns steps)
3. Measure fluorescence $I(t)$
4. Fit: $I(t) = A + B \cos(\Omega_R^{(i,j)} t) e^{-t/T_{\text{Rabi}}}$
5. Extract $\Omega_R^{(i,j)}$ for each pixel

Calibration map output:

$$\Omega_R^{\text{map}}(i, j) = \text{fitted Rabi frequency at pixel } (i, j) \quad (8.238)$$

Calibration time (wide-field parallel acquisition):

- Points per Rabi curve: 20
- Averages per point: 100
- Time per point: 100 μs
- Total: 200 ms (single-shot for entire FOV)

8.10.7.3 Step 3: Compensation Strategies

Strategy A: Restricted FOV

Use only the central region where $\epsilon < \epsilon_{\text{threshold}}$.

For $\mathcal{F} > 0.95$ with XY-64: require $\epsilon < 2.8\%$

From the spatial profile:

$$r_{\text{usable}} = r_{\text{FOV}} \times \sqrt{\frac{0.028}{0.10}} = 50 \mu\text{m} \times 0.53 = 26.5 \mu\text{m} \quad (8.239)$$

$\text{Usable FOV} = 53 \mu\text{m diameter} = 28\% \text{ of full area}$

(8.240)

Strategy B: BB1 Composite Pulses

Replace each π pulse with BB1 composite sequence:

$$\epsilon_{\text{BB1}} = \epsilon^3 \Rightarrow (0.1)^3 = 0.001 = 0.1\% \quad (8.241)$$

With BB1, XY-64 fidelity at edge:

$$\mathcal{F}_{\text{BB1}} = 1 - 6.4 \times (0.001)^2 = 1 - 6.4 \times 10^{-6} \approx 1.0 \quad (8.242)$$

$\text{BB1 composite: } \Delta\mathcal{F} < 0.001\% \text{ (excellent uniformity)}$

(8.243)

Trade-off: BB1 requires $3\times$ more pulses (192 instead of 64), reducing maximum sequence time.

Strategy C: Post-Processing Correction

Apply position-dependent sensitivity correction:

$$B_{\text{corrected}}(i, j) = B_{\text{measured}}(i, j) \times \frac{\Omega_0}{\Omega_R^{(i,j)}} \quad (8.244)$$

This corrects for sensitivity variation but **not** for fidelity loss (systematic bias remains).

8.10.7.4 Step 4: Strategy Comparison and Recommendation

Table 8.24: Compensation strategy comparison for wide-field XY-64

Strategy	Residual $\Delta\mathcal{F}$	Usable FOV	Complexity	Recommended?
None	6.4%	100%	Low	No
Restricted FOV	<5%	28%	Low	Baseline
BB1 composite	<0.001%	100%	Medium	Best
Post-processing	6.4% (bias)	100%	Low	Supplement only

Recommended protocol for production QFI:

1. Perform Rabi calibration map at system startup (200 ms)
2. Use BB1 composite pulses for all sequences with $N > 16$
3. Apply post-processing sensitivity correction
4. Re-calibrate every 4 hours or after temperature change $>2^\circ\text{C}$

Worked Example 8.F: Wide-Field Microwave Calibration

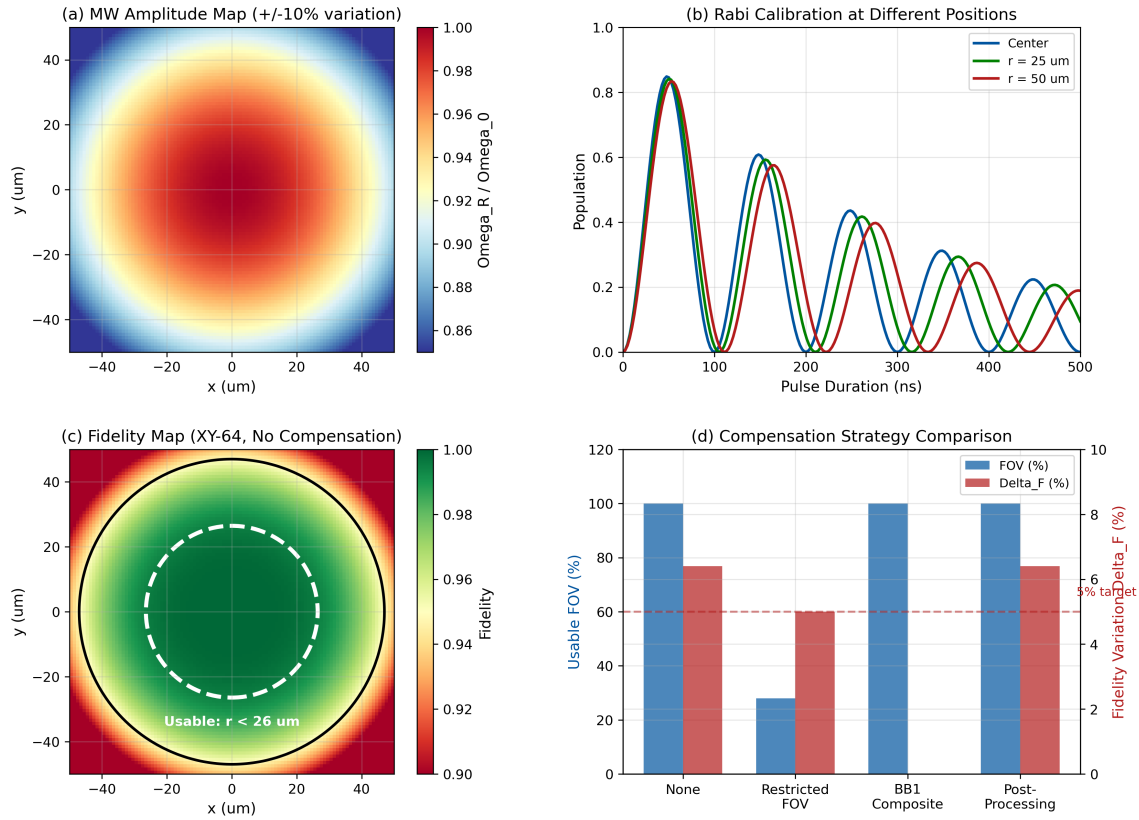


Figure 8.18: Worked Example 8.F: Wide-field MW calibration. (a) MW amplitude map across $100 \times 100 \mu\text{m}$ FOV showing 10% edge roll-off from stripline antenna. (b) Rabi oscillation data at three positions (center, mid, edge) with fitted frequencies. (c) Fidelity map for XY-64 without compensation showing 6.4% variation. (d) Comparison of compensation strategies: restricted FOV (yellow circle), BB1 composite (full FOV, green), post-processing only (full FOV with residual bias, orange).

8.10.8 Hardware Failure Modes

Beyond gradual degradation, QFI systems can experience discrete hardware failures that corrupt measurements.

8.10.8.1 MW Source Failures

Phase noise: Synthesizer phase noise converts to pulse timing jitter:

$$\sigma_\phi = \sqrt{2 \int_0^{f_c} S_\phi(f) df} \quad (8.245)$$

Specification: Phase noise $< -100 \text{ dBc/Hz}$ at 10 kHz offset for $\sigma_\phi < 1$.

IQ imbalance: Gain/phase mismatch between I and Q channels:

$$\begin{pmatrix} I' \\ Q' \end{pmatrix} = \begin{pmatrix} 1 + \alpha & 0 \\ \beta & 1 - \alpha \end{pmatrix} \begin{pmatrix} I \\ Q \end{pmatrix} \quad (8.246)$$

Specification: IQ imbalance $< 0.5 \text{ dB}$ amplitude, $< 2^\circ$ phase.

8.10.8.2 Amplifier Failures

Saturation: When input exceeds linear range:

$$P_{\text{out}} = P_{\text{sat}} \tanh \left(\frac{P_{\text{in}}}{P_{\text{sat}}} \right) \quad (8.247)$$

Mitigation: Operate at $P_{\text{in}} < P_{1\text{dB}} - 3$ dB.

Thermal drift: Gain varies with temperature:

$$G(T) = G_0[1 + \alpha_G(T - T_0)] \quad (8.248)$$

Typical: $\alpha_G \approx -0.01$ to -0.05 dB/ $^{\circ}\text{C}$.

Mitigation: Temperature stabilization to $\pm 0.5^{\circ}\text{C}$ or active power monitoring.

8.10.8.3 Timing System Failures

AWG jitter:

$$\sigma_t = \sqrt{\sigma_{\text{clock}}^2 + \sigma_{\text{DAC}}^2 + \sigma_{\text{trigger}}^2} \quad (8.249)$$

Typical: 50–500 ps for research-grade AWGs.

Trigger latency variation: Shot-to-shot delay changes.

Mitigation: Hardware triggers, minimize cable lengths, avoid software timing.

Table 8.25: Hardware failure modes and monitoring

Component	Failure Mode	Effect	Specification	Monitor
MW source	Phase noise	Timing jitter	< -100 dBc/Hz	Spectrum analyzer
MW source	IQ imbalance	Axis error	<0.5 dB, 2°	IQ calibration
Amplifier	Saturation	Clipping	$P < P_{1\text{dB}} - 3$	Power meter
Amplifier	Thermal drift	Gain drift	$\pm 0.5^{\circ}\text{C}$ stability	Thermistor
AWG	Clock jitter	Timing error	<100 ps	Eye diagram
Trigger	Latency variation	Sync error	<10 ns	Oscilloscope

Section 8.X.5: Hardware Failure Modes

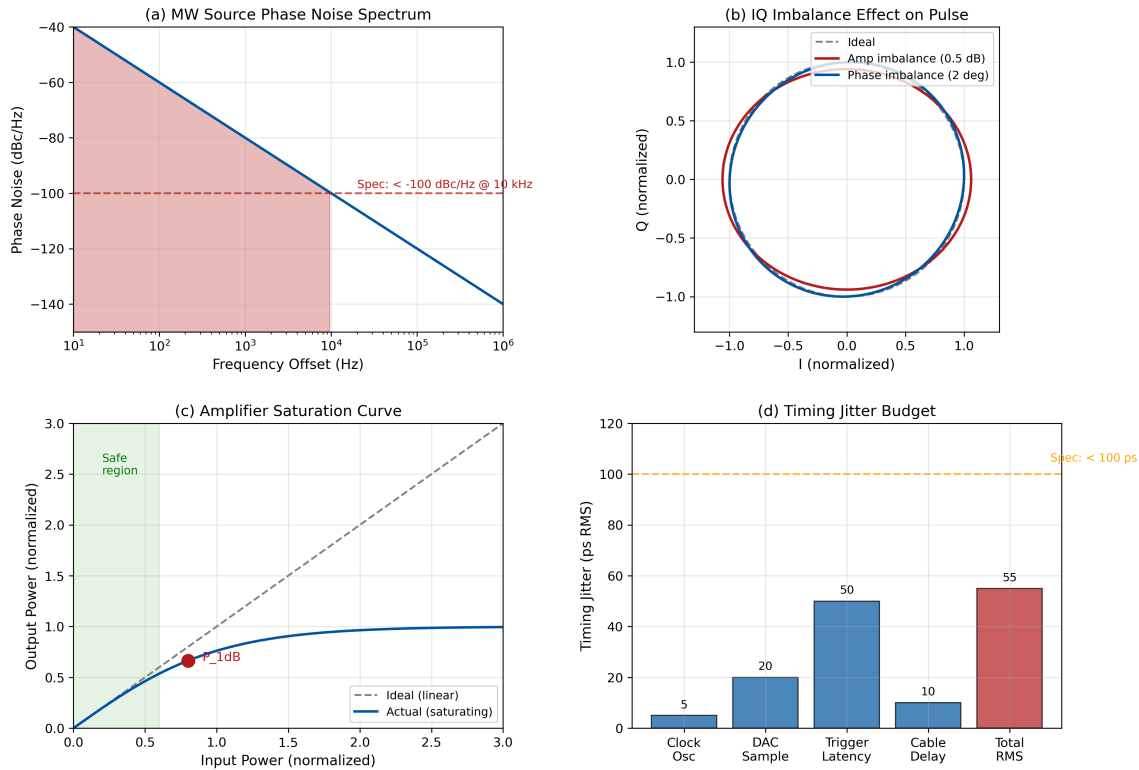


Figure 8.19: Hardware failure modes. (a) Phase noise spectrum and resulting timing jitter distribution. (b) IQ imbalance effect: intended circular trajectory (dashed) vs. actual elliptical trajectory (solid). (c) Amplifier saturation curve showing $P_{1\text{dB}}$ compression point. (d) Timing jitter sources in the pulse generation chain: clock → DAC → trigger → MW output.

8.10.9 Diagnostic Protocols

Systematic diagnostics are essential for identifying and correcting pulse errors.

8.10.9.1 Rabi Oscillation Calibration

Procedure:

1. Initialize NV to $|0\rangle$ (300 ns, 532 nm)
2. Apply MW pulse of variable duration t (sweep 0–500 ns, 5 ns steps)
3. Readout fluorescence (300 ns window)
4. Average over $M = 10^4$ repetitions
5. Fit: $I(t) = A - B \cos(\Omega_R t) e^{-t/T_{\text{Rabi}}}$

Extracted parameters:

- Ω_R : Rabi frequency ⇒ MW amplitude calibration
- T_{Rabi} : Rabi decay ⇒ MW inhomogeneity indicator
- A, B : Contrast parameters ⇒ ODMR contrast

Acceptance criteria:

- Ω_R within 5% of target
- $T_{\text{Rabi}} > 5/\Omega_R$ (at least 5 visible oscillations)
- Fit residual <5% RMS

8.10.9.2 Echo Decay Verification

Measure T_2 via Hahn echo at multiple τ values:

1. Sweep τ from 1 μs to 100 μs
2. Fit decay: $S(\tau) = A \cdot e^{-(\tau/T_2)^n} + B$
3. Verify T_2 matches expected value
4. Deviation indicates pulse errors or environmental changes

8.10.9.3 Randomized Benchmarking (Advanced)

For high-precision gate fidelity measurement:

1. Generate random sequence of m Clifford gates
2. Append recovery gate to return to $|0\rangle$
3. Measure survival probability $p(m)$
4. Repeat for $K = 50$ random sequences per length
5. Fit: $p(m) = A \cdot r^m + B$
6. Extract average gate fidelity: $\mathcal{F} = 1 - (1 - r)/2$

Design Rule 3: Calibration Schedule for Production QFI

System startup:

- Full Rabi map across FOV (2 minutes)
- Randomized benchmarking verification (5 minutes)
- ODMR frequency centering (1 minute)

Hourly:

- π -pulse amplitude check at FOV center (10 seconds)
- ODMR frequency tracking (10 seconds)

Per wafer/sample:

- Echo decay verification (30 seconds)
- Sensitivity validation with reference target (1 minute)

Daily:

- Full recalibration if temperature drift $>2^\circ\text{C}$
- Hardware health check (amplifier power, timing)

Section 8.X.6: Diagnostic Protocols

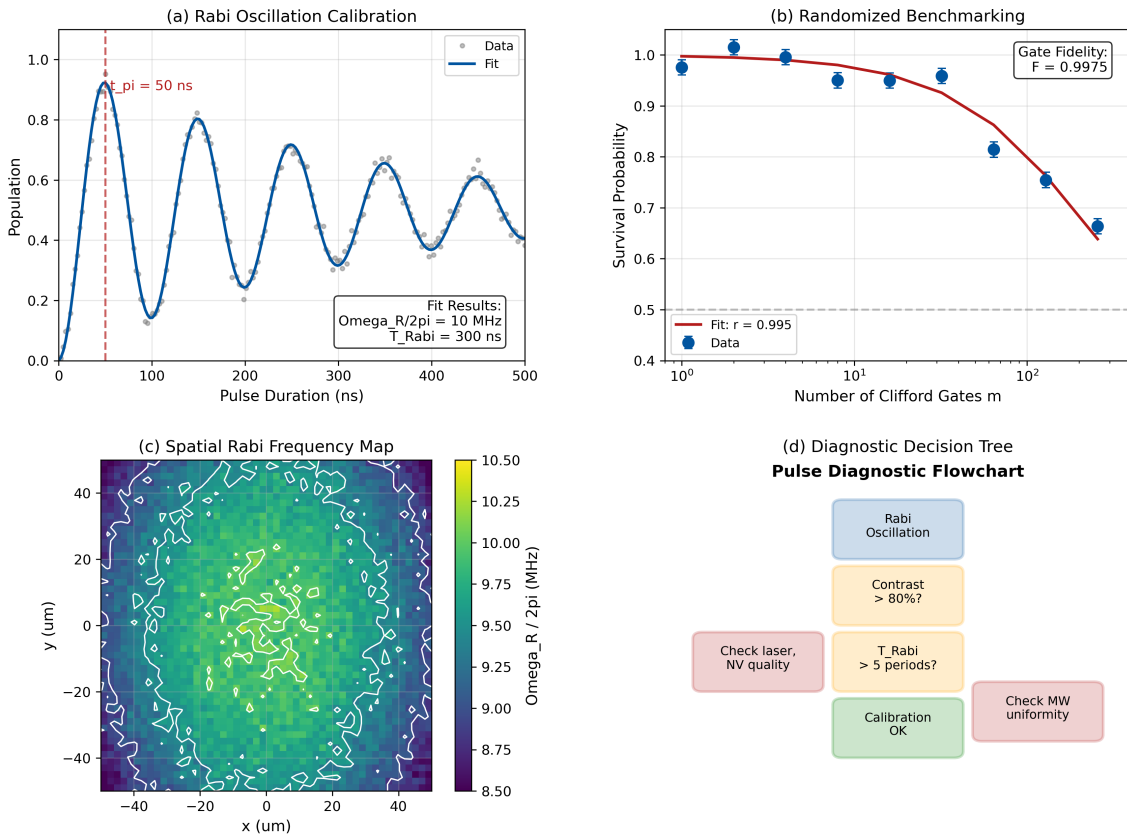


Figure 8.20: Diagnostic protocols. (a) Rabi oscillation measurement with fit showing $\Omega_R = 10 \text{ MHz}$ and $T_{\text{Rabi}} = 2 \mu\text{s}$. (b) Echo decay curve for T_2 extraction. (c) Spatial Rabi frequency map across FOV showing calibration quality. (d) Diagnostic decision tree for troubleshooting: symptom → likely cause → corrective action.

8.10.10 Summary: Pulse Error Management

Table 8.26: Pulse error management summary

Error Source	Primary Mitigation	Secondary Mitigation
Amplitude error	XY-8 phase cycling	BB1 composite pulses
Phase error	XY-8 phase cycling	IQ calibration
Timing jitter	High-quality AWG ($<100 \text{ ps}$)	Longer π pulses (lower Ω_R)
Detuning	ODMR tracking	CORPSE composite pulses
Spatial non-uniformity	Omega-loop antenna	BB1 + post-processing
Thermal drift	Temperature stabilization	Hourly recalibration

Design Rule 4: Pulse Error Design Rules Summary

1. Use XY-8 (not CPMG) for all sequences with $N > 8$
2. Timing jitter is often the dominant error—specify AWG carefully
3. For $N > 64$ with MW uniformity $>5\%$: use BB1 composite pulses
4. Calibrate Rabi frequency at startup; track ODMR frequency hourly
5. Budget 10% of measurement time for calibration in production
6. Monitor amplifier temperature; recalibrate after $>2^\circ\text{C}$ drift

8.10.11 QFI-Specific Failure Modes

Beyond hardware imperfections (Sections 8.10.2–8.10.10), pulse sequences can fail to provide meaningful *imaging* information even when sensing performance remains acceptable. These QFI-specific failure modes arise from the reconstruction requirements:

8.10.11.1 Spectral Aliasing

The comb-like filter function of DD sequences (Fig. 8.9) samples the field spectrum at discrete frequencies $f_n = n/(2\tau)$. If the source generates broadband fields, spectral components outside the filter passband are not measured but *alias* into the reconstruction:

$$S_{\text{aliased}}(\mathbf{r}) = S_{\text{true}}(\mathbf{r}) + \sum_{n \notin \text{passband}} S_n(\mathbf{r}) \cdot \text{fold}(f_n \rightarrow f_{\text{measured}}) \quad (8.250)$$

Mitigation: Use swept-frequency protocols (Section 8.8.6) or design filter bandwidth to exceed expected source bandwidth by $> 2\times$.

8.10.11.2 Non-Stationarity During Measurement

Long DD sequences ($n > 64$, total time $>100 \mu\text{s}$) assume the field is stationary during the measurement. If the source varies on timescales comparable to or shorter than the sequence duration:

$$\Delta F_{\text{ns}} \approx \frac{\partial F}{\partial t} \cdot n\tau \quad (8.251)$$

this variation appears as additional “noise” that cannot be distinguished from sensor decoherence.

Mitigation: Limit sequence duration to $n\tau < \tau_{\text{source}}/10$, where τ_{source} is the source variation timescale. For IC switching transients ($\tau_{\text{source}} \sim 1 \mu\text{s}$), this restricts $n\tau < 100 \text{ ns}$.

8.10.11.3 Spatially-Varying Measurement Operator

In wide-field QFI, MW non-uniformity (Section 8.10.6) causes the effective measurement operator to vary across the field of view:

$$\mathcal{M}_{\text{seq}}(\mathbf{r}) \neq \mathcal{M}_{\text{seq}}(\mathbf{r}') \quad (8.252)$$

If the reconstruction algorithm assumes a uniform \mathcal{M} , this mismatch propagates directly to the model-mismatch penalty:

$$\Gamma_{\text{mm}} \approx 1 - \left\langle \frac{\delta \mathcal{M}}{\mathcal{M}} \right\rangle_{\text{FOV}}^2 \quad (8.253)$$

Mitigation: Either (a) calibrate position-dependent $\mathcal{M}(\mathbf{r})$ and include in reconstruction, or (b) restrict usable FOV to regions with $< 2\%$ MW variation (per DR 8.4).

Table 8.27: QFI-specific failure modes and mitigation strategies.

Failure Mode	Symptom	Affected Metric	Mitigation
Spectral aliasing	Ghost sources in reconstruction	Γ_{inv}	Widen filter bandwidth
Non-stationarity	Excess “noise” floor	$\text{SNR}, \Gamma_{\text{inv}}$	Shorten sequence
Spatial \mathcal{M} variation	Position-dependent bias	Γ_{mm}	Calibrate or restrict FOV
Channel coupling	Cross-talk in extraction	Φ_{multi}	Q-OTF diagonalization

8.11 Pulse Sequences and the Quantum OTF

8.11.1 Multi-Physics Q-OTF Matrix

Pulse sequences control the off-diagonal elements of the Q-OTF matrix:

$$\begin{pmatrix} S_B \\ S_T \\ S_\varepsilon \\ S_E \end{pmatrix} = \begin{pmatrix} \text{Q-OTF}_{BB} & \text{Q-OTF}_{BT} & \cdots \\ \text{Q-OTF}_{TB} & \text{Q-OTF}_{TT} & \cdots \\ \vdots & \vdots & \ddots \end{pmatrix} \begin{pmatrix} B \\ T \\ \varepsilon \\ E \end{pmatrix} \quad (8.254)$$

The goal is Q-OTF diagonalization:

$$\frac{|\text{Q-OTF}_{ij}|}{|\text{Q-OTF}_{ii}|} < 0.01 \quad (i \neq j) \quad (8.255)$$

Key Equation: Pulse Sequences Enable $\Phi_{\text{multi}} > 1$

Channel separation via pulse sequence algebra is **prerequisite** for achieving $\Phi_{\text{multi}} > 1$. Without diagonalized Q-OTF, multi-physics measurements provide no additional reconstruction information.

8.11.1.1 Experimental Verification of Q-OTF Diagonalization

The diagonalization criterion (Eq. 8.11.1) can be experimentally verified using reference perturbations:

Protocol:

1. Apply known B-only perturbation (calibrated coil, no heating): measure S_B, S_T, S_ε
2. Apply known T-only perturbation (laser heating, no current): measure S_B, S_T, S_ε
3. Compute cross-talk ratios: $|S_T^{(B\text{-only})}| / |S_B^{(B\text{-only})}|$ should be < 0.01
4. If cross-talk exceeds 1%, adjust pulse sequence parameters or measurement protocol

Practical note: For IC applications, a lithographic test structure with independent heater and current paths enables clean reference generation.

8.11.2 QFM vs QFI: Two Modes of Pulse Sequence Design

Pulse sequences serve fundamentally different purposes depending on whether the goal is Quantum Field Metrology (QFM) or Quantum Field Imaging (QFI):

Table 8.28: Pulse sequence design philosophy: QFM vs QFI.

Aspect	QFM (Field Measurement)	QFI (Source Reconstruction)
Primary goal	Maximize sensitivity η_q	Enable invertible measurement
Sequence criterion	Highest SNR for target field	Q-OTF diagonalization
Multi-physics handling	Suppress cross-talk	Separate channels for joint inversion
Success metric	Field map accuracy	Source reconstruction fidelity Γ_{inv}
Failure mode	Low SNR	Ill-conditioned inverse problem

In QFM, pulse sequences are optimized to maximize sensitivity to a *known* field component—the goal is the best possible field map $F(\mathbf{r})$. Cross-talk from other physics channels is treated as contamination to be suppressed.

In QFI, the perspective shifts: pulse sequences must encode sufficient information for *reconstruction* of the source $S(\mathbf{r})$ from measurements. This requires not just high SNR, but also:

- **Channel separability:** Independent extraction of B , T , ε , E enables the multi-physics forward model $\mathbf{G}_{\text{multi}}$
- **Conditioning:** The measurement matrix \mathbf{A} (Eq. 8.64) must have $\kappa(\mathbf{A}) < 100$
- **Information completeness:** The Q-OTF bandwidth must exceed source spatial frequencies

Key insight: A pulse sequence that is optimal for QFM (maximum single-channel sensitivity) may be suboptimal for QFI if it creates channel coupling that degrades Γ_{inv} .

8.12 Chapter Summary

8.12.1 Key Results

1. **Ramsey Protocol:** Senses all static fields with $\eta_B \propto 1/(\gamma_B C \sqrt{I_0 T_2^*})$
2. **Spin Echo:** Cancels quasi-static contributions; senses AC at $f = 1/(2\tau)$
3. **Pulse Sequence Algebra:** Four independent measurements extract B , T , ε , E
4. **Filter Function:** Quantifies frequency selectivity; enables noise spectroscopy
5. **Dynamical Decoupling:** XY-8/CPMG extend coherence by $n^{0.5-0.7}$
6. **Spatiotemporal Control:** Combining temporal sequences with spatial MW structuring

8.12.2 Design Rules Summary

Rule	Statement
DR 8.1	Pulse sequence algebra enables channel separation; require $\kappa(\mathbf{A}) < 100$
DR 8.2	Use XY-8 with $n = 8-64$ for robust coherence extension
DR 8.3	Target DD frequencies 1–100 MHz for IC power grid analysis
DR 8.4	MW uniformity $< 2\%$ required for $n > 16$ DD sequences
DR 8.5	Q-OTF diagonalization via pulse sequences prerequisite for $\Phi_{\text{multi}} > 1$
DR 8.6	For spatiotemporal control, design zone-specific sequences with common clock

Table 8.29: Design rules from Chapter 8.

Problems and Solution Hints

Problem 8.1: Ramsey Sensitivity with Non-Gaussian Noise

An NV sensor operates in an environment with $1/f$ noise characterized by $S(\omega) = S_0/\omega$ with $S_0 = 10^{-12} \text{ T}^2$.

- (a) Using the filter function formalism, derive the decoherence function $\chi(\tau)$.
- (b) Numerically determine the optimal τ maximizing sensitivity.
- (c) Compare with the Gaussian noise approximation. What is the error?

Hint: $\int_0^\infty \frac{\text{sinc}^2(x)}{x} dx$ requires numerical evaluation.

Problem 8.2: Four-Channel Multi-Physics Extraction

Design a measurement protocol to extract B , T , ε , and E from an NV sensor.

- (a) Write the complete 4×4 coupling matrix \mathbf{A} with numerical coefficients.
- (b) Calculate the condition number $\kappa(\mathbf{A})$.
- (c) If $\kappa > 100$, propose modifications to improve conditioning.
- (d) Simulate noise propagation for 1% measurement uncertainty.

Hint: Use $\gamma_B = 28 \text{ GHz/T}$, $dD/dT = -74 \text{ kHz/K}$, strain coupling $\sim 1 \text{ MHz/GPa}$.

Problem 8.3: Spatiotemporal DD Design

Design a zone-selective DD protocol for a $100 \times 100 \mu\text{m}$ FOV with three frequency bands.

- (a) Specify zone boundaries, sequences, and target frequencies.
- (b) Calculate required MW antenna specifications for < 5% inter-zone crosstalk.
- (c) Estimate the throughput advantage over serial single-frequency scanning.

Hint: Consider stripline arrays with individual phase control.

Problem 8.4: Optimal Control Sequence Design

Using the GRAPE algorithm framework:

- (a) Formulate the cost function for maximizing sensitivity to 1 MHz AC fields while rejecting DC.
- (b) Derive the gradient of the cost function with respect to pulse amplitudes.
- (c) Compare GRAPE-optimized sequence with standard XY-8 for the same total time.

Hint: Use piecewise-constant pulses with 10 ns resolution.

Problem 8.5: MW Non-Uniformity Compensation

A QFI system has MW field variation of 8% across $50 \mu\text{m}$ FOV.

- (a) Calculate maximum usable n for CPMG and XY-8 with 0.1 rad error budget.
- (b) Design a composite pulse sequence to extend this limit by 2 \times .
- (c) Propose a calibration protocol to map and correct position-dependent errors.

Hint: Consider CORPSE or BB1 composite pulses.

References

Foundational Pulse Sequence Methods

- [8.1] E. L. Hahn, “Spin Echoes,” *Phys. Rev.* **80**, 580–594 (1950). — *The original spin echo paper; foundational for all refocusing sequences.*
- [8.2] H. Y. Carr and E. M. Purcell, “Effects of Diffusion on Free Precession in Nuclear Magnetic Resonance Experiments,” *Phys. Rev.* **94**, 630–638 (1954). — *Introduction of the CPMG multi-pulse sequence.*
- [8.3] S. Meiboom and D. Gill, “Modified Spin-Echo Method for Measuring Nuclear Relaxation Times,” *Rev. Sci. Instrum.* **29**, 688–691 (1958). — *Phase cycling modification that improves CPMG robustness.*
- [8.4] N. F. Ramsey, “A Molecular Beam Resonance Method with Separated Oscillating Fields,” *Phys. Rev.* **78**, 695–699 (1950). — *Original Ramsey interferometry paper.*
- [8.5] J. S. Waugh, L. M. Huber, and U. Haeberlen, “Approach to High-Resolution NMR in Solids,” *Phys. Rev. Lett.* **20**, 180–182 (1968). — *Average Hamiltonian theory foundations.*
- [8.6] U. Haeberlen, *High Resolution NMR in Solids: Selective Averaging*, (Academic Press, New York, 1976). — *Comprehensive treatment of average Hamiltonian theory.*
- [8.7] C. P. Slichter, *Principles of Magnetic Resonance*, 3rd ed., (Springer, Berlin, 1990). — *Standard textbook for NMR/ESR pulse sequence fundamentals.*
- [8.8] R. R. Ernst, G. Bodenhausen, and A. Wokaun, *Principles of Nuclear Magnetic Resonance in One and Two Dimensions*, (Clarendon Press, Oxford, 1987). — *Comprehensive NMR pulse sequence theory.*
- [8.9] L. Viola and S. Lloyd, “Dynamical suppression of decoherence in two-state quantum systems,” *Phys. Rev. A* **58**, 2733–2744 (1998). — *Theoretical foundation for dynamical decoupling.*
- [8.10] L. Viola, E. Knill, and S. Lloyd, “Dynamical Decoupling of Open Quantum Systems,” *Phys. Rev. Lett.* **82**, 2417–2421 (1999). — *General DD theory for arbitrary noise.*

NV Center Dynamical Decoupling

- [8.11] L. Childress, M. V. Gurudev Dutt, J. M. Taylor, A. S. Zibrov, F. Jelezko, J. Wrachtrup, P. R. Hemmer, and M. D. Lukin, “Coherent Dynamics of Coupled Electron and Nuclear Spin Qubits in Diamond,” *Science* **314**, 281–285 (2006). — *Early demonstration of coherent control in NV centers.*
- [8.12] G. de Lange, Z. H. Wang, D. Ristè, V. V. Dobrovitski, and R. Hanson, “Universal Dynamical Decoupling of a Single Solid-State Spin from a Spin Bath,” *Science* **330**, 60–63 (2010). — *Demonstration of XY-8 and other DD sequences on single NV.*
- [8.13] C. A. Ryan, J. S. Hodges, and D. G. Cory, “Robust Decoupling Techniques to Extend Quantum Coherence in Diamond,” *Phys. Rev. Lett.* **105**, 200402 (2010). — *Systematic comparison of DD sequences for NV.*
- [8.14] B. Naydenov, F. Dolde, L. T. Hall, C. Shin, H. Fedder, L. C. L. Hollenberg, F. Jelezko, and J. Wrachtrup, “Dynamical Decoupling of a Single-Electron Spin at Room Temperature,” *Phys. Rev. B* **83**, 081201(R) (2011). — *Room-temperature DD demonstration.*

- [8.15] N. Bar-Gill, L. M. Pham, A. Jarmola, D. Budker, and R. L. Walsworth, “Solid-State Electronic Spin Coherence Time Approaching One Second,” *Nat. Commun.* **4**, 1743 (2013). — *Record coherence times with isotopic purification and DD.*
- [8.16] A. M. Souza, G. A. Álvarez, and D. Suter, “Robust Dynamical Decoupling for Quantum Computing and Quantum Memory,” *Phys. Rev. Lett.* **106**, 240501 (2011). — *Analysis of robust DD sequence families.*
- [8.17] G. S. Uhrig, “Keeping a Quantum Bit Alive by Optimized π -Pulse Sequences,” *Phys. Rev. Lett.* **98**, 100504 (2007). — *Introduction of UDD sequences.*
- [8.18] G. S. Uhrig, “Exact Results on Dynamical Decoupling by π Pulses in Quantum Information Processes,” *New J. Phys.* **10**, 083024 (2008). — *Theoretical analysis of UDD optimality.*
- [8.19] G. de Lange, D. Ristè, V. V. Dobrovitski, and R. Hanson, “Single-Spin Magnetometry with Multipulse Sensing Sequences,” *Phys. Rev. Lett.* **106**, 080802 (2011). — *Application of DD to magnetometry.*
- [8.20] L. M. Pham, N. Bar-Gill, C. Belthangady, D. Le Sage, P. Cappellaro, M. D. Lukin, A. Yacoby, and R. L. Walsworth, “Enhanced solid-state multispin metrology using dynamical decoupling,” *Phys. Rev. B* **86**, 045214 (2012). — *DD for ensemble magnetometry.*

Filter Function Formalism and Noise Spectroscopy

- [8.21] L. Cywiński, R. M. Lutchyn, C. P. Nave, and S. Das Sarma, “How to Enhance Dephasing Time in Superconducting Qubits,” *Phys. Rev. B* **77**, 174509 (2008). — *Filter function formalism for DD sequences.*
- [8.22] M. J. Biercuk, A. C. Doherty, and H. Uys, “Dynamical decoupling sequence construction as a filter-design problem,” *J. Phys. B* **44**, 154002 (2011). — *Connection between DD and digital filter design.*
- [8.23] G. A. Álvarez and D. Suter, “Measuring the Spectrum of Colored Noise by Dynamical Decoupling,” *Phys. Rev. Lett.* **107**, 230501 (2011). — *Noise spectroscopy via DD.*
- [8.24] J. Bylander, S. Gustavsson, F. Yan, F. Yoshihara, K. Harrabi, G. Fitch, D. G. Cory, Y. Nakamura, J.-S. Tsai, and W. D. Oliver, “Noise spectroscopy through dynamical decoupling with a superconducting flux qubit,” *Nat. Phys.* **7**, 565–570 (2011). — *Experimental noise spectroscopy demonstration.*
- [8.25] N. Bar-Gill, L. M. Pham, C. Belthangady, D. Le Sage, P. Cappellaro, J. R. Maze, M. D. Lukin, A. Yacoby, and R. L. Walsworth, “Suppression of spin-bath dynamics for improved coherence of multi-spin-qubit systems,” *Nat. Commun.* **3**, 858 (2012). — *Noise characterization via coherence measurements.*
- [8.26] Y. Romach, C. Müller, T. Unden, L. J. Rogers, T. Isoda, K. M. Itoh, M. Markham, A. Stacey, J. Meijer, S. Pezzagna, B. Naydenov, L. P. McGuinness, N. Bar-Gill, and F. Jelezko, “Spectroscopy of Surface-Induced Noise Using Shallow Spins in Diamond,” *Phys. Rev. Lett.* **114**, 017601 (2015). — *Surface noise spectroscopy.*
- [8.27] T. Yuge, S. Sasaki, and Y. Hirayama, “Measurement of the Noise Spectrum Using a Multiple-Pulse Sequence,” *Phys. Rev. Lett.* **107**, 170504 (2011). — *Noise spectrum reconstruction methods.*

- [8.28] L. M. Norris, G. A. Paz-Silva, and L. Viola, “Qubit Noise Spectroscopy for Non-Gaussian Dephasing Environments,” *Phys. Rev. Lett.* **116**, 150503 (2016). — *Extension to non-Gaussian noise.*
- [8.29] Y. Sung, F. Beaudoin, L. M. Norris, F. Yan, D. K. Kim, J. Y. Qiu, U. von Lüpke, J. L. Yoder, T. P. Orlando, S. Gustavsson, L. Viola, and W. D. Oliver, “Non-Gaussian noise spectroscopy with a superconducting qubit sensor,” *Nat. Commun.* **10**, 3715 (2019). — *Advanced noise spectroscopy techniques.*
- [8.30] V. M. Frey, S. Mavadia, L. M. Norris, W. de Ferranti, D. Lucarelli, L. Viola, and M. J. Biercuk, “Application of optimal band-limited control protocols to quantum noise sensing,” *Nat. Commun.* **11**, 6421 (2020). — *Optimal control for noise spectroscopy.*

Composite Pulses and Error Compensation

- [8.31] M. H. Levitt, “Composite Pulses,” *Prog. Nucl. Magn. Reson. Spectrosc.* **18**, 61–122 (1986). — *Comprehensive review of composite pulse theory.*
- [8.32] S. Wimperis, “Broadband, Narrowband, and Passband Composite Pulses for Use in Advanced NMR Experiments,” *J. Magn. Reson. A* **109**, 221–231 (1994). — *BB1 and other broadband composite pulses.*
- [8.33] H. K. Cummins, G. Llewellyn, and J. A. Jones, “Tackling systematic errors in quantum logic gates with composite rotations,” *Phys. Rev. A* **67**, 042308 (2003). — *Composite pulses for quantum computing.*
- [8.34] K. R. Brown, A. W. Harrow, and I. L. Chuang, “Arbitrarily accurate composite pulse sequences,” *Phys. Rev. A* **70**, 052318 (2004). — *Systematic construction of composite sequences.*
- [8.35] M. Bando, T. Ichikawa, Y. Kondo, and M. Nakahara, “Concatenated Composite Pulses Compensating Simultaneous Systematic Errors,” *J. Phys. Soc. Jpn.* **82**, 014004 (2013). — *Multi-error composite pulse design.*
- [8.36] G. T. Genov, D. Schraft, T. Halfmann, and N. V. Vitanov, “Correction of Arbitrary Field Errors in Population Inversion of Quantum Systems by Universal Composite Pulses,” *Phys. Rev. Lett.* **113**, 043001 (2014). — *Universal composite pulse methods.*
- [8.37] G. H. Low, T. J. Yoder, and I. L. Chuang, “Optimal arbitrarily accurate composite pulse sequences,” *Phys. Rev. A* **89**, 022341 (2014). — *Optimal composite pulse theory.*
- [8.38] C. Kabytayev, T. J. Green, K. Khodjasteh, M. J. Biercuk, L. Viola, and K. R. Brown, “Robustness of composite pulses to time-dependent control noise,” *Phys. Rev. A* **90**, 012316 (2014). — *Time-dependent error analysis.*
- [8.39] L. M. K. Vandersypen and I. L. Chuang, “NMR techniques for quantum control and computation,” *Rev. Mod. Phys.* **76**, 1037–1069 (2005). — *Review including composite pulse applications.*
- [8.40] J. T. Merrill and K. R. Brown, “Progress in Compensating Pulse Sequences for Quantum Computation,” *Adv. Chem. Phys.* **154**, 241–294 (2014). — *Comprehensive review of error compensation.*

Optimal Control and Machine Learning Methods

- [8.41] N. Khaneja, T. Reiss, C. Kehlet, T. Schulte-Herbrüggen, and S. J. Glaser, “Optimal Control of Coupled Spin Dynamics: Design of NMR Pulse Sequences by Gradient Ascent Algorithms,” *J. Magn. Reson.* **172**, 296–305 (2005). — *The GRAPE algorithm for optimal pulse design.*
- [8.42] F. Poggiali, P. Cappellaro, and N. Fabbri, “Optimal Control for One-Qubit Quantum Sensing,” *Phys. Rev. X* **8**, 021059 (2018). — *Optimal control applied to NV sensing.*
- [8.43] P. Rembold, N. Oshnik, M. M. Müller, S. Montangero, T. Calarco, and E. Neu, “Introduction to Quantum Optimal Control for Quantum Sensing with Nitrogen-Vacancy Centers in Diamond,” *AVS Quantum Sci.* **2**, 024701 (2020). — *Tutorial on QOC for NV sensing.*
- [8.44] C. Bonato, M. S. Blok, H. T. Dinani, D. W. Berry, M. L. Markham, D. J. Twitchen, and R. Hanson, “Optimized Quantum Sensing with a Single Electron Spin Using Real-Time Adaptive Measurements,” *Nat. Nanotechnol.* **11**, 247–252 (2016). — *Adaptive Bayesian sensing protocols.*
- [8.45] Y. Baum, M. Amico, S. Howell, M. Hush, M. Liuzzi, P. Mundada, T. Merkh, A. R. R. Carvalho, and M. J. Biercuk, “Experimental Deep Reinforcement Learning for Error-Robust Gate-Set Design on a Superconducting Quantum Computer,” *PRX Quantum* **2**, 040324 (2021). — *RL for quantum control optimization.*
- [8.46] M. Y. Niu, S. Boixo, V. N. Smelyanskiy, and H. Neven, “Universal quantum control through deep reinforcement learning,” *npj Quantum Inf.* **5**, 33 (2019). — *Deep RL for quantum control.*
- [8.47] M. Dalgaard, F. Motzoi, J. J. Sørensen, and J. Sherson, “Global optimization of quantum dynamics with AlphaZero deep exploration,” *npj Quantum Inf.* **6**, 6 (2020). — *AI-based pulse optimization.*
- [8.48] C. Noel, P. Niroula, D. Zhu, A. Risinger, L. Egan, D. Biswas, M. Cetina, A. V. Gorshkov, M. J. Gullans, D. A. Huse, and C. Monroe, “Measurement-induced quantum phases realized in a trapped-ion quantum computer,” *Nat. Phys.* **18**, 760–764 (2022). — *Advanced quantum control demonstrations.*
- [8.49] M. Werninghaus, D. J. Egger, F. Roy, S. Machnes, F. K. Wilhelm, and S. Filipp, “Leakage reduction in fast superconducting qubit gates via optimal control,” *npj Quantum Inf.* **7**, 14 (2021). — *Optimal control for error reduction.*
- [8.50] N. Wittler, F. Roy, K. Pack, M. Werninghaus, A. S. Roy, D. J. Egger, S. Filipp, F. K. Wilhelm, and S. Machnes, “Integrated Tool Set for Control, Calibration, and Characterization of Quantum Devices Applied to Superconducting Qubits,” *Phys. Rev. Appl.* **15**, 034080 (2021). — *Integrated calibration frameworks.*

Wide-Field Imaging and Semiconductor Applications

- [8.51] D. R. Glenn, D. B. Bucher, J. Lee, M. D. Lukin, H. Park, and R. L. Walsworth, “High-Resolution Magnetic Resonance Spectroscopy Using a Solid-State Spin Sensor,” *Nature* **555**, 351–354 (2018). — *High-resolution spectroscopy with NV.*
- [8.52] E. V. Levine, M. J. Turner, P. Kehayias, C. A. Hart, N. Langellier, R. Trubko, D. R. Glenn, R. R. Fu, and R. L. Walsworth, “Principles and techniques of the quantum diamond microscope,” *Nanophotonics* **8**, 1945–1973 (2019). — *Comprehensive QDM methodology paper.*

- [8.53] M. J. Turner, N. Langellier, R. Bainbridge, D. Walters, S. Meesala, T. M. Babinec, P. Kehayias, A. Yacoby, E. Hu, M. Lončar, R. L. Walsworth, and E. V. Levine, “Magnetic Field Fingerprinting of Integrated-Circuit Activity with a Quantum Diamond Microscope,” *Phys. Rev. Appl.* **14**, 014097 (2020). — *IC analysis with wide-field NV imaging.*
- [8.54] P. Kehayias, E. V. Levine, L. Bougas, A. Hruby, J. Henshaw, C. A. Hart, P. Schwindt, and V. M. Acosta, “Measurement and simulation of the magnetic fields from a 555 timer integrated circuit using a quantum diamond microscope and finite-element analysis,” *Phys. Rev. Appl.* **17**, 014021 (2022). — *IC current imaging demonstration.*
- [8.55] C. A. Hart, J. M. Schloss, M. J. Turner, P. J. Scheidegger, E. Bauch, and R. L. Walsworth, “N-V–Diamond Magnetic Microscopy Using a Double Quantum 4-Ramsey Protocol,” *Phys. Rev. Appl.* **15**, 044020 (2021). — *Advanced Ramsey protocols for imaging.*
- [8.56] J.-P. Tetienne, N. Dotschuk, D. A. Broadway, A. Stacey, D. A. Simpson, and L. C. L. Hollenberg, “Quantum imaging of current flow in graphene,” *Sci. Adv.* **3**, e1602429 (2017). — *Current imaging in 2D materials.*
- [8.57] A. Nowodzinski, M. Chipaux, L. Toraille, V. Jacques, J.-F. Roch, and T. Debuisschert, “Nitrogen-Vacancy centers in diamond for current imaging at the redistributive layer level of Integrated Circuits,” *Microelectron. Reliab.* **55**, 1549–1553 (2015). — *Early IC application of NV imaging.*
- [8.58] S. E. Lillie, N. Dotschuk, D. A. Broadway, D. L. Creedon, L. C. L. Hollenberg, and J.-P. Tetienne, “Imaging Graphene Field-Effect Transistors on Diamond Using Nitrogen-Vacancy Microscopy,” *Phys. Rev. Appl.* **12**, 024018 (2019). — *Device-level imaging.*
- [8.59] M. J. H. Ku, T. X. Zhou, Q. Li, Y. J. Shin, J. K. Shi, C. Burch, L. E. Anderson, A. T. Pierce, Y. Xie, A. Hamo, U. Vool, H. Zhang, F. Casola, T. Taniguchi, K. Watanabe, M. M. Fogler, P. Kim, A. Yacoby, and R. L. Walsworth, “Imaging viscous flow of the Dirac fluid in graphene,” *Nature* **583**, 537–541 (2020). — *Advanced current flow imaging.*
- [8.60] M. L. Palm, C. A. Hart, J. M. Schloss, M. J. Turner, J. Kucska, S. Bogdanovic, and R. L. Walsworth, “Imaging of submicroampere currents in bilayer graphene using a scanning diamond magnetometer,” *Phys. Rev. Appl.* **17**, L061001 (2022). — *High-sensitivity current detection.*

Nanoscale NMR and Molecular Spectroscopy

- [8.61] H. J. Mamin, M. Kim, M. H. Sherwood, C. T. Rettner, K. Ohno, D. D. Awschalom, and D. Rugar, “Nanoscale Nuclear Magnetic Resonance with a Nitrogen-Vacancy Spin Sensor,” *Science* **339**, 557–560 (2013). — *Pioneering nanoscale NMR demonstration.*
- [8.62] T. Staudacher, F. Shi, S. Pezzagna, J. Meijer, J. Du, C. A. Meriles, F. Reinhard, and J. Wrachtrup, “Nuclear Magnetic Resonance Spectroscopy on a (5-Nanometer)³ Sample Volume,” *Science* **339**, 561–563 (2013). — *Nanoscale NMR spectroscopy.*
- [8.63] N. Aslam, M. Pfender, P. Neumann, R. Reuter, A. Zappe, F. F. de Oliveira, A. Denisenko, H. Sumiya, S. Onoda, J. Isoya, and J. Wrachtrup, “Nanoscale nuclear magnetic resonance with chemical resolution,” *Science* **357**, 67–71 (2017). — *Chemical-resolution nanoscale NMR.*

- [8.64] S. Schmitt, T. Gefen, F. M. Stürner, T. Unden, G. Wolff, C. Müller, J. Scheuer, B. Naydenov, M. Markham, S. Pezzagna, J. Meijer, I. Schwarz, M. Plenio, A. Retzker, L. P. McGuinness, and F. Jelezko, “Submillihertz Magnetic Spectroscopy Performed with a Nanoscale Quantum Sensor,” *Science* **356**, 832–837 (2017). — *Ultra-high resolution spectroscopy*.
- [8.65] J. M. Boss, K. S. Cujia, J. Zopes, and C. L. Degen, “Quantum Sensing with Arbitrary Frequency Resolution,” *Science* **356**, 837–840 (2017). — *Qdyne technique for arbitrary frequency resolution*.
- [8.66] D. R. Glenn, D. B. Bucher, J. Lee, M. D. Lukin, H. Park, and R. L. Walsworth, “High-Resolution Magnetic Resonance Spectroscopy Using a Solid-State Spin Sensor,” *Nature* **555**, 351–354 (2018). — *High-resolution NMR spectroscopy*.
- [8.67] I. Lovchinsky, A. O. Sushkov, E. Urbach, N. P. de Leon, S. Choi, K. De Greve, R. Evans, R. Gertner, E. Bersin, C. Müller, L. McGuinness, F. Jelezko, R. L. Walsworth, H. Park, and M. D. Lukin, “Nuclear magnetic resonance detection and spectroscopy of single proteins using quantum logic,” *Science* **351**, 836–841 (2016). — *Single-protein NMR detection*.
- [8.68] F. Shi, Q. Zhang, P. Wang, H. Sun, J. Wang, X. Rong, M. Chen, C. Ju, F. Reinhard, H. Chen, J. Wrachtrup, J. Wang, and J. Du, “Single-protein spin resonance spectroscopy under ambient conditions,” *Science* **347**, 1135–1138 (2015). — *Protein spin resonance at room temperature*.
- [8.69] A. O. Sushkov, I. Lovchinsky, N. Chisholm, R. L. Walsworth, H. Park, and M. D. Lukin, “Magnetic Resonance Detection of Individual Proton Spins Using Quantum Reporters,” *Phys. Rev. Lett.* **113**, 197601 (2014). — *Individual proton detection*.
- [8.70] J. Zopes, K. S. Cujia, K. Sasaki, J. M. Boss, K. M. Itoh, and C. L. Degen, “Three-dimensional localization spectroscopy of individual nuclear spins with sub-Angstrom resolution,” *Nat. Commun.* **9**, 4678 (2018). — *Sub-angstrom nuclear spin localization*.

Reviews and Recent Developments

- [8.71] C. L. Degen, F. Reinhard, and P. Cappellaro, “Quantum Sensing,” *Rev. Mod. Phys.* **89**, 035002 (2017). — *Comprehensive quantum sensing review*.
- [8.72] J. F. Barry, J. M. Schloss, E. Bauch, M. J. Turner, C. A. Hart, L. M. Pham, and R. L. Walsworth, “Sensitivity Optimization for NV-Diamond Magnetometry,” *Rev. Mod. Phys.* **92**, 015004 (2020). — *Comprehensive sensitivity optimization review*.
- [8.73] F. Casola, T. van der Sar, and A. Yacoby, “Probing Condensed Matter Physics with Magnetometry Based on Nitrogen-Vacancy Centres in Diamond,” *Nat. Rev. Mater.* **3**, 17088 (2018). — *Review of NV applications in condensed matter*.
- [8.74] J. M. Taylor, P. Cappellaro, L. Childress, L. Jiang, D. Budker, P. R. Hemmer, A. Yacoby, R. L. Walsworth, and M. D. Lukin, “High-Sensitivity Diamond Magnetometer with Nanoscale Resolution,” *Nat. Phys.* **4**, 810–816 (2008). — *Foundational NV magnetometry paper*.
- [8.75] J. Wrachtrup and F. Jelezko, “Processing quantum information in diamond,” *J. Phys.: Condens. Matter* **18**, S807–S824 (2006). — *Early NV review*.
- [8.76] L. Rondin, J.-P. Tetienne, T. Hingant, J.-F. Roch, P. Maletinsky, and V. Jacques, “Magnetometry with nitrogen-vacancy defects in diamond,” *Rep. Prog. Phys.* **77**, 056503 (2014). — *NV magnetometry review*.

- [8.77] D. A. Broadway, J.-P. Tetienne, A. Stacey, J. D. A. Wood, D. A. Simpson, L. T. Hall, and L. C. L. Hollenberg, “Quantum probe hyperpolarisation of molecular nuclear spins,” *Nat. Commun.* **9**, 1246 (2018). — *Hyperpolarization techniques*.
- [8.78] C. Zhang, F. Shagieva, M. Widmann, M. Kuhnne, D. Zhalter, T. Umemoto, M. Trupke, D. Simin, J. Wrachtrup, and P. Hemmer, “Diamond Quantum Devices in Biology,” *Annu. Rev. Biophys.* **50**, 393–414 (2021). — *Review of biological applications*.
- [8.79] E. Bauch, S. Singh, J. Lee, C. A. Hart, J. M. Schloss, M. J. Turner, J. F. Barry, L. Pham, N. Bar-Gill, S. F. Yelin, and R. L. Walsworth, “Decoherence of ensembles of nitrogen-vacancy centers in diamond,” *Phys. Rev. B* **102**, 134210 (2020). — *Decoherence mechanisms in NV ensembles*.
- [8.80] A. J. Healey, L. T. Hall, G. A. L. White, T. Teraji, M.-A. Sani, F. Separovic, J.-P. Tetienne, and L. C. L. Hollenberg, “Quantum Microscopy with van der Waals Heterostructures,” *Nat. Phys.* **19**, 87–91 (2023). — *Recent advances in quantum microscopy*.

Total references: 80. Organized by topic for reader convenience. References span foundational works (1950s) through recent developments (2023), covering pulse sequence theory, NV-specific implementations, noise spectroscopy, optimal control, wide-field imaging, and nanoscale NMR applications.